Nonlinear-optical studies of single gold nanoparticles

PROEFSCHRIFT

ter verkrijging van
de graad van Doctor aan de Universiteit Leiden,
op gezag van Rector Magnificus prof.mr. P.F. van der Heijden,
volgens besluit van het College voor Promoties
te verdedigen op woensdag 17 oktober 2007
klokke 13.45 uur

door

Meindert Alexander van Dijk
geboren te Zaanstad
in 1979

Promotiecommissie:

Promotor: Prof. Dr. M. A. G. J. Orrit
Copromotor: Prof. Dr. M. O. Lippitz   (Universität Stuttgart)
Referent: Prof. Dr. N. F. van Hulst   (ICFO Barcelona)
Overige Leden: Prof. Dr. V. Sandoghdar   (ETH Zürich)
                Prof. Dr. E. J. J. Groenen
                Prof. Dr. J. M. van Ruitenbeek
                Prof. Dr. J. P. Woerdman

voor Paul en Jenny

Contents

Contents

Preface

This thesis reflects the results of four years of research in the MoNOS group at Leiden University on the development of new techniques for the detection of single gold nanoparticles, in particular by using a pulsed laser system to excite the particles. Gold nanoparticles are spherical clusters of gold atoms with diameters typically between 1 and 100 nm. Initially, our goal was to develop a method to detect the smallest possible particles, that could be used in biophysical experiments. Gold particles are useful labels for these experiments, since they do not suffer from photoblinking and photobleaching, as molecules and nanocrystals do. Therefore, unlimited observation times come within reach, which is of great importance for experiments in which the a biological system is tracked for a long period. For a tracking experiment it is essential that the label has no influence on the mobility of the system to which it is attached. Therefore, for a method for detection of gold nanoparticles to be useful in biophysical applications, it has to enable detection of very small particles, preferably with diameters below 5 nm, with a high signal-to-noise ratio.

Pulsed lasers emit their light not continuously, but periodically in very short bursts. By concentrating the light in these short bursts, the peak powers become much higher. As an example, the laser system that I used emitted one pulse of 100 fs every 13 ns. In other words, all photons that would have been emitted in 13 ns are now emitted in 100 fs, which leads to an enhancement of the peak power by a factor of more than 10^5. These high peak powers have opened windows towards new physical effects, such as frequency mixing. Two photons can form one new photon with a frequency that is the sum or the difference of the two old photons. A special case is second-harmonic generation (SHG), in which the two original photons have the same energy, as a result of which the frequency of the new photon is twice as high. These processes are of course not limited to two photons. One step beyond SHG is third-harmonic generation (THG), in which three photons form a new photon

of three times the frequency of the source.

Besides the benefit of high peak powers, pulsed lasers also allow for studying the time evolution of processes on extremely short time scales, in which the time resolution is limited only by the length of the pulse. The technique that is most common to study the dynamics of systems at this very short time scale is called pump-probe spectroscopy. In pump-probe spectroscopy, changes of a system can be measured on a time scale on the order of the pulse length. Two pulses, a pump pulse and a probe pulse, arrive at the sample with a tunable mutual delay that can be tuned simply by changing the optical path length of one of the beams, for example by translating a mirror. The pump pulse induces a perturbation of the system, and the probe measures the effect of this perturbation at variable time intervals, thereby mapping the complete time evolution of the induced perturbation. By modulating the intensity of the pump and demodulating the detected signal with a lock-in amplifier, only the difference in response between the perturbed and unperturbed state is measured, while much of the noise is subtracted away, which largely enhances the signal-to-noise ratio.

We have used both benefits of short pulses, the high peak powers and the high time resolution, to explore new methods for detection of single gold nanoparticles. The first method we have developed was the detection of third-harmonic generation of single gold nanoparticles. In this experiment, a gold particle was excited by an infra-red laser pulse. New frequencies were generated inside the particle, with values twice (second-harmonic generation) and three times (third-harmonic generation) the frequency of the source. For spherically symmetric particles, the second harmonic is forbidden, therefore we aimed to detect the third harmonic. The method worked and we have successfully detected single particles. Additionally, we have detected a size dependence that deviates from earlier assumptions. Nevertheless, the method was not sensitive enough to detect the really small particles that we were after, and we decided to try a different method. In chapter 2, the method and results of the THG experiment are presented in detail.

We proceeded with a new experiment, no longer dwelling on generation of new wavelengths in the particle, as in the THG experiment, but instead we tried to detect the absorption of light by a single particle. We have developed a common-path interferometer, in which the probe and reference waves are not separated in space, as for example in a Michelson interferometer, but in time. Splitting and recombination of probe and reference waves was done in a birefringent crystal in which the spatial overlap is guaranteed, which made alignment of the interferometer much easier. The interferometer was

combined with a pump-probe spectroscopy setup (described above). A full description and characterization of the pump-probe interferometer is given in chapter 3. The idea for this experiment was to detect the changes in absorption of a probe pulse in the first picosecond after excitation with a pump pulse. The very large and short-lived increase in electron temperature was expected to induce large changes in the absorption spectrum of the particle, and together with the size dependence of the absorption signal, which decreases much slower for small particles than more conventional methods as scattering, we hoped that this method would enable the detection of very small gold particles.

Unfortunately, most probably due to saturation of the absorption signal, it turned out that the method was limited to detection of particles larger than 10 nm. During the experiments, we observed a peculiar oscillation in our signals, which appeared to be acoustic vibrations of single gold nanoparticles, a periodic expansion of the lattice of the particle, caused by the sudden increase in electron and lattice temperature after excitation with a short pulse. These vibrations had been detected in large ensembles already, but never before on single particles. There appeared to be a lot of interesting physics in the acoustic oscillations, and eventually, these vibrations have filled a majority of the pages in this thesis. In chapter 4 and chapter 5, the results of the vibration experiments are described. In these chapters, I present a careful characterization of the signals that we have detected in the pump-probe experiments. Proof of detection of single particles is given, a probe-wavelength analysis is demonstrated and we have studied homogeneous damping times. An ensemble measurement of acoustic vibration detects the average vibration of many particles that all vibrate at a slightly different frequency, since their sizes differ (generally the size dispersion is in the order of 5%). This effect, which reduces the damping time of the ensemble vibration due to dephasing, is called inhomogeneous broadening and is obviously absent in single-particle measurements. Only by detecting single particles it is therefore possible to detect the homogeneous damping time of the particles.

Most of the vibrations we have detected were a plainly radial expansion and contraction of the particle, called the breathing mode. A fraction of the particles however, showed an additional vibration mode, associated with ellipsoidal deformation, which had so far never been detected in pump-probe experiments. For a long time, we were puzzled why only a small fraction of our particles showed a very strong sign of this mode. The very last experiments I did could shed light on the origin of this mode, and an explanation is given in chapter 5.

The physics behind metal nanoparticles is addressed in chapter 1. Their optical and spectral properties, as well as the response of a metal nanoparticle to excitation with a short laser pulse are explained. Also, this chapter contains an overview of the field of single-particle detection (including experiments that *did* succeed in the detection of particles with a size useful for biologists).

1

Gold nanoparticles

This chapter gives an introduction to the physics behind gold nanoparticles. Discussed are the applications and the spectral and mechanical properties of the particles. The focus of this thesis is on experiments on single particles. The chapter therefore concludes with a short overview of the field of single-particle detection.

1.1 Introduction

Metal nanoparticles, with diameters ranging roughly between 1 and 100 nanometers, are natural bridges between molecules and extended solids. They are complex many-electron systems, where reduced sizes and quantum confinement of electrons and phonons give birth to fascinating new effects, potentially tunable with particle size and shape. Metal nanoparticles attract strong interest both because they open up a new field in fundamental science and because of their potential technological applications. They are convenient components for sub-wavelength optical devices [1, 2, 3, 4], for nonlinear optics [5, 6, 7], for optical data storage [8, 9], for surface-enhanced spectroscopy [10] and catalysis [11], for biological labelling and sensing [12, 13], and even for cancer therapy [14].

Until the beginning of this century, the optical properties of metal particles were invariably studied on large ensembles. These experiments included studies of optical absorption or scattering [15, 16, 17], non-linear optical properties [18], luminescence [19, 20], or structural and vibrational properties

11

[16, 17, 21]. Recent progress and interest in optical microscopy has stimulated studies of *single* metal particles. In these experiments, particles are not only isolated from one another (i.e., they do not interact), but separated by distances so large, that at most one particle is present in any given laser spot in the sample (the spot, typically a few hundreds of nanometers in diameter, is empty most of the time). Just as in the case of molecules [22, 23] or semiconductor nanocrystals [24], investigations of single metal particles add novel insight to conventional ensemble measurements, by exploiting the following advantages:

- Inhomogeneity is suppressed. Even the best preparation methods yield populations of nanoparticles which differ not only in size and shape, but also in the presence and distribution of bulk and surface defects, in chemical composition, etcetera. As in the case of semiconductor nanocrystals, of conjugated polymers, or of bio-molecules, the selection of individuals is the only possible access to well-defined objects. This is a marked difference with chemically synthesized small molecules, whose inhomogeneity usually exclusively arises from their local environment.

- Time-dependent fluctuations directly appear, without any need for synchronization. Conventional ensemble methods rely on averages over many individual systems. Therefore, they are completely blind to fluctuations whenever synchronization is not possible.

- Being small objects, single nanoparticles act as relays between a particular nanometer-sized spot and the macroscopic world in the laboratory. They can probe local properties, or tag other mobile nano-objects such as biomolecules. In such applications, their main advantage with respect to fluorescent labels will be their stability and their low reactivity. Whereas dyes and semiconductor particles blink and eventually bleach under heavy laser illumination, the many electrons of a metal particle never stop interacting with light.

1.2 Linear optical properties

The interaction of light with small particles depends strongly on the size, shape and composition of the particles, as well as on the composition of the medium in which the particles are embedded. This section reviews the theory behind the spectral properties of spherical noble metal particles (specifically
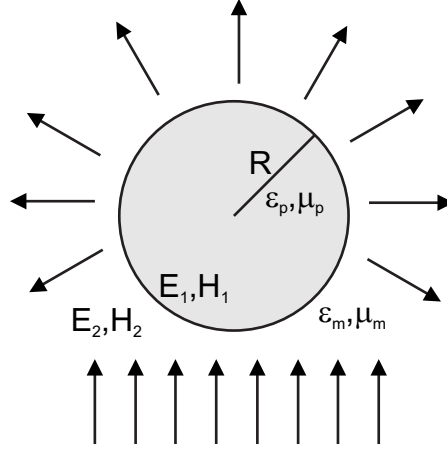
Figure 1.1: Sketch of the problem as it is treated in section 1.2.1. A particle with optical constants ϵ_p and μ_p is embedded in a medium with optical constants ϵ_m and μ_m, and illuminated by a plane wave, which generates an electric field $\mathbf{E}_1$ and a magnetic field $\mathbf{H}_1$ inside the particle. The particle radiates a scattered field in all directions, which leads, together with the applied fields, to an electric field $\mathbf{E}_2$ and a magnetic field $\mathbf{H}_2$ outside of the particle.

gold) of nanoscopic dimensions. The ultrafast dynamics of metal nanoparticles, the particle's electronic and acoustic response in the first nanosecond after a photon is absorbed, is treated in section 1.3.

If a small particle is illuminated by light, its electrons are set in an oscillatory motion, which generates radiation. This process is called *scattering*. If the particle transfers the energy of the exciting light to another energy source, e.g. heat, the light is said to be *absorbed*.

A basic absorption experiment consists of a light source and a detector placed in the path of the source. A sample containing the particles under study is then placed in the optical path, which causes a part of the light to be rejected from the detector. The total *extinction* of the light beam by the sample contains contributions of both scattering and absorption, and the extincted energy is the sum of the absorbed and scattered energy.

1.2.1 An exact solution

Solving the problem of absorption and scattering of light by a small particle involves solving Maxwell's equations with the correct boundary conditions. We use the general formulation of the problem as shown in Fig. 1.1. Assum-

ing harmonic time dependence of the light source, we can rewrite Maxwell's equations into the vector wave equation

$$\nabla^2 \mathbf{E} + k^2 \mathbf{E} = 0$$
$$\nabla^2 \mathbf{H} + k^2 \mathbf{H} = 0 \,, \tag{1.1}$$

where k is the wave number. Both the particle and the medium can be described by two non-dimensional parameters, the dielectric function ϵ and the magnetic permeability μ (generally, the relative magnetic permeability of the materials under study in this thesis is close enough to 1 to be neglected), that enter in the wave number as $k^2 = \omega^2 \epsilon \mu$. At the boundary between the particle and the medium, ϵ and μ are discontinuous. It follows from Maxwell's equations that the tangential components of the fields are continuous. For points $\mathbf{x}$ on the particle surface, we can write

$$[\mathbf{E}_2(\mathbf{x}) - \mathbf{E}_1(\mathbf{x})] \times \hat{\mathbf{n}} = 0$$
$$[\mathbf{H}_2(\mathbf{x}) - \mathbf{H}_1(\mathbf{x})] \times \hat{\mathbf{n}} = 0 \,. \tag{1.2}$$

Only if we restrict ourselves to spherical particles, is this problem exactly solvable. This was first shown in 1908 by Gustav Mie [25]. A complete derivation of Mie theory is given by Bohren and Huffman [26]. From Mie theory scattering matrices can be derived, from which information about, e.g., the direction and polarization dependence of the scattered light can be extracted. An important parameter that can be calculated with Mie theory is the *cross section*, a geometrical quantity that relates the incident light to the scattered, absorbed or extincted power.

$$\sigma_{sca} = \frac{P_{sca}}{I_{inc}} \qquad \sigma_{abs} = \frac{P_{abs}}{I_{inc}} \qquad \sigma_{ext} = \frac{P_{ext}}{I_{inc}} \tag{1.3}$$

From Mie theory, absorption, scattering and extinction cross sections for an arbitrary spherical particle with dielectric function ϵ_p can be calculated. Since extincted power is the sum of the scattered and absorbed power, the absorption cross section is simply

$$\sigma_{abs} = \sigma_{ext} - \sigma_{sca} \,, \tag{1.4}$$

while the scattering and extinction cross sections can be calculated from

$$\sigma_{sca} = \frac{2\pi}{k^2} \sum_{n=1}^{\infty} (2n+1) \left(|a_n|^2 + |b_n|^2 \right) \tag{1.5}$$

$$\sigma_{ext} = \frac{2\pi}{k^2} \mathrm{Re} \left(a_n + b_n \right) \,. \tag{1.6}$$
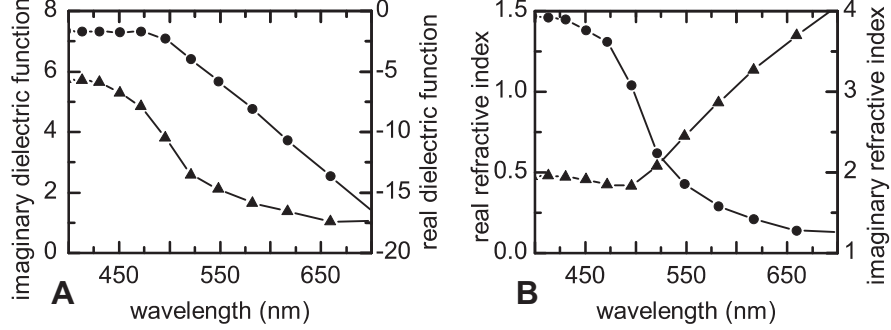
Figure 1.2: (A) Imaginary (circles) and real (triangles) part of the dielectric function of gold. (B) Imaginary (circles) and real (triangles) part of the refractive index of gold. Data measured by Johnson and Christy [27].

The coefficients a_n and b_n in Eq. (1.5) and Eq. (1.6) are given by

$$a_n = \frac{m\psi_n(mx)\psi_n'(x) - \psi_n(x)\psi_n'(mx)}{m\psi_n(mx)\xi_n'(x) - \xi_n(x)\psi_n'(mx)} \tag{1.7}$$

$$b_n = \frac{\psi_n(mx)\psi_n'(x) - m\psi_n(x)\psi_n'(mx)}{\psi_n(mx)\xi_n'(x) - m\xi_n(x)\psi_n'(mx)}, \tag{1.8}$$

in which ψ and ξ are Ricatti-Bessel functions of order n [26], $x = kR$ is a size parameter (R is the radius of the particle) and $m = \sqrt{\epsilon_p/\epsilon_m}$ is the square root of the ratio of the dielectric functions of the particle and of the medium. The prime indicates a derivation to the parameter in parentheses.

The complex dielectric function $\epsilon = \epsilon_1 + i\epsilon_2$ is related to the particle's complex refractive index $\tilde{n} = n + ik$, whose real and imaginary parts describe the spatial varieties of respectively the phase and amplitude of a wave in matter. Assuming the material is not magnetic ($\mu \approx 1$), the dielectric function and the refractive index are related by $\epsilon = \tilde{n}^2$.

The dielectric functions of most noble metals are known from experiments, mostly done in the 1960's and 1970's. The measurements by Johnson and Christy in 1972 [27], for copper, silver and gold, are generally considered to be the most reliable, and will be used throughout this thesis. Their values, in terms of both the dielectric function and the refractive index, are plotted in Fig. 1.2. Apart from a small correction below $R \approx 5$ nm [15, 28], the bulk dielectric function describes the optical properties of nanoparticles very well.

Using the experimentally determined dielectric functions of Johnson and Christy, Eqs. (1.4)-(1.8) can provide the absorption, scattering and extinction spectra of a metal nanoparticle as functions of the particle radius R and the
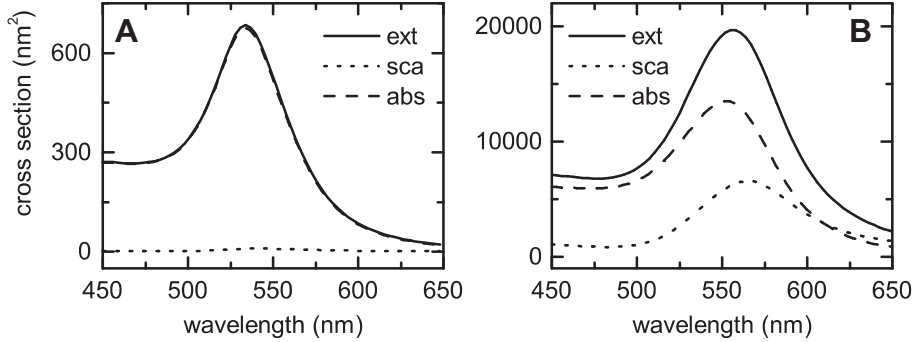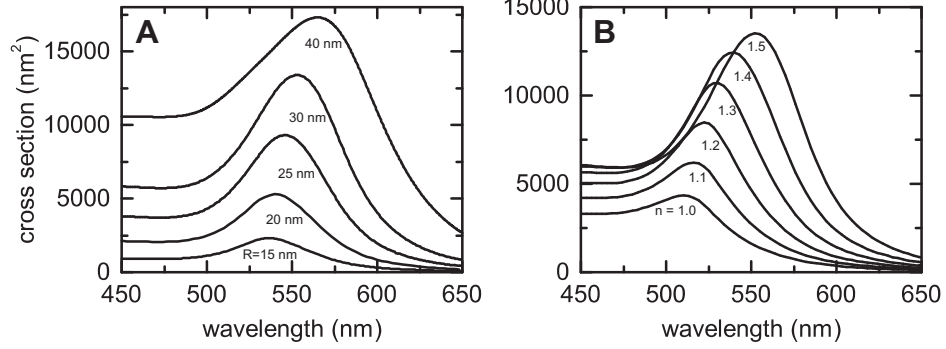
Figure 1.3: Extinction, scattering and absorption spectra of a particle with a radius of 10 nm (A) and a radius of 30 nm (B). In both cases, the refractive index of the environment is 1.5. Note that for the 10-nm particle, the scattering cross section nearly vanishes, and as a result of that, the absorption and extinction cross sections are approximately equal.

refractive index of the medium n_m in which it is embedded. Figure 1.3 shows examples of these spectra for two differently sized particles, $R = 10$ nm and $R = 30$ nm, embedded in a medium of $n_m = 1.5$. All spectra have a relatively broad resonance around $\lambda = 550$ nm, caused by the collective plasma oscillations of the free electron gas. The resonance is red- shifted for larger particles, and the scattering peak generally lies further to the red than the absorption peak. Also, especially the absorption spectra are highly asymmetric, showing a plateau for low wavelengths, due to absorption by the bound (d-band) electrons. Fig. 1.4 gives a closer look at how the absorption cross section depends on size (Fig. 1.4A) and the refractive index of the environment (Fig. 1.4B). The absorption cross section increases with size as R^3. If the size of the particle becomes comparable to the wavelength of the light inside the metal, the phase of the electric field can no longer be considered uniform over the particle. This induces a retardation effect, which results in a red shift of the surface plasmon resonance.

1.2.2   Simplifying matters

Although Mie theory gives an exact solution for any spherical particle, it can in some cases be useful to obtain simpler formulas for the cross sections using some approximations. We can make life easier if we only consider particles that are small compared to the wavelength of the light with which they are excited. In this regime, which is called the Rayleigh limit, we require for the

Figure 1.4: Absorption spectra for increasing radius with $n_m = 1.5$ (A), and for increasing refractive index with $R = 30$ nm (B).

size parameter $x = kR$ that

$$|m|x \ll 1 . \tag{1.9}$$

We can now derive expressions for the absorption, scattering and extinction cross sections via two approaches. One is to make a power series expansion of the full Mie solution and reduce the solution to only the first term. A different approach, which leads to the same result, is to consider the particle to be an ideal dipole. We will first place a spherical particle in a static field to show that the field it induces is the same as that of an ideal dipole. Then we will replace the static field by a plane wave to calculate the cross sections.

If we start with a spherical particle with dielectric function ϵ in a uniform electric field E_0, we can define scalar potentials V_1 inside and V_2 outside the sphere

$$\begin{aligned} \mathbf{E}_1 &= -\nabla V_1 \\ \mathbf{E}_2 &= -\nabla V_2 \end{aligned} \tag{1.10}$$

where

$$\begin{aligned} \nabla^2 V_1 &= 0 \\ \nabla^2 V_2 &= 0 \end{aligned} \tag{1.11}$$

and the boundary conditions (at $r = R$) in this problem are

$$\begin{aligned} V_1 &= V_2 \\ \epsilon_p \frac{\delta V_1}{\delta r} &= \epsilon_m \frac{\delta V_2}{\delta r} \; . \end{aligned} \tag{1.12}$$

17

Furthermore, we require that the electric field is unaffected by the sphere at large distances. It is then possible to show, that the potential outside the sphere equals

$$V_2 = R^3 E_0 \frac{\epsilon_p - \epsilon_m}{\epsilon_p + 2\epsilon_m} \frac{\cos\theta}{r^2} \, , \qquad (1.13)$$

where θ gives the direction of the scattered wave with respect to the propagation direction of the source. This is the same potential we would get if we would replace the sphere by a dipole, consisting of a positive and a negative charge, separated by a distance $d = 2R$. This means that the applied field induces a dipole moment, which allows us to define a polarizability α.

$$\mathbf{p} = \epsilon_m \alpha \mathbf{E}_0 \qquad (1.14)$$

$$\alpha = 4\pi R^3 \frac{\epsilon_p - \epsilon_m}{\epsilon_p + 2\epsilon_m} \qquad (1.15)$$

If we now replace the static applied field by a plane wave, it can be shown that the dipole radiates a scattered field which is proportional to the polar-
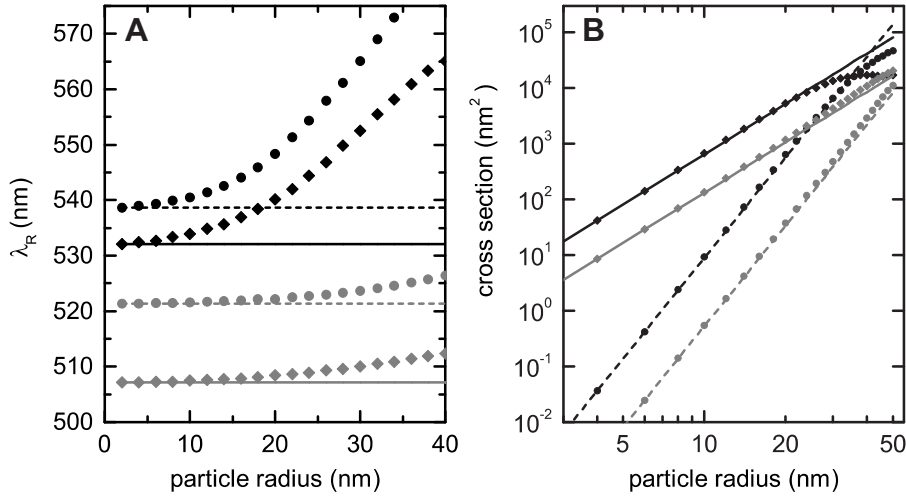
Figure 1.5: (A) Comparison of the resonance wavelength in the dipole approximation and for Mie theory, for $n_{env} = 1.0$ (grey) and $n_{env} = 1.5$ (black). The circles (Mie) and dashed lines (dipole) represent scattering, the diamonds (Mie) and solid lines (dipole) represent absorption. (B) Comparison of the absorption and scattering cross sections at the resonance wavelength in the dipole approximation and for Mie theory, for $n_{env} = 1.0$ (grey) and $n_{env} = 1.5$ (black). The symbol coding is the same as in (A), note the log-log scale.

izability and the applied field. This gives the following cross sections in the small-particle limit [26].

$$\sigma_{abs} \approx \sigma_{ext} \quad = \quad \mathrm{k}\,\mathrm{Im}(\alpha) = 4\pi\,\mathrm{k}\,R^3\,\mathrm{Im}\left(\frac{\epsilon_p - \epsilon_m}{\epsilon_p + 2\epsilon_m}\right) \tag{1.16}$$

$$\sigma_{sca} \quad = \quad \frac{\mathrm{k}^4}{6\pi}\,|\alpha|^2 = 8\pi\,\mathrm{k}^4\,R^6\,\left|\frac{\epsilon_p - \epsilon_m}{\epsilon_p + 2\epsilon_m}\right|^2 \tag{1.17}$$

For very small particles, scattering is almost negligible compared to absorption, which is why the absorption cross section is approximately equal to the extinction cross section. Eqs. (1.16) and (1.17) predict a resonance if the denominator $\epsilon_p + 2\epsilon_m = 0$. In the dipole approximation, which does not take retardation into account, this resonance is independent of particle size. Fig. 1.5 shows the absorption as well as the scattering cross section for two different values of n_m (solid and dashed lines). The circles and diamonds in the same plot show the position of the resonance as calculated from Mie theory. The deviation between the dipole approximation and Mie theory is clearly visible for larger particles, although the extent of deviation depends on n_m. Eqs. (1.16) and (1.17) also give information on the size dependence of the absorption and scattering cross sections. Whereas scattering increases with the sixth power of the size of the particle, absorption scales with the third power. As a result of this, for small particles, the absorption cross section is larger than the scattering cross section (see Fig. 1.5), and an absorption-based detection technique is therefore much more sensitive to detect small particles than a method based on scattering. As can be seen in Fig. 1.5, these size dependencies hold well beyond the Rayleigh limit.

1.2.3   Temperature dependence

Johnson and Christy [27] only measured their values for the dielectric functions of noble metals at room temperature. In 1961, Otter [29] measured the dielectric functions of noble metals in the solid phase for a range of temperatures up to the melting point, and in the liquid phase at the melting point. His data is shown in Fig. 1.6. A comparison of Otter's room-temperature data with the data measured by Johnson and Christy (see Fig. 1.2) reveals that the experiments do not agree. Since Johnson and Christy used a more sophisticated method to measure the dielectric functions, it is likely that Otter's values are not very accurate. Nevertheless, it can be very insightful to apply Mie theory to these dielectric functions, and obtain absorption spectra of gold nanoparticles as a function of the temperature of the particle.

In Fig. 1.7A, we have plotted the absorption spectrum (in the dipole limit), of a particle with a 10-nm radius, embedded in a medium with a refractive index of 1.5, for various temperatures. With increasing temperature, the absorption cross section decreases and the spectra shift towards the red. If the particle melts, the resonance completely disappears. The grey spectrum is that of the same particle at room temperature, using Johnson and Christy's values for the dielectric function. As mentioned earlier, there is a large discrepancy between the data of Johnson and Christy and Otter's room-temperature data points. Therefore, it is not possible to use these spectra to measure the temperature of the particle. Only the qualitative trend in the temperature dependence can be trusted.

It has been predicted that the melting of a nanoparticle goes via surface melting. Before the particle becomes fully liquid at a melting temperature of 1063°C, it first forms a liquid shell around a solid core. A number of heating experiments on metal nanoparticles suggest the formation of a liquid shell at temperatures below the melting point [30, 31, 32, 33]. We can combine the temperature-dependent dielectric function of Otter with a theoretical description of core-shell particles to calculate the effect of liquid-shell formation on the melting process. The geometry of a core-shell particle is defined in Fig. 1.8. The easiest way to calculate the absorption of a core-shell particle, is to use the polarizability as it is given by Kreibig and Vollmer [28] and Van de Hulst [34], of a particle consisting of a core and a shell of two different
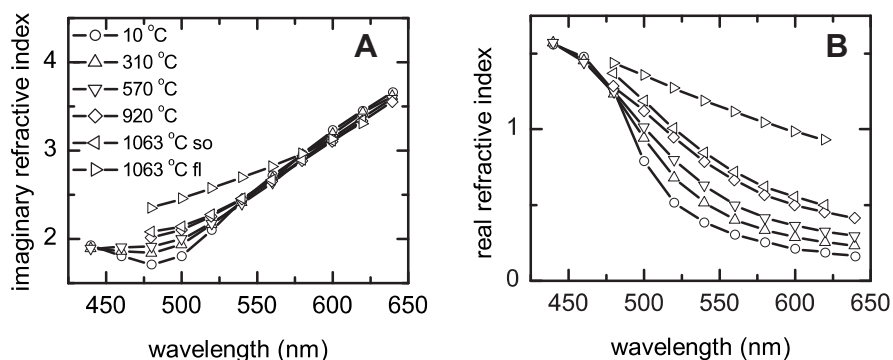
Figure 1.6: Imaginary (A) and real (B) part of the refractive index of gold, for various temperatures in the solid phase and in the liquid phase at the melting point, as measured by Otter [29]. The symbol coding is the same for both panels.
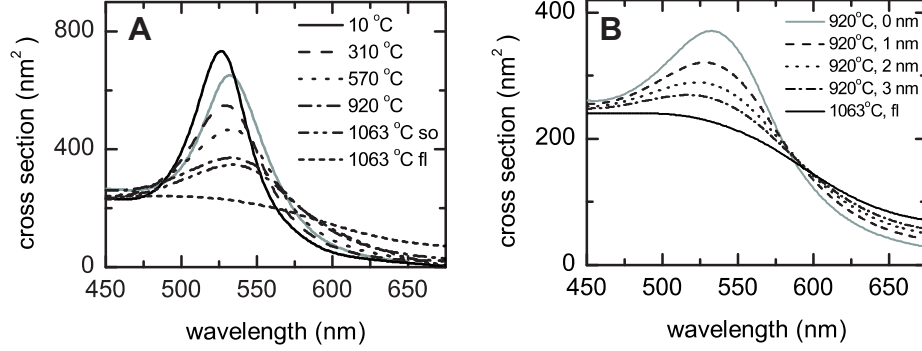
Figure 1.7: (A) Absorption spectra for a particle with a radius of 10 nm, embedded in a medium with a refractive index of 1.5, as a function of temperature, calculated with the temperature-dependent dielectric functions of Otter [29]. The grey spectrum is an absorption spectrum of an identical particle, using the dielectric functions of Johnson and Christy [27], for comparison. (B) The dotted lines show absorption spectra for a liquid-shell particle with varying shell thickness. The temperature of the solid core is 920°C, the temperature of the liquid shell is 1063°C. The solid lines are absorption spectra of a solid particle with a temperature of 920°C (grey), and a fully liquid particle at 1063°C.

materials (as sketched in Fig. 1.8).

$$\alpha_{cs} = 4\pi(R+d)^3 \frac{(\epsilon_s - \epsilon_m)(\epsilon_c + 2\epsilon_s) + \left(\frac{R}{R+d}\right)^3 (\epsilon_c - \epsilon_s)(\epsilon_m + 2\epsilon_s)}{(\epsilon_s + 2\epsilon_m)(\epsilon_c + 2\epsilon_s) + \left(\frac{R}{R+d}\right)^3 (\epsilon_c - \epsilon_s)(2\epsilon_s - 2\epsilon_m)} \quad (1.18)$$

Although we restrict ourselves to the Rayleigh regime in this way, the calculations become much easier, and this approach suffices very well for the purpose we have in mind, which is to acquire a qualitative picture of the melting process. Note that the formula of Kreibig and Vollmer contains a mistake, and Van der Hulst only gives the polarizability in a medium with $n_m = 1$. Eq. (1.18) is the correct formula for an arbitrary medium, which can be verified by choosing the dielectric constant of the shell to be the same as that of either the core or the medium. In both cases, Eq. (1.18) reduces to the polarizability of a homogeneous particle with the expected parameters.

Having established a method to (theoretically) produce core-shell particles, we can now make liquid-shell particles, by applying Eq. (1.18) with the dielectric function of a solid particle with a temperature of, e.g., 920°C for the core and the dielectric function of a fluid particle for the shell. This has been plotted for three different shell thicknesses in Fig. 1.7B. Besides a further decrease in the absorption cross section, a blue shift can be observed when the
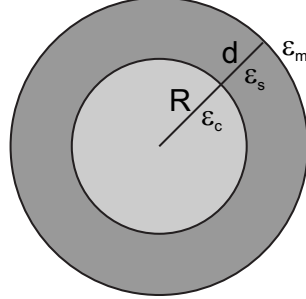
Figure 1.8: Sketch of a core-shell particle. A core of radius R and dielectric function ϵ_c is surrounded by a shell of thickness d and dielectric function ϵ_s. The particle is embedded in a medium ϵ_m.

liquid shell becomes thicker. This blue shift can be a method to identify surface melting.

From the spectra in Fig. 1.7, a number of predictions can be made for an experiment in which the melting of gold nanoparticles is studied. In such an experiment, a gold nanoparticle would be heated with a CW laser, with which the particle can be kept stable at a certain temperature, that depends on the laser intensity. Now the absorption spectrum can be probed with a white-light source and a spectrometer, as a function of particle temperature. The temperature of the particle can be calculated from the heating intensity by solving a heat-balance equation.

$$\sigma_{abs} I = 4\pi R^2 K_m \left[\frac{\delta T}{\delta r} \right]_R \tag{1.19}$$

Here, I is the intensity if the heating laser and K_m the thermal conductivity of the medium ($K_m = 1.3$ W m^{-1} K^{-1} for fused silica). Rewriting this equation, using $[\delta T / \delta r]_R = \Delta T / R$, yields the intensity I that is needed to heat a particle of radius R to a temperature ΔT above room temperature.

$$I = \frac{4\pi R K_m}{\sigma_{abs}} \Delta T \tag{1.20}$$

We have assumed here that the absorption cross section σ_{abs} is independent of temperature. From Fig. 1.7A, we see that close to the resonance, the absorption cross section has a very strong temperature dependence. The most obvious choice for the wavelength of the heating laser, close to the resonance, is therefore not the best one, since at these wavelengths the temperature of the particle depends on the laser power in a nonlinear (and *a priori*
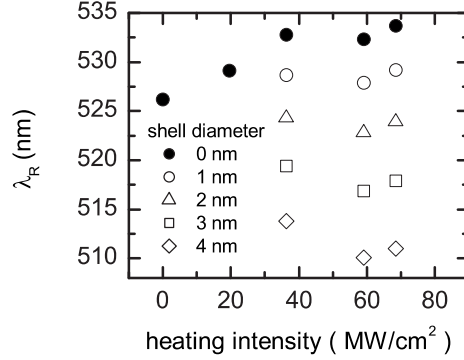
Figure 1.9: Resonance wavelength of the absorption spectrum of a gold nanoparticle with a 10-nm radius as a function of heating intensity. If the particle undergoes liquid-shell formation during the melting process, the absorption spectrum will blue shift before the resonance disappears when the particle becomes fully liquid. The magnitude of the blue shift depends on the shell thickness. The data points without a liquid shell correspond to a particle temperature of 10°C, 310°C, 570°C, 920°C and 1063°C respectively.

unknown) way. For this calculation, we will choose a heating wavelength of 475 nm, where the cross section is nearly temperature-independent. For larger particles, for which the resonance lies further towards the red, the Ar^+ line at 488 nm is also a good choice. From Eq. (1.20), we can calculate the intensity that is needed to melt the particle. For a gold nanoparticle with a radius of 10 nm, this is 70 MW/cm^2, which is the intensity of a 50 mW laser beam, focussed to a diffraction limited spot with a NA 1.4 microscope objective. The melting intensity is inversely proportional to the square of the particle radius, since the absorption cross section scales with the particle volume.

As was already shown in Fig. 1.7B, the absorption spectrum of a gold nanoparticle undergoes a blue shift upon surface melting. This can be a method to identify a possible contribution of surface melting to the melting process. From Eq. (1.19), we can estimate the heating intensity necessary to stabilize the particle at a certain temperature. Using the temperature-dependent dielectric functions of Otter, we can now determine the resonance wavelength we expect at this intensity. This dependence is shown in Fig. 1.9, where the closed circles indicate melting without liquid-shell formation. In this case, we would expect a gradual red shift of the spectra up to the melting intensity, where the resonance disappears when the particle is completely liquified. Liquid-shell formation below the melting point might be observ-

able as a blue shift of the absorption spectrum, initiated at intensities below the melting intensity, as shown in Fig. 1.9B with open symbols, for liquid shells between 1 and 4 nm, formed at temperatures below the melting point.

In conclusion, an experiment in which the temperature dependence of the absorption spectrum of a gold nanoparticle is measured can provide information on the melting process of gold nanoparticles, such as liquid shell formation, and with a simple calculation, we were able to make predictions for the outcome of such an experiment. Nevertheless, it has to be noted that the temperature-dependent dielectric functions on which these calculations are based, are not accurate enough to make quantitative conclusions. The temperature at which liquid-shell formation is initiated can be estimated, since liquid-shell formation is accompanied by a significant blue shift of the spectrum.

1.3   Ultrafast dynamics

The dynamics of metals on a sub-picosecond scale have been studied on metal films [35, 36, 37] and ensembles of nanoparticles [15, 16, 17] for many decades. These experiments demonstrate a complex interaction of lattice and electrons with the exciting light pulses. The rise and decay of electron and lattice temperatures are found to evolve in a distinct series of steps. On top of that, for gold and silver nanoparticles, acoustic vibrations of the lattice, launched by short laser pulses, have been observed [38, 39, 40]. In this section, these processes are discussed, together with some of the models that have been proposed to explain the experiments.

1.3.1   Cooling dynamics

The response of gold nanoparticles to excitation with light evolves in a number of steps. These steps are shown schematically in Fig. 1.10. After excitation with a laser pulse, the excitation energy is primarily transferred to the electrons and not to the lattice, due to the much smaller heat capacity of the lattice. A part of the electron distribution is excited and the electrons will be set in a coherent oscillatory motion, which is damped on a 10-fs timescale. The initial excitation creates a largely non-thermal distribution. Through electron-electron scattering, the energy is redistributed over the entire electron distribution within a few hundred femtoseconds. This brings the electrons in thermal equilibrium and creates a hot electron gas, which will subsequently release its energy, thereby heating the lattice. The latter process, which is in fact initiated before the electron gas is completely in equilibrium, takes
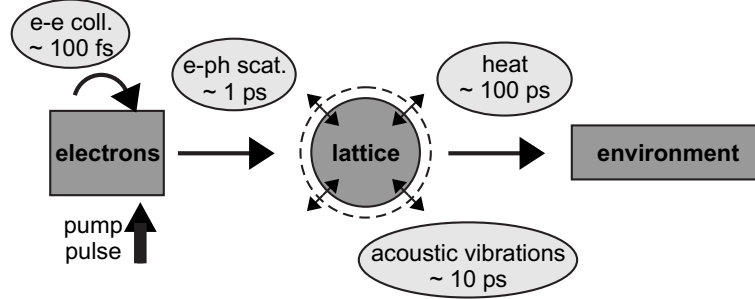
Figure 1.10: Schematic picture of the excitation and relaxation dynamics of metal nanoparticles. After excitation, heat is transferred from the electrons via the lattice to the environment in a series of steps. Sudden expansion of the lattice induces a vibration in the particle.

place in about 1 ps, and brings the electrons in thermal equilibrium with the lattice. The final step is cooling of the lattice, through heat diffusion to the environment. Typically less than a nanosecond after excitation, the particle has returned to its initial state.

The relaxation of the electron gas is described by the two-temperature model. We can define two subsystems, each with their own temperature (T_e for the electron gas, T_l for the lattice). The thermalization of the two systems can then be described by two coupled differential equations [35, 36].

$$C_e(T_e)\frac{\delta T_e}{\delta t} = -G(T_e - T_l) \tag{1.21}$$

$$C_l\frac{\delta T_l}{\delta t} = G(T_e - T_l) - \frac{1}{\tau_c}(T_l - T_0) \tag{1.22}$$

G is the electron-phonon coupling constant and C_l and C_e are the heat capacities of the lattice and the electron gas. The electronic heat capacity is temperature dependent, $C_e = \gamma T_e$ (γ is a proportionality constant [41]). The temperature dependence of the lattice is very weak, so we can assume this parameter to be temperature independent. The solution of the above set of differential equations is a decay of the electron temperature, with a time constant $\tau = \gamma T_e/G$. The dependence of the decay time constant on the pump power (the electron temperature after excitation depends on pump power) leads to a non-exponential decay. The second term in Eq. (1.22) describes the energy transfer of the lattice to the surroundings, with a characteristic cooling time τ_c [41, 42].

1.3.2   Acoustic vibrations

The cooling of the electrons and thereby the heating of the lattice takes place on a 1-ps timescale. The lattice will undergo thermal expansion, but the timescale of expansion is in the order of tens of picoseconds (for particles larger than 30 nm). Lattice heating is therefore much faster than lattice expansion, which will lead to an overshoot of the lattice expansion [43]. Additionally, due to the strong and fast increase of the electron temperature, there is a sudden increase of the electron pressure, which induces a force on the lattice and contributes to the sudden lattice expansion [44]. This has the same effect on the nanoparticle as the beat of a clapper has on a bell. The particle will start to 'ring'; a periodic expansion of the lattice is launched, which is called an acoustic vibration. The timescale of the vibration is directly related to the sound velocity of the material of the particle and to its size.

The frequency of this vibration can be calculated using macroscopic elastic theory for spheres, which was conceived by H. Lamb, already in 1882 [45], and has since then been successfully applied to materials sized anywhere between a metal nanoparticle [46] and the earth (in fact, the lowest-order vibrational mode of our planet has a period of about 21 minutes, and can be excited by earthquakes) [47]. Lamb's theory predicts vibration in different quantified modes, that are characterized by two integers, n for the harmonic order of the vibration, and l for angular momentum. The mode that is usually detected in time-resolved experiments is the breathing mode, with integer values $(n, l) = (0, 0)$. Note that some discrepancy exists in literature on the definition of the lowest harmonic order, which can be $n = 0$ (e.g., Ref. [48]) or $n = 1$ (e.g., Ref. [46]). Throughout this thesis, we define the lowest harmonic order to be $n = 0$.

The frequencies of the different modes can be found from the Navier equation [46].

$$ v_L^2 \, \nabla \cdot (\nabla \cdot \mathbf{u}) - v_T^2 \, \nabla \times (\nabla \times \mathbf{u}) = \omega^2 \, \mathbf{u} \, , \qquad (1.23) $$

where v_T and v_L are the transversal and longitudinal sound velocities of the vibrating medium. Solving this equation of motion in a spherical coordinate system for a displacement $\mathbf{u}(\mathbf{r}, t) = \mathbf{u}(\mathbf{r})e^{-i\omega t}$ in terms of dimensionless eigenvalues ξ_L and ξ_T

$$ \xi_{L,T} = \omega \frac{R}{v_{L,T}} \, , \qquad (1.24) $$

results in an equation for a free boundary (i.e., the sphere is in vacuum), for

modes with and without angular momentum.

$$\frac{\tan(\xi_L)}{\xi_L} = \frac{1}{1 - (v_L^2/4v_T^2)\,\xi_L^2} \qquad (l = 0)\,, \tag{1.25}$$

and

$$
\begin{aligned}
&-\frac{\xi_T^2\,\xi_L^2}{2}\left(2l^2 - l - 1 - \frac{\xi_T^2\,\xi_L^2}{2}\right) j_l(\xi_T)\,j_l(\xi_L) + \\
&(l^3 + 2l^2 - l - 2 - \xi_T^2\,\xi_L^2)\,\xi_L\,j_{l+1}(\xi_L)\,j_l(\xi_T) + \\
&\left(l^3 + l^2 - 2l - \frac{\xi_T^2\,\xi_L^2}{2}\right)\xi_T\,j_l(\xi_l)\,j_{l+1}(\xi_T) + \\
&(2 - l^2 - l)\,\xi_L\,\xi_T\,j_{l+1}(\xi_L)\,j_l(\xi_T) = 0 \qquad (l \neq 0)\,,
\end{aligned}
\tag{1.26}
$$

where j_l and j_{l+1} are spherical Bessel functions. If the boundary is completely rigid, the eigenvalues can be calculated from

$$\tan(\xi_L) = \xi_L \qquad (l = 0)\,, \tag{1.27}$$

and

$$\xi_L\,j'_l(\xi_L)\left[\xi_T j'_l(\xi_T) + j_l(\xi_T)\right] = l(l+1)j_l(\xi_L)j_l(\xi_T) \qquad (l \neq 0)\,. \tag{1.28}$$

A mode pattern has been calculated and is presented in Table 1.1, where the ratio between the period of the mode and the diameter of the particle is given, as well as the relative frequency of the mode with respect to the breathing mode.

	$\frac{d(nm)}{T(ps)}\left(\frac{\Omega_{(n,l)}}{\Omega_{(0,0)}}\right)$	free	$\frac{d(nm)}{T(ps)}\left(\frac{\Omega_{(n,l)}}{\Omega_{(0,0)}}\right)$	rigid
l	$n=0$	$n=1$	$n=0$	$n=1$
0	3.039 (1.000)	6.391 (2.103)	4.637 (1.000)	7.971 (1.719)
1	1.433 (0.472)	2.825 (0.929)	1.918 (0.414)	2.549 (0.550)
2	1.016 (0.334)	2.029 (0.668)	2.539 (0.548)	3.463 (0.747)
3	1.521 (0.500)	2.649 (0.871)	3.036 (0.655)	4.205 (0.907)
4	1.957 (0.644)	3.256 (1.071)	3.501 (0.755)	4.786 (1.032)

Table 1.1: Ratio between diameter and oscillation period (in nm/ps) of a number of modes, for gold spheres in the free and rigid boundary limits, calculated with Eqs. (1.26) and (1.28). Between brackets, the frequency of the mode $\Omega_{(n,l)}$ relative to the breathing mode $\Omega_{(0,0)}$ is given. The sound velocities and density of gold are v_L = 3240 m/s, v_T = 1200 m/s and ρ = 19,700 kg/m^3.

The model described above does not predict damping of the acoustic modes. Yet damping is experimentally observed, and it would therefore be desirable to be able to calculate damping times of nanoparticles embedded in a homogeneous medium. The parameter that determines the acoustic interaction of a sphere and a matrix is the acoustic impedance of both materials $Z = \rho v_L$, where ρ is the material density and v_L is the longitudinal sound velocity of the material. The acoustic impedance governs the reflection of sound waves at a material interface. If the impedance of a sphere equals the impedance of a matrix in which it is embedded, sound waves are not reflected but propagate out of the sphere immediately, and the mode will be highly damped. If there is a large impedance mismatch between the sphere and the matrix, the sound waves are strongly reflected and will remain confined in the sphere much longer. In this case, the acoustic mode will have a very low damping.

For radial modes ($l = 0$), the influence of a matrix surrounding the particle can be described with the complex-frequency model [49, 50, 51]. As for the free-sphere and bound-sphere models described above, the complex-frequency model involves solving the Navier equation for sphere displacements with harmonic time dependence. If the continuity of the displacement and stress at the interface between the sphere and the matrix are considered, the vibration of the sphere can be described in terms of a complex-valued frequency $\tilde{\omega} = \omega + i\gamma$, where γ now describes the damping of the system. $\tilde{\omega}$ can be written in terms of a complex-valued dimensionless eigenvalue $\tilde{\xi}$.

$$\tilde{\xi} = \tilde{\omega} \frac{R}{v_L^{(s)}} \tag{1.29}$$

where $v_L^{(s)}$ is the longitudinal sound velocity of the sphere, and R is its radius. $\tilde{\xi}$ can be calculated from the following equation.

$$\tilde{\xi} \cot \tilde{\xi} = 1 - \left(\frac{\tilde{\xi}^2}{\eta} \right) \frac{1 + \tilde{\xi}/\alpha}{\tilde{\xi}^2 + (2\alpha\epsilon)^2 (1/(\eta\beta^2) - 1)(1 + i\tilde{\xi}/\alpha)} \tag{1.30}$$

The parameters α, β, ϵ and η describe the longitudinal and transverse sound velocities and the densities of the sphere and the medium, $v_{L,T}^{(s),(m)}$ and $\rho^{(s),(m)}$ as

$$\alpha = \frac{v_L^{(m)}}{v_L^{(s)}} \qquad \beta = \frac{v_T^{(m)}}{v_T^{(s)}} \qquad \epsilon = \frac{v_T^{(m)}}{v_L^{(m)}} \qquad \eta = \frac{\rho^{(m)}}{\rho^{(s)}} \;. \tag{1.31}$$

We can calculate vibration frequencies and damping rates using this model, for a nanoparticle embedded in any medium, as long as the longitudinal and

transversal sound velocities and the density of the medium and the particle material are known. For a number of common matrices as well as for gold and silver, these values can be found in Table 1.2 and [50].

The acoustic vibrations of metal nanoparticles can be observed in the time domain by pump-probe spectroscopy [16, 17], or in the frequency domain with Raman spectroscopy [46]. In the time domain, a damped oscillation is observed, and the modes are characterized by the period T and the $1/e$ damping time τ of the oscillation (the amplitude is not considered here).

$$y(t) = e^{-t/\tau} \cos \left(2\pi t/T \right), \tag{1.32}$$

In the frequency domain, a Lorentzian line is observed, and the mode is characterized by the central frequency f_0 and the full width at half maximum (FWHM) Γ of the line.

$$S(f) = \frac{1}{\pi} \frac{\Gamma/2}{(f - f_0)^2 + (\Gamma/2)^2} \tag{1.33}$$

The time and frequency domain are related through a Fourier transform. From the Fourier transform of the spectral density in Eq. (1.33),

$$S'(t) = e^{-i2\pi f_0 t - \pi \Gamma t} \tag{1.34}$$

we see that the central frequency of the Lorentzian and the vibration period of the transient are related as $f_0 = T^{-1}$ and the damping time of the transient and the FWHM of the Lorentzian as $\tau = (\pi \Gamma)^{-1}$. The complex frequency $\tilde{\omega}$ that follows from Eqs. (1.29) and (1.30) can be expressed in terms of the period T and $1/e$ damping time τ as

$$\tilde{\omega} = \omega + i\gamma = \frac{2\pi}{T} + i\,\frac{1}{\tau}. \tag{1.35}$$

Table 1.2 shows the calculated period and damping times for gold nanoparticles embedded in various media. The particle radius of 28 nm is chosen since it is the average radius of the particles used in the experiments in section 5.3, where a comparison of these calculated values with experiments will be made. The periods depend only very little on the environment of the particle. The damping times on the other hand are strongly influenced by their surroundings. This makes damping-time analysis a good candidate for the application of gold nanoparticles as local probes for their environment.

| Matrix	ρ (kg/m^3)	v_L (m/s)	v_T (m/s)	T (ps)	τ (ps)
SiO2	2200	5970	3765	17.7	53.8
BK7	2240	5100	2840	18.1	54.4
PVA	1300	(*) 2350	(*) 2000	18.3	157
Water	1000	1500	–	18.7	327

Table 1.2: Vibration periods and damping times for gold nanoparticles with a radius of 28 nm, embedded in several matrices. The density and longitudinal and transversal sound velocities of gold are ρ = 19,700 kg/m^3, v_L = 3240 m/s and v_T = 1200 m/s. (*) The sound velocities of PVA in a film are not known, so the values of polystyrene were used instead.

1.3.3 Optical contrast

The picosecond-scale dynamics of metal nanoparticles can be detected optically through changes in the complex refractive index of the particle. The excitation of the electrons and the subsequent heating of the electron gas increases the probability for electron scattering processes. This in turn results in an increased damping of the surface plasmon resonance and hence to a broader spectrum [52].

Also the lattice expansion can be detected optically. Due to the expansion of the lattice, the electron density decreases, which manifests itself, through a change in the refractive index of the particle, as a red shift of the plasmon resonance. Since an acoustic vibration is a periodic expansion of the lattice, it can be detected optically as a periodic oscillation of the electron density, and thus as a periodic red shift of the resonance.

The change of the surface plasmon resonance is sketched in Fig. 1.11A for the electron heating in the first picosecond, and in Fig. 1.11B for the lattice heating. This change can be detected by *pump-probe spectroscopy*. This technique is based on two pulses, a pump pulse and a probe pulse, and exploits the changes in spectral response that are induced by a pump pulse. In other words, a metal nanoparticle is excited by a pump pulse at a time $t = 0$, which induces a series of heating and cooling steps as described in this section. These steps will, at different time intervals, lead to spectral changes as shown in Fig. 1.11. A probe pulse (weak enough not to change the state of the particle) that arrives at the sample an interval Δt later than the pump, will sense the particle in the state as produced by the pump pulse. If the intensity of the pump beam is modulated, and the detected signal is demodulated with a lock-in amplifier, the difference between a state perturbed by the pump and an unperturbed state is measured, which largely enhances the sensitivity of
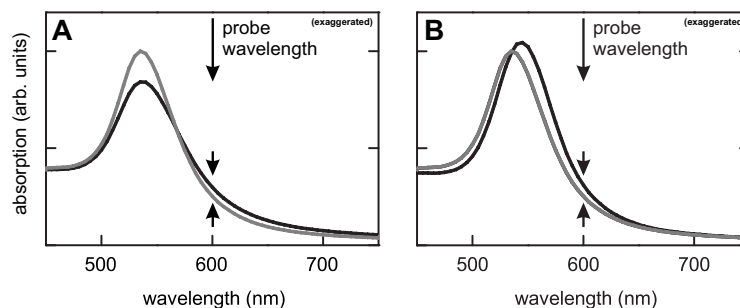
Figure 1.11: Sketch of the effect of the electronic temperature rise (A) and the lattice expansion (B) on the absorption spectrum of a gold nanoparticle. The grey lines are the absorption spectrum of an unperturbed or cold nanoparticle. The black lines give the absorption spectrum of an excited gold nanoparticle. The heating of the electrons broadens the spectrum, while the heating of the lattice causes a red shift.

the experiment. This difference is indicated with arrows in Fig. 1.11. As a final step, the interval between pump and probe can be varied, and in this way the full time response of the particle can be probed with a time resolution that is only limited by the length of the pulses.

1.4   Detection techniques

There are several approaches to the far-field optical detection of individual metal nanoparticles. They can be based on the generation of new wavelengths by the particle, either in a linear photoluminescence process [53, 54, 55] or in nonlinear processes [5, 56, 57]. Alternatively, detection can be done at the same wavelength as the one at which the particle was excited (or probed, in the case of a two-color experiment such as pump-probe spectroscopy or photothermal imaging). One can then directly detect the scattered light [58, 59], or directly or indirectly use the interference of the scattered wave with a reference wave. The advantage of the interference signal is that it varies only with the third power of the particle size, whereas the directly scattered intensity varies with the sixth power. As a result, techniques based on direct scattering are much less sensitive for small particles. Interferometry not only improves the sensitivity of both absorption-based and scattering-based methods, but it can also give access to both the amplitude and the phase of the scattered wave. Short laser pulses can be used to probe the time-dependent optical response of metal nanoparticles. Combination of high temporal or spectral resolution with the ultimate spatial resolution at the single-particle

level gives a new insight into the electronic relaxation processes of nanoparticles [60, 61], as well as into their vibrational properties [62].

The simplest way of optically detecting metal nanoparticles is via the light they scatter [63]. By tuning the probing wavelength to the plasmon resonance, one considerably improves selectivity against non-metallic objects, and one can access sizes down to a few tens of nanometers [12, 58, 59]. As mentioned, the main drawback of this method is that the scattered intensity decreases steeply (as R^6) for small particles. Despite the large index contrast between the metal and its surroundings, scattering of a single particle smaller than about 30 nm can no longer be discerned from the scattering of other (often numerous) scatterers.

A number of recently proposed methods for studying single nanoparticles rely on detection of E_{sca}, the *field* scattered by the particle, which decreases as R^3 only. This scattered field is mixed with some suitable, larger, reference field E_{ref}. The reference and scattered waves are required to be coherent, and their spatial modes should overlap to a large extent (ideally, they should be identical). Otherwise, only the intensities add, and the benefit of the field's weaker size-dependence is lost. Practically, the interference can be implemented in many different ways. The reference wave can be the incident wave itself [64], a reflection of the incident wave on a close-by interface [65, 66, 67], the auxiliary wave in a DIC setup [68], in a Michelson interferometer [69], or in a common-path polarization interferometer [70]. The scattered wave can be directly produced by the nanoparticle's dipole itself, or can result from scattering of some other local index inhomogeneity related to the particle. In the photothermal method [67, 68, 71] this inhomogeneity is induced by heat that the particle releases upon absorption of a pump beam. Note that direct absorption measurements [64] fit the same scheme of mixing a reference and a scattered wave. Indeed, absorption follows from interference of the incident wave with the forward-scattered wave, as stated by the optical theorem [72, 73]. There are different ways to detect small intensity changes resulting from the interference. One can modulate one of the interfering fields, for example by modulating the particle's position [64], or the heating beam [62, 68, 71], and analyze the total intensity with a lock-in amplifier. Alternatively, one can carefully subtract the background by exploiting the frequency- [65], space- or time- dependence of the signal [66, 69]. In practice, all schemes boil down to detecting the interference term, preferably with a tunable phase factor $e^{i\varphi}$ between the two fields:

$$I = \left| E_{ref} + e^{i\varphi} E_{sca} \right|^2 \quad . \tag{1.36}$$

For a discussion of the signal-to-noise ratio in this general interference experiment, we will for sake of simplicity, assume that the particles are small enough to be considered as dipoles. The direct contribution of the scattered intensity ($E_{sca}{}^2$), then becomes negligible, and the detected signal arises only from the interference term $2\,\mathrm{Re}\,(E^*_{ref}\;e^{i\varphi}\,E_{sca})$, whereas the noise is (ideally) limited by the photon noise of the total intensity falling on the detector (i.e. mainly the strong reference intensity), and is proportional to $(E^*_{ref}\,E_{ref})^{1/2}$. Although different methods may differ in practical details (electronic noise, laser noise, dark counts of the detectors, etc.), for the case of ideal optical and electronic components all of them are ultimately limited by photon noise only. In these conditions, the signal-to-noise ratio is immediately seen to be independent of the strength of the reference field, at least as long as this field remains much stronger than the scattered field. Therefore, the possibility to detect a scatterer does not depend on the strength of the reference field. In other words, the reference field may be adjusted in each experiment so as to adapt the measured signal to detectors or to other experimental constraints, without any loss (or gain) of signal-to-noise ratio.

A more quantitative estimate of the maximal signal-to-noise ratio can be given, which depends on the physical origin of the signal. Let us first consider the field directly emitted by the induced dipole itself, which, as we recall, is responsible for the extinction of the incident wave, and, for small particles, mainly arises from absorption processes. The number of absorbed photons N_{abs} during an integration time τ is given by the ratio of the absorption cross-section σ_{abs} to the beam area A at the focus. It has to be compared to the number of incident photons N_{det} that reach the detector and determine the shot-noise. The signal will be visible when it dominates the shot-noise of N_{det}, i.e., when

$$\sigma_{abs} > \frac{A}{\sqrt{N_{det}}}\quad . \tag{1.37}$$

The maximum admissible intensity I_{sat} on the nanoparticle is usually limited by some saturation effect, so that in the best case $N_{det} = A\,I_{sat}\,\tau$. As a comparison, for a single molecule at room temperature, typical values would be $\sigma_{abs} \approx 0.01\ \mathrm{nm}^2$, $I_{sat} \approx 1\ \mathrm{kW\ cm}^{-2}$, which would yield a minimum integration time of about 30 seconds to directly detect the absorption. This should be compared to the typical integration time in single-molecule fluorescence, often shorter than 1 millisecond. In contrast, for a single gold nanoparticle of 10 nm in diameter, $\sigma_{abs} \approx 50\ \mathrm{nm}^2$, $I_{sat} \approx 200\ \mathrm{MW\ cm}^{-2}$ (approximate intensity to melt the particle in condensed matter). Hence, the minimum integration time for detection is theoretically less than a nanosecond. More

practically, the limit for detection by direct absorption (Chapter 4) or by scattering methods [66] currently seems to lie at diameters of about $5 - 10$ nm for reasonable integration times of the order of 10 ms, and reasonable intensities in the order of 1 MW/cm^2.

The case of photothermal detection largely follows the above discussion but for one important difference. The surrounding medium stores the absorbed energy during the heating period, typically 1 microsecond. This results in an accumulated change in refractive index, which varies at the modulation rate, and is then probed by a second beam at a different wavelength, itself detected by a photodiode connected to a lock-in amplifier. In this way, static or slowly fluctuating sources of background scattering are eliminated. Moreover, if the probe wavelength is chosen to lie outside the absorption band, the probing intensity can be very high, leading to a further increase in signal-to-noise ratio. The best achieved result was the detection of gold nanoparticles with diameters down to 1.4 nm with an integration time of 10 ms and an applied intensity of about 5 MW cm^{-2} [71]. A full discussion of the origin of the photothermal contrast and of the signal-to-noise ratio has been given by Berciaud *et al.* [67].

2

Third-harmonic generation

2.1 Introduction

Optical signals from single nano-objects open new windows for studies at
nanometer scales in fields as diverse as material science and cell biology.
Cleared from ensemble averaging, distributions and time-dependent fluc-
tuations stand out. Simpler pictures of molecular processes emerge from
first-hand comparison to theoretical models. Early work has concentrated
on aromatic dye molecules, whose fluorescence can be detected with a very
high signal-to-background ratio [22]. Their applications as labels for single
biomolecules are considerably limited by photobleaching. This irreversible
destruction of the molecule forces the experimentalist to change molecule
and to hark back to statistics, thereby losing part of the advantages of single-
molecule methods. Semiconductor nanocrystals, which resist bleaching for
longer times, have recently been introduced as labels [74]. The random inter-
ruption of their luminescence by long off-times is, however, a serious draw-
back for many applications. Tracking biomolecules requires chemically and
photochemically stable labels, ideally no larger than a few nanometers. Noble
metals, in particular gold, strongly interact with light while being chemically
inert. Because they resist high illumination levels and don't saturate, and be-
cause they can be attached to biomolecules, as is currently done in electron
microscopy, gold nanoparticles would be appealing optical labels.

Being bridges between molecules and solids, metal nanoparticles and col-
loids show fascinating size and confinement effects. Their linear and nonlin-

ear optical properties are the subject of active research [28, 75, 76, 77]. Much of the current work bears on large ensembles of nanoparticles in gas phase, solid matrices, or liquid solutions. In such bulk samples, the properties of interest can be obscured by the distribution of sizes, and in the case of liquid suspensions, by aggregates, which can easily dominate the signal of isolated colloids. The need for small-sized labels has rekindled interest in the photoluminescence of noble metal particles [54, 55, 75]. However, the luminescence yield of all except the smallest metal clusters is weak, and strongly depends on surface states and defects. Therefore, more reliable optical contrast mechanisms are desirable. Scattered laser light enables tracking of gold particles larger than 100 nm in biological media, where a high background arises from other scatterers. Such large labels, however, may hamper the functions of tagged biomolecules in real cells. Interferometric detection of laser heating was recently proposed as a two-color contrast mechanism to image gold nanoparticles as small as a few nanometers [68]. Other nonlinear processes may offer simpler ways to optically detect metal nanoparticles. Multiphoton processes are expected to be amplified by enhanced electric fields within, or in the vicinity of, metal particles, and may provide sufficient contrast against background from the surroundings.

The simplest nonlinear effect, second-harmonic generation (SHG), is forbidden for a perfect spherical particle much smaller than the wavelength. SHG will therefore strongly depend on defects, facets and other small deviations from the spherical shape. It will strongly vary from particle to particle, which is a drawback for labelling. In this chapter, we consider third-harmonic generation (THG, i.e. third-order hyper-Rayleigh scattering), which is allowed in all media, and requires only one pump color. Giving a specific signal for particles of a given size, THG can distinguish labels of different sizes. We have explored the strength of the THG signal of single gold particles in a confocal microscope, in view of its possible combination with THG in bioimaging [6, 78].

2.2   Experimental method

In a THG experiment, we deal with a large spectral difference between fundamental and third harmonic. If the source at the fundamental frequency is a titanium:sapphire laser, for instance, the third harmonic lies in the deep ultraviolet (270 nm), where imaging is difficult and photodetection inefficient. Instead, we chose to use the signal beam of an optical-parametrical oscillator (OPO) at a wavelength of 1500 nm as the fundamental. The Mie frequency
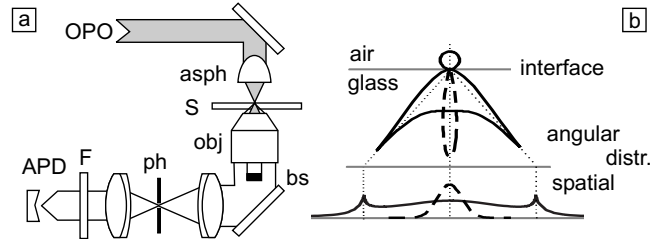
Figure 2.1: a) The central part of the experimental setup. The OPO signal beam (1500 nm) is focused by an aspheric lens **asph** (NA 0.65) on the sample **S**. The generated light is collected by an oil immersion objective **obj** (NA 1.4). The coherent background is suppressed by a beam stop **bs** and a pinhole **ph**. The filter **F** blocks the excitation light. b) Comparison of the angular emission pattern of a dipole (—) and the phase-matched coherent background (- -). The dipole points out of the paper plane.

of gold colloids with diameters lower than 100 nm (about 520–560 nm) is then close to resonance with the third harmonic, thus enhancing its generation [79]. The OPO produces nearly Fourier-limited pulses of about 1.2 ps width at a repetition rate of 76 MHz. This light is coupled into a home-built microscope (Fig. 2.1a). The sample is scanned by a piezo stage through the overlapping foci of an aspheric lens (excitation) and an oil immersion objective (detection). This way, both excitation and detection benefit from efficient optics. A confocal pinhole reduces the detection volume and a band-pass filter (510 ± 20 nm) allows only the third harmonic to reach the avalanche photodiode. The detection rate is recorded as a function of the position of the scanning piezo stage.

The samples are gold colloids (British Biocell International, EM.GC) of different diameters d (40, 50, 60, 80, 100, and 150 nm) spin-coated in a polymer solution (polyvinyl-alcohol, PVA, 10 g/l) on a clean glass cover slide. Special care was taken to avoid changes in the ionic strength of the solution which may cause aggregation of the colloids. We imaged mono-disperse samples and mixtures of two different diameters where the larger particles (100 or 150 nm) served as references.

Bulk THG cancels for a focused beam in massive materials because of the Gouy phase shift on both sides of the focus, but it still takes place in the vicinity of interfaces [80]. This background, which is several orders of magnitude higher than the THG from gold colloids, can be dramatically suppressed by exploiting the difference in angular THG emission patterns of the interface and of a single colloid (Fig. 2.1b). The interface THG-beam is created in a

coherent process in the direction of the exciting beam with one third of its numerical aperture (NA) [80]. The THG pattern from a colloid can be approximated by that of a dipole at the interface [81]. When the THG-beam is collimated by a high-NA objective, the outer parts of the parallel beam are dominated by colloid THG, and the interface THG can be blocked by a beam-stop in the center. In our case a beam-stop of 3.2 mm diameter transmits only about 10^{-5} of the interface THG but about 75 % of the colloid THG. This simple device reduced the coherent background THG below the dark count rate of the detector (40 cps).

2.3   Single gold nanoparticles
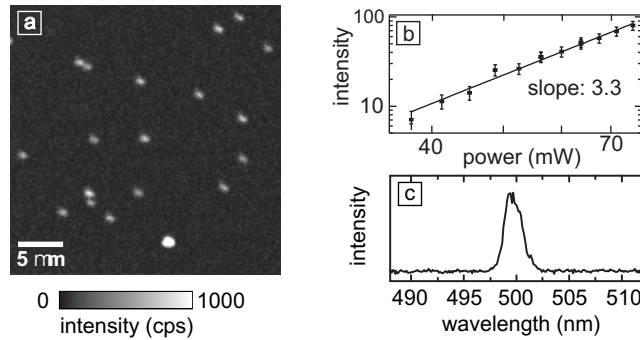
Figure 2.2: a) Raster-scanned image of colloids ($d = 100$ nm), 100 ms/pixel integration time, 75 mW excitation power; b) Excitation power dependence of the detected THG signal, measured on a single 100-nm colloid by fitting a 2D Gaussian to series of scans; c) Emission spectrum of a single 100-nm colloid. The full width at half maximum of the peak is 2 nm.

Figure 2.2a shows a 30×30 μm raster scan of a sample obtained by spin-coating a solution of 100-nm colloids. In this image, several peaks with approximately the same height can be discerned. The signal shows clear signatures of third-harmonic generation: the emitted intensity has a third-power dependence on the excitation intensity (Fig. 2.2b) and the spectrum consists of a single narrow line (FWHM of 2 nm) centered around 500 nm, corresponding to three times the fundamental frequency (Fig. 2.2c). The time-dependence of the THG signal is constant over very long intervals, as shown the bottom panel of Fig. 2.3a. Outside the filter passband, the only detected emission is a second line centered around 750 nm, at twice the fundamental frequency (i.e., the second harmonic). As mentioned in the introduction, the
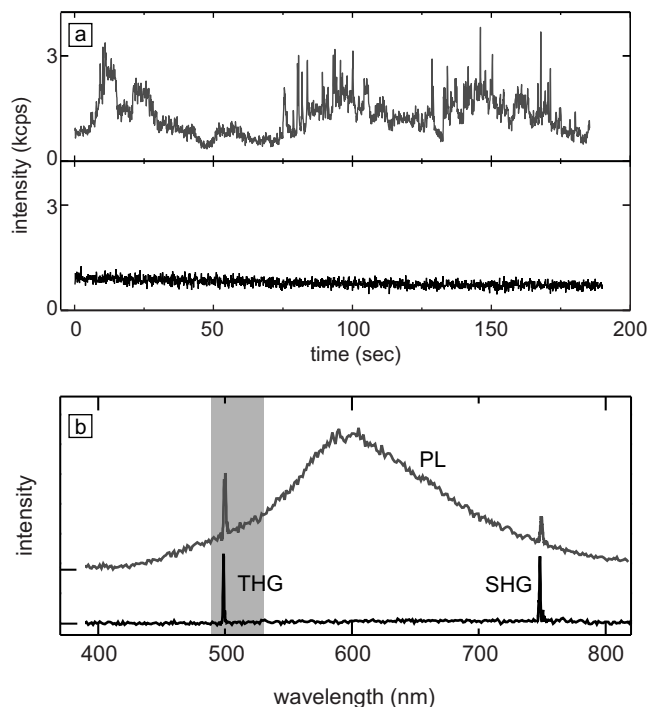
Figure 2.3: a) Time traces of two single 100-nm colloids; b) Emission spectra corresponding to the same two colloids. All colloids show THG and SHG, a small fraction of the colloids additionally show photoluminescence (PL, upper spectrum in b)) with a very irregular time dependence (upper timetrace in a)). Note the difference in SHG intensity between the two spectra, which points to the sensitivity of this signal to defects.

SHG line can be explained by defects in the colloid (e.g. deviations form a perfect sphere) or by an environment-broken symmetry (e.g., due to the air-glass interface). Since this line fell outside our detection window, it did not contribute to the confocal image (Fig. 2.3c, bottom spectrum).

The spot in the bottom center of Fig. 2.2a is much brighter than the others (it is saturated in the gray scale of Fig. 2.2a). Such "hot" colloids could be identified in the images by their high intensity. As can be seen at the top of Fig. 2.3b, the spectrum of a hot colloid contains, in addition to the THG and SHG lines, a broad peak centered around 600 nm, with a much higher integrated intensity. This photoluminescence spectrum has been previously observed under two-photon excitation by Beversluis et al. [53]. Most hot colloids presented extremely bright flares over microseconds to milliseconds (Fig. 2.3a), covering a large range of intensities (flickering), but we never
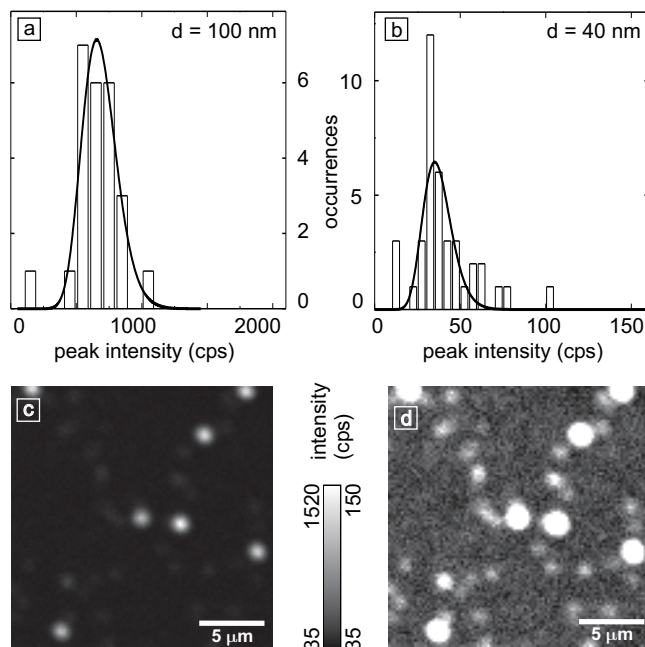
Figure 2.4: a,b) Histograms of the peak intensities above background for a pure 100-nm sample (a) and the 40-nm colloids of a mixed sample (b). The fit yields a relative diameter distribution $\Delta d / d$ of 7 % (100 nm) and 8 % (40 nm) which agree with the manufacturer's values (5 % and 6 %). c,d) Raster-scanned image of a mixture of 40-nm and 100-nm gold colloids (600 ms integration time). The same scan is shown with two different intensity scalings. In (d) the 100-nm colloids are saturated, but the 40-nm colloids appear above the background.

observed the clear on-off blinking of single molecules and nanocrystals. The hot colloids (in total 2 %) were left out of the THG analysis that follows.

Histograms of peak intensities of the THG from normal colloids were extracted from images in the following way. We filtered a copy of each image with a Gaussian correlation filter. All pixels above a certain threshold (70 cps) were found to cluster in spots. At these positions we fitted a Gaussian intensity distribution to the unfiltered data. We thus ended up with histograms of spot intensities above the background level. Two examples are shown in Fig. 2.4a and b. All the histograms show a monomodal Gaussian distribution with a significant offset from the background. This feature unambiguously discriminates a distribution of single objects from a distribution of aggregates with different sizes. The spots that fall into the lowest bins of each histogram are attributed to specks of dust or fluctuations in the background level that

triggered the fitting procedure. The histograms can be fitted assuming a normal size distribution and the size dependence discussed below. The resulting relative width $\Delta d/d$ matches the values of the manufacturer's test certificate. Fig. 2.4c and d shows the same scan of a 40 and 100-nm mixture in two different intensity gray scales. In Fig. 2.4d the 40-nm colloids appear above the background. This diameter of 40 nm was our detection limit (at 600 ms integration time) with a fundamental average intensity of 2 MW/cm^2 (peak intensity of 40 GW/cm^2), which was limited by OPO output.
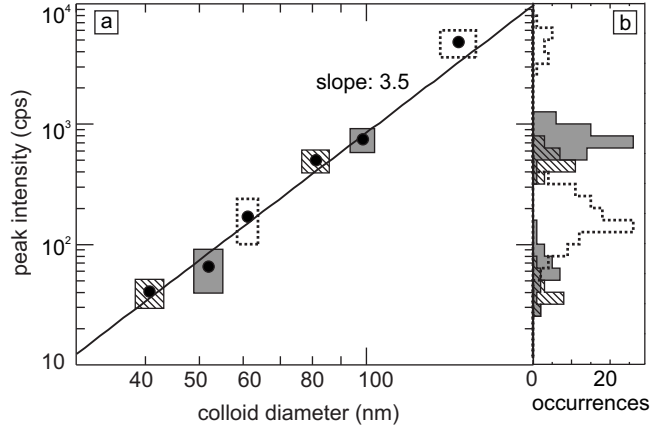
2.4 Size dependence

With increasing particle size, the third-harmonic signal increases as the square of the induced nonlinear dipole, which, for a cluster of independent molecules, would increase as their number. Thus, when the nonlinear susceptibility originates from *bound* electrons and is therefore a molecular, size-independent property, we expect a sixth-power dependence of the THG intensity on cluster diameter. Fig. 2.5 shows the average signal intensity for 6 sizes of particles, from 40 nm to 150 nm. The slope of the plot across the whole range is compatible with a third- to fourth-power dependence in diameter, and clearly deviates from a sixth power (for which the ratio of 40 nm to 150 nm colloid signal should be 14 times lower).

A metal's *free* electrons can lead to a size-dependent susceptibility. In an infinite metal bulk, free electrons perform exactly harmonic plasma oscillations. In nanoparticles, however, finite size and surfaces give rise to anharmonicity. Recently, Fomichev et al. [79, 82] have theoretically considered THG by plasma oscillations in a small conducting sphere, when the third harmonic is resonant with the plasmon frequency. For a neutral particle at high intensity, they predict a significant production of third harmonic, and a fourth-power dependence of the intensity on diameter. Their calculation is based on the slight deviation from a harmonic potential that the electron charge distribution experiences when it oscillates as a whole around the fixed ion distribution. In this model, THG can be seen as induced by the surface of the sphere. The induced dipole is therefore proportional to the area of the sphere rather than to its volume. This leads to a third-harmonic intensity varying as the fourth power of the diameter. The signal intensity we measure, taking our collection efficiency into account, is in good order-of-magnitude agreement with the formula of Ref. [79] for neutral particles, although we are in a regime of much lower intensities.

Note, however, that retardation effects lead to a significant change in the

Figure 2.5: a) Size dependence of the THG signal of single gold colloids: mean values (black dots) of the obtained histograms shown in part (b). The boxes represent the error bars: The intensity error is estimated by the histogram standard deviation and the size error is the width of the size distribution as given in the manufacturer's test certificate. The data was fitted with a power law (black line). To correct for thermal drifts, the colloid samples were mixed with 100-nm colloids, used as references (150-nm colloids were taken as references for the 80-nm colloids). The excitation power was 68 mW, the integration time was 100 ms (600 ms for the 40-nm colloids).

absorption spectrum for colloids larger than about 50 nm. This gives an additional size-dependent factor in both the bound-electron and the free-electron model, which is difficult to estimate. The accurate calculation of the influence of retardation on the third-harmonic generation is computationally demanding and has, to our knowledge, only be done for the bound-electron case [83]. It is therefore desirable to measure THG from yet smaller individual colloids, where retardation is negligible. The 1-ps pulses of our current laser system limited us to 40-nm particles. With the 100-fs pulses of current commercial OPO's, and assuming the fourth-power to hold on for lower sizes, we estimate a signal-to-noise ratio of more than unity for 15-nm particles, with the present accumulation time of 600 ms.

2.5   Conclusion

We have demonstrated that single gold nanoparticles can be detected by third-harmonic generation. Peak-height histograms show that each spot in the image is produced by a single particle. In the present setup colloid sizes down to 40 nm are detectable, but the use of 100-fs pulses should allow us to

image 15 nm particles. Even if this limit would be hard to reach in a scattering medium such as a cell, and smaller labels can be detected with photothermal heterodyne detection [84], single particle spectroscopy through THG can be advantageous when combined with THG imaging [6]. The size-dependence of the THG signal would make it possible to distinguish labels of different sizes. Gold nanorods (elongated particles) might further increase the signal to volume ratio of the particles [77]. However, the absorption of water at 1500 nm must be taken into account for biological samples. In order to avoid attenuation of the fundamental power and heating problems, the sample thickness should not exceed some tens of micrometers, about the size of a cell.

3

Characterization of a common-path interferometer

3.1 Introduction

For the last 15 years, single-molecule spectroscopy has mainly focused on luminescence studies of fluorescent molecules and semiconductor nanocrystals [22]. In the last few years, however, ever increasing interest in the properties and applications of metal nanoparticles (nanospheres, nanorods, etc., with sizes between 1 and 100 nm) has stimulated the development of various optical detection schemes for single metal nanoparticles.

An attractive characteristic of gold nanoparticles is their high photostability. Unlike dyes or semiconductor nanocrystals, gold particles do not suffer from photobleaching or photoblinking, which makes them appealing labels for biophysicists [85]. Another strong motivation is the study of original physical properties of metal nanoparticles, that often differ from those of the bulk metal, and to a large extent can be tuned through the size and shape of the nanoparticle. This sensitivity to size and shape makes studies of ensembles of nanoparticles particularly vulnerable to distributions in sizes, shapes, crystal defects, etcetera. Isolating a single particle once and for all eliminates inhomogeneous broadening and any implicit averaging inherent to even the most carefully selected ensembles. Only single-particle experiments permit to study a particle's elastic interaction with its specific close environment [62], to correlate optical and structural properties [86], or to obtain new insight in

their linear and nonlinear optical properties [60, 61, 57].

The number of available methods for the detection of single metal nanoparticles has grown rapidly in the last few years [87]. Of all these methods, interferometric detection of the scattered field seems very promising, mainly because the interferometric signal drops as the third power of the particle size only, whereas the direct scattering signal drops as the sixth power, but also for the possibility to detect the full complex response of a nanoparticle [62, 88]. In all interferometric experiments, the field scattered by a single metal nanoparticle is mixed with a reference field, but the methods differ in their choices for the reference and scattered field [89]. Using the incident wave itself as a reference, one basically measures absorption [64]. Alternatively, the reference wave can be the reflection from the substrate on which the particle has been deposited [66], or an external reflection in a Michelson interferometer [69]. The signal wave can be either directly scattered by the particle, or indirectly scattered from a local inhomogeneity of refractive index, for example induced by heat released by the excited particle into its surroundings, as done in the photothermal method [68, 71]. We have used a common-path interferometer to measure the time-resolved response of single gold nanoparticles down to a 10-nm diameter [62]. This sensitive technique allowed us to detect acoustic vibrations of single gold nanoparticles as small as 40 nm. This chapter gives a detailed description and a characterization of the interferometer. In chapter 4, results on single gold nanoparticles are presented.

In our common-path interferometer, probe and reference arms are spatially overlapped (in contrast to, for example, Michelson and Mach-Zehnder interferometers [37]). The interfering waves are distinguished on the basis of both polarization and time, although any single one of these characteristics would in principle suffice. Temporal separations can be created via a relative delay between laser pulses, as done here, or via a small phase shift between two CW beams, as for example in phase-contrast microscopy [90], or by counter propagation in a Sagnac ring interferometer, as was recently implemented by Hwang et al. [91], for the phase-sensitive detection of very weak absorbers. The first implementation of a common-path interferometer in combination with pulsed laser sources was published by LaGasse et al. [92] in an optical switching experiment. In this experiment, the probe pulse was delayed by means of polarizing beam splitters and mirrors. Patel et al. [93] have built a number of logical elements by using the same technique, but with a birefringent fiber as a delay medium. Hurley and Wright [94] constructed a common-path interferometer based on a Sagnac interferome-

ter, also using diversion through polarizing beam splitters to split a pulse into probe and reference. Polarization analysis allowed them to separately detect pump-induced changes in reflectivity and phase. Using this method, the same group were able to image the progression of pump-induced acoustic waves along a surface [95, 96].

We also rely on a polarization-induced delay between a probe pulse and a reference pulse, but we use a birefringent crystal as beamsplitter. The main advantage of this element is its simplicity and ease of alignment, which leads to a high contrast of the interference pattern. The delay between the interfering wavetrains in combination with a pump-probe configuration allows us to obtain information on ultrafast properties of the nanoparticles, and the high sensitivity and low noise floor enables experiments on single nanoparticles. By choosing the proper configuration for the polarization optics of our interferometer, we can separate the detection of amplitude and phase changes induced by a single nanoparticle on the probe pulse, and measure the full complex response of the particle. Although we used our interferometer only for gold nanoparticles so far, the method is in principle applicable to any absorbing and/or dispersing nano-object.

3.2 Description of the setup

We have designed a polarization-based common-path interferometer that uses two birefringent crystals to split and recombine the probe and reference waves [62]. A sketch of the setup is shown in Fig. 3.1. A laser pulse that is initially polarized at 45 degrees from vertical is split into two orthogonal polarization directions by the first calcite crystal, whose fast optical axis is vertical. Propagation in the thick (15 mm) birefringent crystal delays one of the two polarized waves by a time longer than the pulse length. This effectively creates two pulses, a probe and a reference, which are orthogonally polarized and have a mutual delay of 10 ps. These pulses interact with the sample (a glass coverslide on which nanoparticles are spincoated) in the microscope.

Behind the microscope, probe and reference are recombined by a second crystal, identical to the first one but oriented perpendicularly, its fast axis now being horizontal. With an analyzer assembly of a quarter-wave plate and a polarizer, the recombined waves are projected onto the same polarization state and interfere. Independently rotating the quarter-wave plate and the polarizer allows us to tune the relative contributions of the phase and amplitude of the probe and reference waves. The interference reports on changes of the sample over the time interval between the probe and the
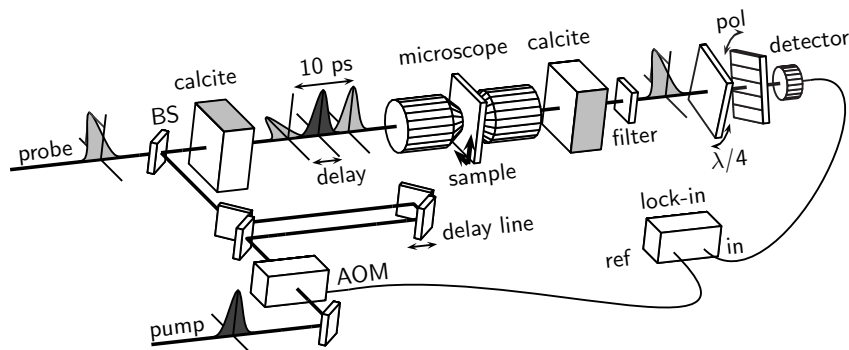
Figure 3.1: Schematic drawing of the pump-probe common-path interferometer. A pump pulse and a pair of reference and probe pulses are focused on the sample in a microscope. The reference-probe pulses arise from a single pulse, split in time (10 ps delay) and polarization by a properly oriented birefringent calcite crystal. The delay between the pump pulse and the reference-probe pair can be scanned with a delay line. After the microscope, probe and reference are recombined by a second crystal and their interference monitors pump-induced changes in the optical properties of the sample. A quarter-wave plate ($\lambda/4$) and a polarizer (pol) are independently rotated to set the working point of the interferometer. The other details are described in the text.

reference pulses. In order to generate and accumulate the signal, we induce a change of the sample by means of a separate laser pulse, in a pump-probe configuration. This pump pulse (from a synchronous second laser source) is intensity-modulated by an acoustic-optical modulator (AOM) and travels over a variable delay line, before it is overlapped by a dichroic beam splitter (BS) with the probe beam. Dichroic filters efficiently prevent pump light from reaching the detector. By varying the delay between the pump pulse and the pair of probe and reference pulses, we can measure the ultrafast dynamics of our sample.

Let us schematically describe the working of the ideal interferometer with proper settings of the analyzer assembly. If the sample does neither modify the phase nor the amplitude of the probe with respect to those of the reference (e.g., if the pump laser is switched off, or if there is no particle in the laser focus), the polarization state after recombination is again linear, rotated by 45 degrees from the vertical. If we now switch on the pump laser while a nanoparticle sits in the common focus of the two laser beams, a small change in the phase and/or amplitude of the probe pulse will modify the polarization state after recombination, giving rise to a slightly elliptical and/or ro-

tated linear polarization. This changes the transmission through the analyzer assembly. The change in polarization state is thus translated into a change of intensity at the detector, which we can measure with a lock-in amplifier synchronized with the pump's modulation.

With the quarter-wave plate and the polarizer, we can tune the fraction of the light that reaches the detector. If the quarter-wave plate has one of its optical axes parallel to the polarization direction of the incoming light, and if the polarizer is perpendicular to the incoming polarization, the detected intensity is minimized, and the interferometer is in a dark fringe. By rotating the polarizer by 90 degrees, we find a bright fringe, where the detected intensity has a maximum. Besides tuning the fraction of probe light that reaches the detector, we can also use the quarter-wave plate and the polarizer to select a working point where either phase or amplitude modifications of the probe field by the sample can be detected, independently from each other. If quarter-wave plate and polarizer are rotated in such a way that the amplitudes of the interfering fields are equal, but the phases are different, the interference term will only report on phase changes of the probe – assuming small changes to the fields as it is the case with nanoparticles. Conversely, if the polarizer and the quarter-wave plate are tuned so that the amplitudes are different while the phases are the same, the interferometer only senses amplitude changes of the probe, while phase changes remain unnoticed. The precise orientations of the polarizer and the quarter-wave plate for which the interferometer is either purely amplitude-sensitive or purely phase-sensitive are calculated in section 3.3 using a model based on Jones matrices.

Key features of our interferometer are the birefringent crystals for temporal beam splitting and recombination. Although they have the disadvantage that the delay between the probe and the reference pulse is fixed, the alignment becomes much easier, since it is not necessary to align the overlap of the spatial paths of the two interferometer arms. This considerably improves the visibility of the interferometric fringes. The crystals are 15-mm thick calcite crystals, cut from the same slab to make them as alike as possible. In order to keep the operation of the interferometer stable, we had to actively stabilize the temperature difference between the two crystals. No special temperature or mechanical stabilization is needed for the other elements in the beam path as they affect probe and reference in exactly the same manner.

If there is a small difference between the optical path lengths through the crystals, either because of a difference in orientation, temperature, or because of a difference in thickness (the crystals are specified to be equally thick to within 1 μm), we will have to allow for a static change in the polarization

state of the probe beam after recombination. Instead of being linear at 45 degrees, the recombined beam can be elliptically polarized with a rotated axis, even when the pump is off. A second static effect that must be taken into account is a residual difference in the transmissions of the vertical and horizontal polarizations by the microscope. These two effects change the orientations of the quarter-wave plate and the polarizer at the dark fringe, and the settings of the phase-sensitive and amplitude-sensitive working points. These experimental imperfections, however, can be included into the model of section 3.3. By measuring them, we can determine and compensate for their influence on the response of the interferometer. The quality of an interferometer can be characterized by its contrast ratio I_{max}/I_{min}. It can be shown that the previous effects, if properly compensated for, do not reduce the contrast. The contrast ratio is in fact limited by other imperfections of the optical elements, such as depolarization by the microscope objectives.

To generate our probe beam, we start with the signal beam of an OPO (APE, Berlin) synchronously pumped by a Ti:Sapphire laser (Coherent Mira 900D) at a repetition rate of 76 MHz. The signal beam is frequency-doubled in the OPO cavity. The resulting pulses are nearly Fourier-limited and are tunable in wavelength between 520 and 650 nm. The Ti:Sapphire laser is operated at 800 nm, and pumped by a CW frequency-doubled Nd:YAG laser (Coherent Verdi V10, 10 W, 532 nm). The laser system can be aligned to produce pulse lengths either in the picosecond or in the femtosecond range. The pulse lengths (full width at half maximum of the autocorrelation function) at the output of the laser of the Ti:Sapphire laser and the OPO are approximately 3 ps and 1.5 ps in the picosecond configuration and 120 fs and 250 fs in the femtosecond configuration.

A small part of the Ti:Sapphire laser beam, split off before entering the OPO, serves as the pump in the experiment. The pump beam travels over a variable delay stage to tune its time of arrival with respect to that of the probe-reference pair (see Fig. 3.1). The pump beam is combined with the probe beam by a dichroic beam splitter before the first crystal. The pump polarization is kept parallel to one of the optical axes of the crystal, to ensure that this pulse is not split. After the objectives, the residual pump light is filtered out by optical bandpass filters.

The home-built microscope consists of two objectives, an oil-immersion objective (NA 1.4) for excitation and an air-spaced objective (NA 0.95) for collection. The sample is mounted on a piezo-electric stage and can be scanned with 25-nm precision. For some of the characterization experiments, we used single gold nanoparticles as a model system. For these experiments, we

used commercial gold nanoparticles (purchased from British Biocell International and Sigma-Aldrich and used without further treatment), dispersed in a 10 mg/ml aqueous solution of polyvinyl alcohol This suspension was spin-coated onto a clean glass microscope cover slide. The cover slides were cleaned by subsequently sonicating them 10 minutes in a KOH solution, rinsing and sonicating 5 minutes in water and incubating 5 minutes in acetone. After that the slides were rinsed with water once more and then dried and stored. Prior to spincoating the glass slides were cleaned in an ozone cleaner for 5 minutes.

Our detector is an analog Silicon APD (Hamamatsu C5331-11), which is sensitive for signals modulated at frequencies between 4 kHz and 100 MHz. The smallest optical signal that can be detected against electronic noise, called the noise-equivalent power (NEP), is specified between 0.5 and 1 pW/$\sqrt{\text{Hz}}$. The detector signal is fed into a lock-in amplifier (Stanford SR844), whose internal clock drives an acousto-optical modulator (AOM) in the pump path at 400 kHz. To prevent overload of the lock-in from the 76 MHz signal of the laser pulses, the signal from the detector is pre-filtered with a passive 12 MHz low-pass filter.

Note that although we only describe a transmission configuration for the interferometer here, it is in principle also possible to apply our method to reflection measurements. In that case, only one calcite crystal is necessary, but a quarter-wave plate has to be introduced between the crystal and the microscope to ensure that the pulses are recombined when travelling through the crystal in the backward direction.

3.3 Model of the interferometer

We model our interferometer by representing each element by a Jones matrix. In this way, we obtain analytical expressions for the intensity at the detector and for the measured signal, as functions of the angles of the quarter-wave plate ϕ and of the polarizer θ (see Fig. 3.1). We calculate the contribution to our signal of real and imaginary changes in the electric field of the probe for each θ and ϕ and calculate for which combination of angles we can measure the real and imaginary changes separately.

From Fig. 3.1, we write all elements of the interferometer as Jones matrices. Matrix multiplication of the elements with the incoming probe field will yield the electric field and subsequently the intensity at the detector.

The input wave is polarized at -45 degrees, $E_{in} = \sqrt{1/2}\,(1, -1)$, and is split into a horizontally polarized reference wave, which travels in front, and

a vertically polarized probe. The absorption of the pump pulse by the particle triggers a small time-varying modification $\zeta(t)$ in the fields transmitted though the microscope. The modification ζ is complex-valued, allowing for changes in amplitude and phase of the fields. The temporal zero is the arrival of the pump pulse at the sample. Reference and probe pulses are orthogonally polarized on each other and delayed by 10 ps. After recombination, the Jones matrix associated with the particle can be written as

$$\mathbf{P} = \begin{pmatrix} 1 + \zeta_H(t - 10\text{ps}) & 0 \\ 0 & 1 + \zeta'_V(t) \end{pmatrix} \quad . \tag{3.1}$$

Shape and orientation of the particle are *a priori* unknown, and a difference in particle response in the horizontal and vertical direction has to be taken into account, and is here indicated with the indices H and V. Also, the field of the reference pulse might alter the state of the particle, which changes the particle response to the probe pulse from $\zeta(t)$ to $\zeta'(t)$. Including these two effects would however lead to more parameters than are solvable, so we assume for now that the particle is symmetric for the horizontal and vertical direction (so either spherical, or spheroid with the two equal axes in the x-y plane), and that we are in a linear-response regime, where the state of the particle is not affected by the field of the reference pulse. We can now write, instead of Eq. (3.1),

$$\mathbf{P} = \begin{pmatrix} 1 + \zeta(t - 10\text{ ps}) & 0 \\ 0 & 1 + \zeta(t) \end{pmatrix} \approx \begin{pmatrix} 1 & 0 \\ 0 & 1 + \Delta\zeta(t) \end{pmatrix} \quad , \tag{3.2}$$

where $\Delta\zeta(t) = \zeta(t) - \zeta(t - 10\text{ ps})$ is the 10-ps difference in the pump-induced modification of the field. The approximation is exact for $t < 10$ ps as then $\zeta(t - 10\text{ ps}) = 0$, and introduces only small errors for working points of the interferometer close to the dark fringe for all other delays t.

As was already mentioned in section 3.2, it is important to consider a difference in optical path length through both crystals and a difference in transmission of probe and reference through the microscope. The former effect manifests itself as an additional wave plate in the optical path, while the latter can be modelled with a relative decrease in amplitude of one of the two arms. In the model, we can combine both effects in one matrix $\mathbf{D}$, which adds two additional parameters, ρ for the difference in transmission between the two polarizations (dichroism), and τ for the optical-path difference:

$$\mathbf{D}(\rho, \tau) = \frac{1}{1 + (1 - \rho)^2} \begin{pmatrix} 1 & 0 \\ 0 & (1 - \rho)\, e^{i\tau} \end{pmatrix} \quad . \tag{3.3}$$

The prefactor is introduced for normalization of the bright fringe intensity. ρ and τ can be determined experimentally, since a change in either of them causes the dark fringe of the interferometer to deviate from its original position $(\theta, \phi) = (45°, 45°)$. Therefore, by measuring the actual position of the dark fringe, the two calibration parameters ρ and τ can be calculated.

The Jones matrices of a quarter-wave plate **Q** and of a polarizer **L** oriented at an arbitrary angle are found by multiplying the Jones matrices for the elements at 0 degrees [97] by rotation matrices:

$$\mathbf{Q}(\phi) = \frac{1}{\sqrt{2}} \begin{pmatrix} 1 + i\cos(2\phi) & i\sin(2\phi) \\ i\sin(2\phi) & 1 - i\cos(2\phi) \end{pmatrix} \quad, \tag{3.4}$$

$$\mathbf{L}(\theta) = \frac{1}{2} \begin{pmatrix} 1 + \cos(2\theta) & \sin(2\theta) \\ \sin(2\theta) & 1 - \cos(2\theta) \end{pmatrix} \quad. \tag{3.5}$$

The combined action of the elements in Eqs. (3.2) to (3.5) on the incoming wave E_{in} now gives the electric field and the intensity of the probe beam at the detector:

$$\mathbf{E}_{\text{det}}(\theta, \phi, \rho, \tau, \Delta\zeta) = \mathbf{L}(\theta) \cdot \mathbf{Q}(\phi) \cdot \mathbf{D}(\rho, \tau) \cdot \mathbf{P}(\Delta\zeta) \cdot \mathbf{E}_{in} \quad, \tag{3.6}$$

$$I_{\text{det}}(\theta, \phi, \rho, \tau, \Delta\zeta) = |\mathbf{E}_{\text{det}}(\theta, \phi, \rho, \tau, \Delta\zeta)|^2 \quad. \tag{3.7}$$
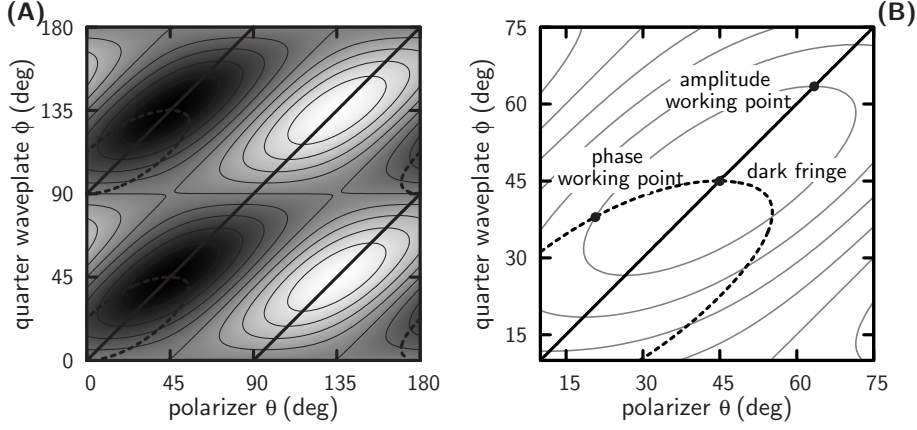
A contour plot of the detected intensity I_{det} as a function of θ and ϕ with $\rho = 0$, $\tau = 0$ and $\Delta\zeta = 0$ is given in Fig. 3.2. The intensity has a minimum (dark fringe) for $(\theta, \phi) = (45°, 45°)$, increases outwards in an elliptical shape, and at $(\theta, \phi) = (45°, 135°)$ we find a bright fringe.

Essentially, with a lock-in amplifier, we subtract the detected intensity of the probe beam when the pump is off from the detected intensity when the pump is on, which gives a signal of

$$S(\theta, \phi, \rho, \tau, \Delta\zeta) = I_{\text{det}}(\theta, \phi, \rho, \tau, \Delta\zeta) - I_{\text{det}}(\theta, \phi, \rho, \tau, 0) \quad. \tag{3.8}$$

In general, for a given value of θ and ϕ, there will be both a contribution from the real and imaginary part of $\Delta\zeta$ to the signal in Eq. (3.11), corresponding to amplitude and phase changes of the field, respectively. They cannot be detected separately, except for configurations where either the amplitude contribution or the phase contribution is zero. For these working points, the detected signal will consist of either the pure phase contribution, or the pure amplitude contribution. In the following we call amplitude working point a configuration of the interferometer which is *not* sensitive to a phase change in the field. All these amplitude working points form a line which we will

Figure 3.2: (A) Contour plot of the intensity at the detector as a function of the angle of the quarter-wave plate and the polarizer, showing bright and dark fringes. On the thick lines, the interferometer is sensitive to either amplitude changes only (solid) or phase changes only (dashed). (B) Magnification around a dark fringe, additionally showing two working points of the interferometer where to detect pure amplitude or phase signals.

call amplitude line. It is the zero contour of the response to a phase change, i.e. imaginary $\Delta\zeta$ in Eq. (3.11). In the same way, a phase working point is a configuration of the interferometer which is not sensitive to an amplitude change of the field. The amplitude and phase lines are shown in Fig. 3.2.

Our model is fully analytical, and is in principle exact for a weak enough probe pulse. It gives the measured signal in terms of θ, ϕ, ρ, τ, and $\Delta\zeta$, but this expression is too lengthy for a qualitative discussion. Instead, we will give a first-order expansion in θ and ϕ around the dark fringe, which provides an illustrative explanation of the working of the interferometer and of the separation of phase and amplitude.

From Fig. 3.2A we see that the interferometer is in the dark fringe if the quarter-wave plate's fast axis and the polarizer's transmission axis are both oriented at +45 degrees. For a first order approximation, we only consider small deviations from the dark fringe: $\hat{\theta} = \theta - \frac{\pi}{4}$ and $\hat{\phi} = \phi - \frac{\pi}{4}$. Using the small-angle approximation, neglecting all higher-order terms of $\hat{\theta}$ and $\hat{\phi}$, and disregarding the experimental correction parameters ρ and τ, we find the total intensity at the detector

$$I_{\text{det}} = |\mathbf{E}_{\text{det}}|^2 = \left(\hat{\theta} - \hat{\phi} - \frac{\text{Im}(\Delta\zeta)}{2} \right)^2 + \left(\hat{\phi} + \frac{\text{Re}(\Delta\zeta)}{2} \right)^2 \quad , \qquad (3.9)$$

while the intensity at the detector without the pump ($\Delta\zeta = 0$) is

$$I_0 = (\hat{\theta} - \hat{\phi})^2 + \hat{\phi}^2 \quad . \tag{3.10}$$

We thus find our signal, which is the first-order change in intensity

$$S = I_{\text{det}} - I_0 = \hat{\phi}\,\text{Re}(\Delta\zeta) - (\hat{\theta} - \hat{\phi})\,\text{Im}(\Delta\zeta) \quad . \tag{3.11}$$

From Eq. (3.11) it is easy to see that amplitude and phase responses can be separated by choosing proper angles for the polarizer and the quarter-wave plate. If $\hat{\theta}$ and $\hat{\phi}$ are equal and nonzero, the interferometer is sensitive for amplitude changes only, while if $\hat{\phi} = 0$ and $\hat{\theta} \neq 0$, the interferometer only measures phase changes. Fig. 3.2B shows that this first-order approximation still applies for the amplitude line even for large angles, while the phase line follows by $\hat{\phi} = 0$ only very close to the dark fringe.

3.4 Results and discussion

3.4.1 Characterization of the interferometer

The contrast ratio of the interferometer (I_{max}/I_{min}), found by rotating the polarizer by 360 degrees as shown in Fig. 3.3A, reaches 150 in the case shown here and varies typically between 100 and 200. This corresponds to a fringe visibility (defined as $(I_{max} - I_{min})/(I_{max} + I_{min})$) between 98% and 99%. The contrast is mainly limited by depolarization by the microscope objectives and by the quality of the crystal surfaces. Nevertheless, due to the simplified alignment of the crystals, the fringe visibility is high compared with other implementations of interferometric microscopes (90% ref. [96], 66% ref. [91]). As expected, the model describes the position of the equal-intensity contours, as shown in Fig. 3.3B for the 10% contour line.

The detection path was calibrated by a laser beam square-modulated at the lock-in reference frequency. In the following we give, if not otherwise mentioned, the root-mean-squared (rms) values of the pump-induced square modulation to our probe beam. To be independent of the absolute probe power, we normalize the detected intensity modulation ΔI to the intensity of the bright fringe I_{bright}. For a constant relative change in the probe field $\Delta\zeta$, the measured and calculated intensity changes ΔI depend on the working point as plotted in Fig. 3.3C and D . In order to calibrate $\Delta\zeta$, we notice that at half-fringe on the amplitude line the reference is fully blocked, and $\Delta\zeta = \Delta I/I_{bright}$.
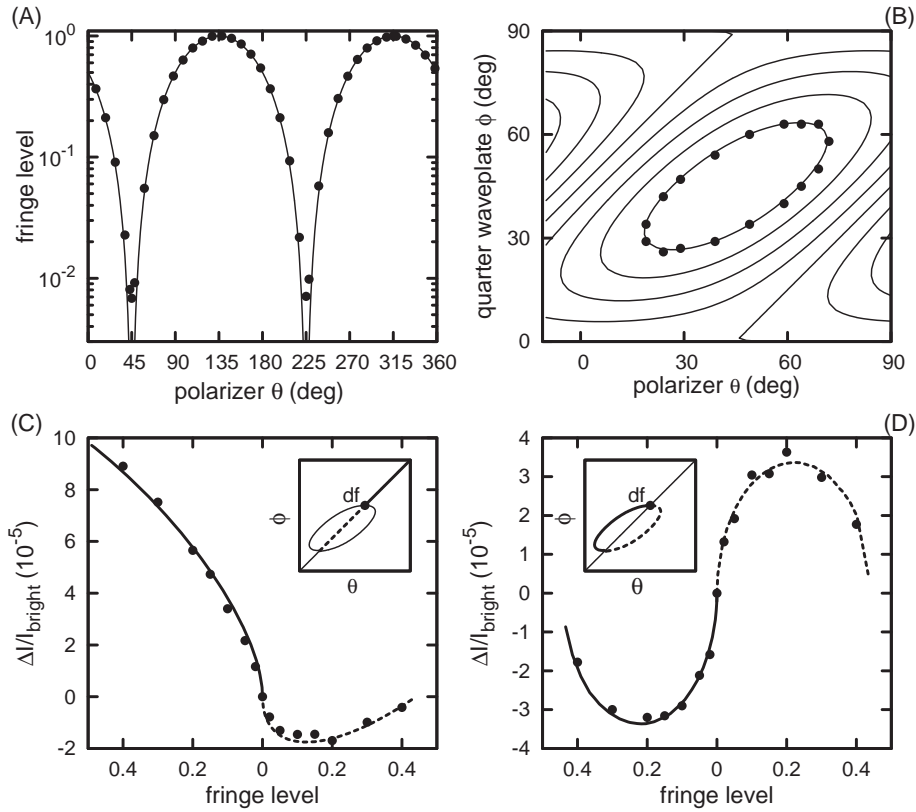
Figure 3.3: (A) The contrast ratio of the interferometer amounts to 150 as measured by scanning the polarizer angle (dots). The model (line) assumes infinite contrast, i.e. an absolute zero at the dark fringe. (B) The position of the 10%-fringe (dots) is well described by our model (intensity contour lines in steps of 0.1). (C, D) Signal from a single 60-nm gold nanoparticle, measured along the amplitude working line (C) and along the phase working line (D). The lines are the signals as calculated by the model assuming $\Delta\zeta = (9.3 - 10.2\,i)\,10^{-5}$. The insets depict the corresponding positions of the polarizer (θ) and the quarter-wave plate (ϕ) relative to the dark fringe (df). The measurement in panel (B) was carried out in the picosecond configuration.
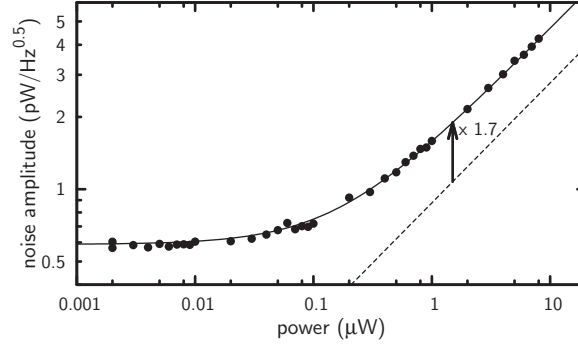
Figure 3.4: Noise amplitude as a function of the optical power at the detector. The solid line is a fit to Eq. (3.13), with $\sigma_{ampl} = 0.6 \, \text{pW}/\sqrt{\text{Hz}}$, $n_{laser} = 0$, and $F = 3 \approx 1.7^2$. The dashed line describes the expected photon noise scaling as the square-root of the probe power. The difference is due to the excess noise of the avalanche process in the analog detector. This experiment was carried out in the picosecond configuration.

Fig. 3.3C and D compare the detected intensity modulation as a function of the interferometer fringe level for working points on the amplitude (Fig. 3.3C) and phase line (Fig. 3.3D). The probe modulation was caused by a single 60-nm gold particle in the focus under constant pump. The data is well described by our model with a pump-induced field modification of $\Delta\zeta = (9.3 - 10.2\,i)\,10^{-5}$ as the only free parameter.

In the linear-response regime it is possible to calculate the pump-induced change of the probe field $\zeta(t)$ from $\Delta\zeta(t)$ (Eq. 3.2). However, this assumption is too crude for our experimental conditions, and the full nonlinear response must be calculated for a quantitative agreement between predicted and measured $\zeta(t)$ traces. This calculation is unfortunately beyond the scope of this thesis.

3.4.2 Noise

In an optical experiment, we have to consider two independent sources of noise, electronic noise and optical shot noise, which add quadratically. Optical noise itself has two causes. On the one hand, laser noise σ_{laser} stems from classical fluctuations in the output power of the laser, and usually grows linearly with laser power. The photon noise σ_{ph}, on the other hand, originates from quantum-mechanical uncertainty in the amplitude of the electric field of the laser wave and grows as the square root of laser power. Unless squeezed

light is used, photon noise is the fundamental noise limit. Photon noise is given by [98]

$$\sigma_{ph} = \sqrt{2 \, B \, P \, h\nu} \quad , \tag{3.12}$$

where B is the detection bandwidth and P is the detected optical power.

The electronic noise also has two dominant sources. One is the thermal noise of the amplification stage of the detector (σ_{ampl}, dark noise), which is specified by the noise equivalent power (NEP), and is independent of laser power. Another source of electronic noise, the excess noise, is specific for the analog avalanche photodiodes used here [99]. It arises from statistical fluctuations in the avalanche process following the absorption of every photon. Because it is related to the detection of photons, excess noise has the same statistical properties as photon noise and also increases as the square root of laser power. The excess noise factor F is defined as $\sigma_{shot}^2 = F\sigma_{ph}^2$, where σ_{shot} is the full shot noise. The total noise amplitude σ_{tot} then amounts to

$$\sigma_{tot} = \sqrt{\sigma_{ampl}^2 + \sigma_{shot}^2 + \sigma_{laser}^2} = \sqrt{\sigma_{ampl}^2 + F \, 2 \, B \, Ph\nu + (n_{laser}P)^2} \quad . \tag{3.13}$$

The noise is measured as the standard deviation of a series of calibrated root-mean-square values given by the lock-in amplifier. This is equivalent to the standard deviation of a series of absolute power measurements in the given bandwidth B. Fig. 3.4 shows the measured noise as a function of the probe power at the detector (note that, as long as the pump laser is sufficiently rejected from the detector with dichroic filters, there is no pump-power dependence of the noise level). At low power, the electronic noise dominates and we find a constant contribution of $0.6 \, \text{pW}/\sqrt{\text{Hz}}$, within the specification of the NEP of the detector (section 3.2). At higher power, the optical noise becomes dominant and in this regime, the noise scales as the square-root of the laser power. The power range in Fig. 3.4 was limited by saturation of the detector. Within this range, there is no contribution that scales linearly with laser power, which means that laser noise does not contribute to the total noise. For detected powers levels between 1 and 10 μW, the main noise component is shot noise. The expected photon noise as a function of laser power is indicated with a dashed line in Fig. 3.4. The difference arises from the excess noise generated by the avalanche photodiode and is described by an excess noise factor $F = 3 \approx 1.7^2$, in good agreement with the manufacturer's specification. Replacing the avalanche diode by a PIN diode will remove this excess-noise contribution, if a sufficiently low-noise amplifier is used. The analysis of noise sources in our experiment shows that the interferometer is

not absolutely required to reduce noise from fluctuations of the light sources (laser noise), as our laser and OPO systems are very stable. A much simpler experimental setup in a pump-probe configuration would therefore suffice to provide information on transient absorption only (i.e., on the amplitude signal).

3.5 Conclusion

We have developed a common-path interferometer, which enables time-resolved experiments on single nanoparticles, and with which the absorptive and dispersive responses of the particles can be separated. The design of the interferometer, using birefringent crystals as splitting elements, simplifies the alignment and increases the fringe contrast. A noise analysis showed that the detection is shot-noise limited, just a factor of about 1.7 above the ultimate limit of photon noise. We expect to reach the photon-noise limit by replacing the avalanche diode with a good PIN diode. The interferometer is fully described by an analytical model, which allows us to find optimal working points. While also direct absorption measurements on single particles yield the ultrafast response of the hot electron gas, only an interferometric experiment provides the full complex response of a nanoparticle on the sub-picosecond timescale, free from any model or assumption.

4

Acoustic vibrations of single gold nanoparticles

4.1 Introduction

The confinement of electrons and phonons causes the physical properties of nanometer-sized objects to depart from those of bulk solids [28]. One of the ambitions of nanoscience is to exploit these deviations to tailor the properties of nanoparticles through their sizes and shapes. The plasmon resonance of noble-metal (silver and gold) particles is a collective oscillation of the conduction electrons, which governs their strong interaction with light. The shift and broadening of the plasmon resonance with changes in size and shape remains an active research area [16, 17, 75]. A further strong motivation for optical studies of metal nanoparticles is their recently proposed use as labels for molecular biology [13, 54, 59, 85].

Working with ensembles of nanoparticles entails a fundamental difficulty. The current preparation methods generate a distribution of particles with a significant dispersion of sizes and shapes, and with many possible configurations of defects. This problem can be solved by the isolation of *single* nanoparticles. A number of methods have recently been put forward to study them with near-field [100] and far-field optical microscopy [87]. Each single nanoparticle can be studied in detail, and extended statistics can then be accumulated over many individuals. Following one and the same particle gives access to environmental influences and unravels space and time heterogene-

ity. In this chapter, we show different electronic and elastic components in the time-resolved response of single gold nanoparticles. Combining short laser pulses with the microscopy of single nano-objects (molecules [101], semiconductor [102], or metal particles) offers new insight into their optical and mechanical properties on their characteristic times, picoseconds and shorter.

When an ultrashort pump pulse excites a metal particle, the absorbed energy is first conveyed to the conduction electrons, which collide within some tens of femtoseconds through electron-electron interactions [16, 17, 75]. On a 1-ps timescale, the hot electrons thermalize with the lattice, and, still later (typically 10 ps for a 10-nm particle), the whole particle cools down to ambient temperature via heat diffusion. The sudden heating of the electron gas has mechanical effects. Just as sharp rap causes a bell to ring, an optical excitation launches elastic oscillations, via two mechanisms: First, a short-lived transient arises from the initial surge in electronic temperature and Fermi pressure. This pressure burst is short but strong because of the low heat capacity of the electron gas [44]. Second, as the electronic energy is shared with lattice modes on a picosecond timescale, anharmonicity leads to thermal expansion. For large enough particles, both times are short compared to the period of elastic vibrations (3.3 ps for the breathing of a 10-nm diameter particle).

The optical properties of the hot particle are also modified. The initial excitation spreads the electronic population around the Fermi level, thereby opening new relaxation channels and broadening the surface plasmon resonance [52]. The subsequent thermal expansion of the lattice reduces the electron density, bringing about a red shift of the plasmon resonance. Size variations can thus be optically detected via shifts of the plasmon resonance. In particular, the elastic oscillations that are launched in a particle by a short pulse, are optically detectable through a periodic red shift of the plasmon resonance.

Laser-induced acoustic vibrations of nanoparticles have been previously studied on ensembles [16, 17]. Such bulk observations are only possible as long as the oscillations are synchronized. Small differences in particle size within the ensemble lead to slight differences in oscillation periods. This inhomogeneous broadening, which often dominates the observed decay of the ensemble oscillation, is completely eliminated in our present study of single gold nanoparticles by interferometric pump-probe spectroscopy.

4.2 Experimental method

As a single nanoparticle is much smaller than the diffraction-limited laser spot, and as time-dependent changes in optical properties are small, the signals are weak. Measuring minute absorption changes requires many photons and the reduction of all noise sources, down to photon-noise. An interferometer set close to its dark fringe suppresses intensity fluctuations on all timescales. We designed a common-path interferometer, in which two interfering pulses follow the same optical path at different times and with orthogonal polarizations (Fig. 3.1 on page 48). Defects of the optical components (particularly of the objectives), being nearly identical for both polarizations, cancel to a large extent. The setup is described in detail in chapter 3. A short description follows.

The measuring light pulse is linearly polarized at 45 degrees from vertical and split into probe and reference pulses by a first birefringent crystal (calcite). The reference pulse is polarized along the crystal's horizontal fast axis, and the probe along the vertical slow axis. The pump pulse, being polarized along one of the crystal axes, is not split, and travels at a variable delay from the reference-probe pulse pair. After passage through the microscope, reference and probe pulses are recombined in a second, identical calcite crystal, with its fast axis vertical. Crystals as splitting elements have the advantage that alignment is easy, but the time delay (10 ps) is fixed by their thickness.

A pump-induced change in the real or imaginary part of the particle's dielectric permittivity causes a small variation $\Delta\zeta$ in the probe field's complex amplitude, from E to $(1 + \Delta\zeta)E$. This change is detected by the interferometer, either as an amplitude or as a phase variation. The working point of the interferometer is adjusted by independently rotating a quarter-wave plate and a polarizer. The amplitude-sensitive working point is obtained for slightly different amplitudes but equal phases of the interfering waves, and gives the variations of the real part $\text{Re}(\Delta\zeta)$ of the probe field. At the phase-sensitive working point, the amplitudes are equal and the phases are slightly different, giving $\text{Im}(\Delta\zeta)$. In the following, unless mentioned, we use the amplitude-sensitive working point.

The Fourier-limited 1-ps probe pulses are generated at a 76 MHz rate by an intra-cavity frequency-doubled optical parametric oscillator (OPO), tunable between 520 and 650 nm. The OPO itself is pumped at 800 nm by the 1-ps pulses of a Ti:sapphire laser. A small fraction of the latter beam, used as pump, is modulated at 400 kHz by an acousto-optical modulator (AOM). The probe (and reference) power varied between 12 and 330 μW, the pump power between 0.5 and 5 mW. The home-built microscope includes an oil-
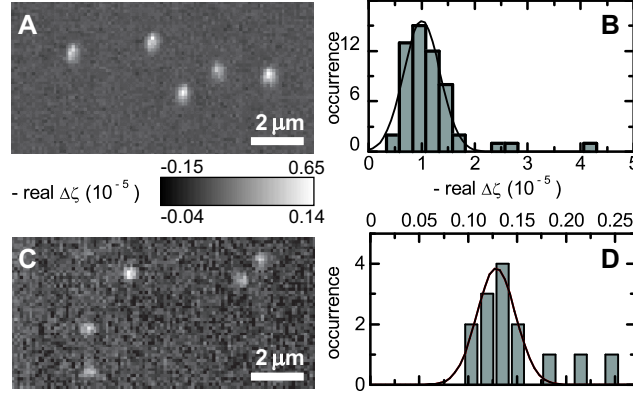
Figure 4.1: Raster-scanned images of single gold nanoparticles and corresponding histograms of field changes $\text{Re}(\Delta\zeta)$ for 20 nm (A,B) and 10 nm diameter (C,D). The integration times were 100 and 200 ms/pixel, respectively. A minimum signal level was required to start the fit to a Gaussian spot, indicated by a dashed line in the histograms. The relative width of the distributions, as deduced from rough Gaussian fits, is 34 % (20 nm) and 11 % (10 nm). The noise level in panel (C) is $7.1 \cdot 10^{-5}$, less than three times the shot-noise limit.

immersion objective (numerical aperture NA=1.4), and an air-spaced objective (NA=0.95). The measurement spot has a 300 nm diameter. The sample cover slide, mounted on a piezo stage, can be scanned with 25 nm precision. The interferometer output is fed to an analog avalanche photodiode and demodulated in a lock-in amplifier.

The samples are roughly spherical gold particles with diameters ranging between 10 nm and 80 nm (British Biocell International and Sigma-Aldrich), spin-coated with a poly(vinyl alcohol) solution (10 g/l) on a clean glass cover slide (see section 3.2 for a description of the glass-cleaning procedure) . The polymer film was about 20 nm thick.

Please note that on the axes of the figures in this and the next chapter we have plotted - $\text{Re}(\Delta\zeta)$, contrary to our publications. This is caused by a late discovery of a mistake of 180° in the phase setting of our lock-in amplifier. This mistake had been made consistently in all plots. We have decided to make a correction to the axes and not to the traces. The convention of plotting - $\text{Re}(\Delta\zeta)$ has been kept for the unpublished data as well.

4.3   Imaging single gold nanoparticles

Figure 4.1 shows images of single gold nanoparticles with 10 and 20 nm diameter. The sample preparation procedure was that of chapter 2, where third-harmonic signals proved that the particles were isolated. Figure 4.1 is recorded for zero delay, i.e., when the pump and probe pulses impinge simultaneously on the sample, providing maximum contrast. We extracted histograms from a set of images, as done in Chapter 2. The discrimination threshold between noise and particles was $\mathrm{Re}(\Delta\zeta) = -2.7 \cdot 10^{-4}$ (B) and $-1.3 \cdot 10^{-4}$ (D). The resulting distributions, shown in Fig. 4.1B and D, being mono-modal and well separated from the background, confirm that each spot corresponds to a single particle. The relative width of the 20-nm distribution, 34%, is considerably larger than expected from the volume spread given by the manufacturer (19%). Additional fluctuations in shape, orientation and surroundings of the particles can contribute to this large dispersion via shifts and intensity changes of the plasmon resonance, as recently observed by Berciaud et al. [60]. In order to minimize the spread in signal, we recorded the data of Fig. 4.1 with an off-resonant probe (635 nm). Pump and probe power were limited by the maximum permissible absorption in the particle, which results in a detection limit of 10-nm diameter for gold nanoparticles, for reasonable sampling times shorter than one second per pixel.

4.4   Time-resolved experiments

We measure the time-dependent response of the nanoparticle to excitation with the pump pulse by varying the delay between the pump pulse and the probe-reference pair of pulses. Fig. 4.2 shows an example of the response of a single 60-nm gold nanoparticle in the laser focus, detected with a bandwidth of 7.8 Hz. The first part of the trace, which is enlarged in the inset, shows two sharp peaks, that occur when the pump is overlapped with the probe and with the reference respectively. These peaks stem from the change in optical response due to the hot electron gas. From the rise and decay times of the peaks, the electron-electron scattering and electron-phonon coupling times can be obtained [17, 103]. Since these processes take place on timescales faster than a picosecond, the width of the peaks is dominated by the pulse length if the measurement is carried out with picosecond pulses, and information on the electronic decay times of the particle is lost. However, by using shorter pulses, it is possible to resolve these processes. This is demonstrated in the
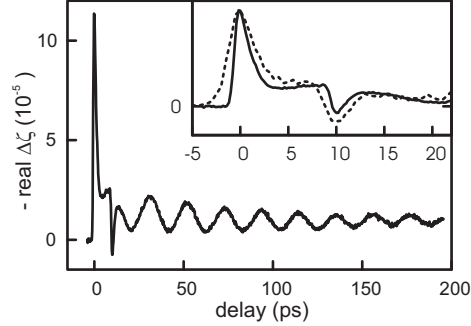
Figure 4.2: Example of a delay scan of a single 60-nm gold nanoparticle showing a short spike due to the hot electron gas and periodic oscillations of the particle size. The inset compares the 'femtosecond' (solid) and the 'picosecond' (dashed) configuration of the laser system in their resolving power of the fast electronic process. The traces in the inset are normalized to the first peak. The detection bandwidth was 7.8 Hz.

inset of Fig. 4.2, where the fast electronic response is measured with femtosecond and picosecond pulses on two different single particles. In the femtosecond experiment, the peaks are narrow enough to resolve the electronic processes in the particle. On a longer timescale, the signal shows a damped harmonic oscillation. This is a direct observation of the acoustic vibrations of the particle, from which we can derive information on the elastic properties of the particle itself and its mechanical coupling to the surroundings.

As mentioned in section 4.1, the optical detection of acoustic vibrations is assumed to be caused by a periodic red shift of the plasmon resonance, caused by a periodic change of the electron density. Figure 4.3 shows two delay scans, one with the probe tuned to the red wing (595 nm) and one to the blue wing (520 nm) of the particle's resonance. The oscillations are out of phase, which gives clear evidence for this periodic red shift, as has also been seen earlier in bulk experiments on silver nanoparticles [104].

In Fig. 4.4, we combine the amplitude and phase separation with time-resolved experiments, in order to measure the complete complex temporal response of the particle. As mentioned in section 3.3, for delay times larger than 10 ps, it is important to choose a working point close to the dark fringe, to ensure the full separation of amplitude and phase. The interferometer was tuned to a 2% fringe, to comply with the approximation of Eq. (3.2). In Fig. 4.4A, the real and imaginary temporal responses of a single particle are shown together. Here, the different spectral origin (resonance broadening
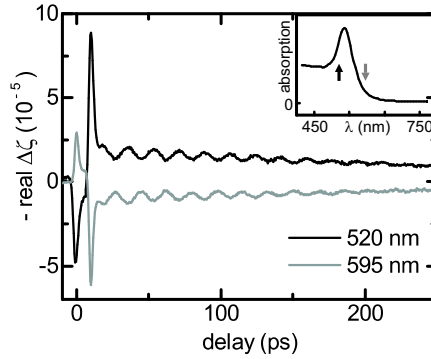
Figure 4.3: Two delay scans of one single gold particle, with the probe on the red side (black trace) and on the blue side (grey trace) of the surface plasmon resonance (see inset). The period of the oscillations is 17.6 ps for both traces, corresponding to a particle size of 53 nm [17].

versus red shift) of the peaks and of the oscillations becomes apparent, since the two peaks have the same sign in both the amplitude and the phase configuration, while the vibrations are exactly out of phase. Figure 4.4B shows the real and imaginary temporal response of another particle in the same sample. While the amplitude response of this particle is nearly the same as that of the particle in Fig 4.4A, the phase response is rather different. The electronic contribution gives a mainly dispersive response, while the acoustic vibrations are completely absorptive. The differences between the two particles can be visualized in a different manner in Fig. 4.4C, where the dispersive response is plotted against the absorptive response for both particles. The trace of the particle from Fig. 4.4A (gray) shows a weaker electronic response, while the overall trace is tilted towards the real axis. These kind of differences between particles can arise from differences in their spectral responses, themselves due to differences in their size, shape or local environment. Further study is needed to precisely correlate the optical and structural properties of the particles, but there is little doubt that single-particle studies of gold nanoparticles will lead to a better understanding of their properties, and to such applications as elasticity and damping sensors at nanometer scales.

Because of their size and shape distribution, individual particles present slightly different oscillation periods, and they run out-of-phase on longer timescales. This inhomogeneous broadening of the breathing mode totally masks any intrinsic damping of the ensemble oscillation. Selecting a single particle provides direct access to the intrinsic (or homogeneous) damping, by
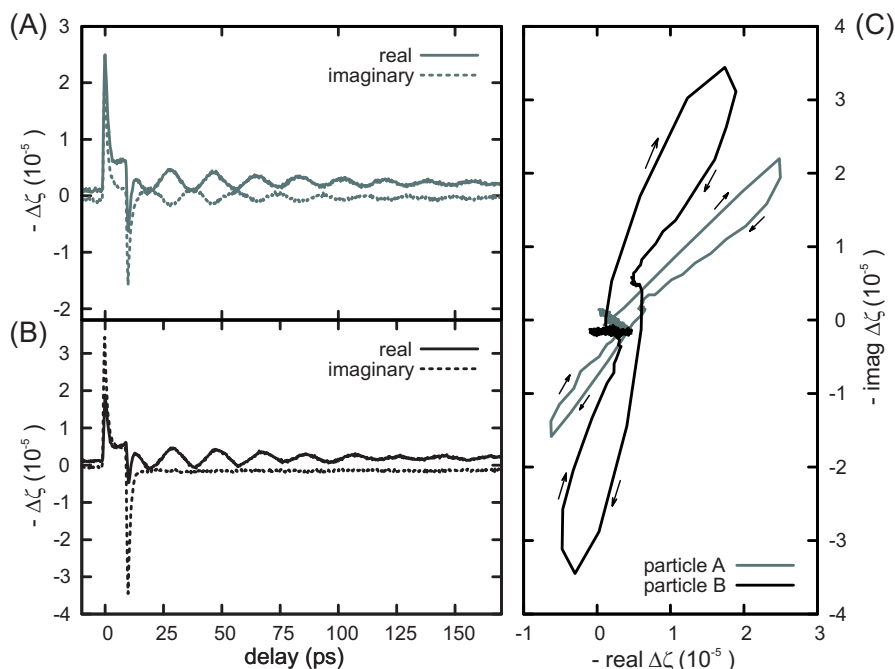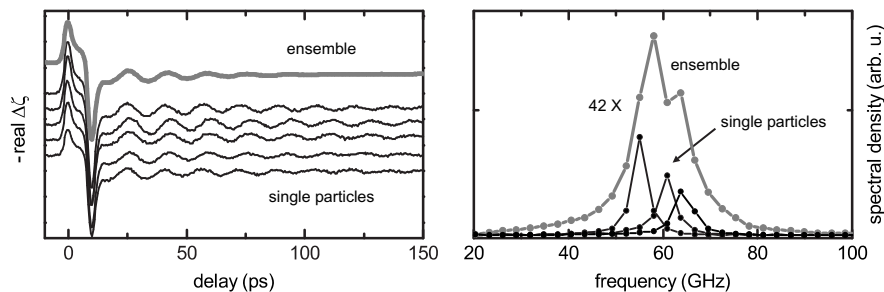
Figure 4.4: (A,B) Delay scans of two gold nanoparticles with a nominal diameter of 60 nm, measured at the amplitude (solid) and phase (dotted) sensitive working point. For particle (A), the peaks have the same sign, but the sign of the vibrations is opposite demonstrating the different spectral origin. For the particle in panel (B), the dispersive contribution to the peaks is much stronger, while the vibrations completely vanish in this phase-sensitive configuration. (C) Plotting $\mathrm{Im}(\Delta\zeta)$ against $\mathrm{Re}(\Delta\zeta)$ reveals the full response of both particles in the complex plane. The arrows indicate the time evolution. In all plots, the detected intensity was 2% of the bright-fringe intensity. The traces show the average of five measurements, each with a detection bandwidth of 7.8 Hz.

removing ensemble averaging. The damping rate is found to vary from particle to particle, probably through fluctuations of the environment and of the coupling to acoustic phonons in the substrate. The resonance quality factors $Q = \nu/\Delta\nu$ ($\Delta\nu$ being the mode's FWHM in the power spectrum), are about 4-5 for an ensemble, but reach considerably larger values, distributed between 15 and 30 (corresponding to amplitude $1/e$ relaxation times of 75-150 ps), for individual particles in the thin polymer film.

A striking illustration of the strength of single-particle observations is displayed in Fig. 4.5. The left panel shows delay scans and the right panel shows

Figure 4.5: Comparison of delay scans (left panel) and power spectra of the oscillatory part (right panel) of a set of 29 single gold nanoparticles (examples shown as thin black lines) to a reconstructed ensemble measurement (thick grey line; for this experiment, the sample was covered by index-matching fluid, which increased the damping of the oscillations). The particles have a nominal size of 50 nm with a spread of 6 %. The sample was prepared as described in this chapter and additionally coated with an index-matching fluid. The average spectrum in part (B) is scaled by 42 for clarity. The quality factor $Q = \nu / \Delta\nu$ is 4 for the ensemble and about 13 for the individual traces. The index-matching fluid reduces the quality factor of the individual traces compared to particles embedded in a thin polymer film only (see main text).

power spectra of the oscillatory behavior of nanoparticles. We measured 29 single particles under the same experimental conditions and then calculated an average trace to yield an "ensemble" signal (thick grey line). Examples of the single particle data are shown as thin black lines. Comparing the "ensemble" signal to the single particle signal, we clearly see that the ensemble oscillation damps much faster than those of individual nanoparticles, and as a result, the peak in the ensemble power spectrum is much broader, as can be seen in the right panel of Fig. 4.5. Because of the size distribution, the nanoparticles present slightly different oscillation periods, and they run out-of-phase on longer timescales. This inhomogeneous broadening easily masks the intrinsic decay of the vibrations of individual particles.

4.5 Vibrational modes

The elastic vibration modes of a solid sphere are labelled in Lamb's theory [46] by two integers, n, the harmonic order, i.e., the number of radial nodes, and l, the angular momentum number, which represents the angular dependence of the mode. We calculated the mode frequencies using bulk gold transversal and longitudinal sound velocities [50] following the equations
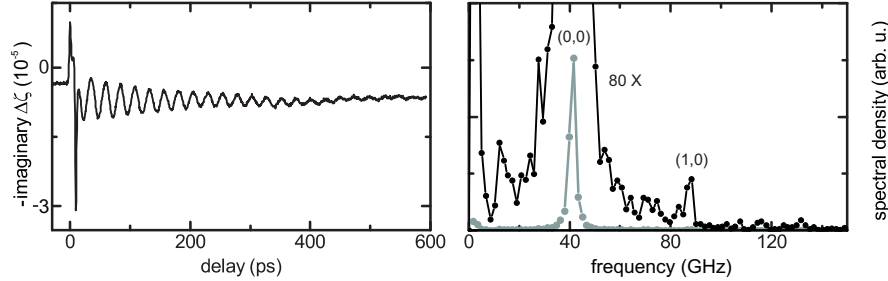
Figure 4.6: Delay scan of a single 80-nm particle, which shows the second harmonic $(n, l) = (1, 0)$ of the fundamental breathing mode at $\Omega_{1,0} \approx 2.17 \cdot \Omega_{0,0}$, close to the expected value of Lamb's theory at $2.103 \cdot \Omega_{0,0}$. The delay trace (left panel) has no signs of higher harmonics, but the power spectrum (right panel) shows a clear peak at $\Omega_{1,0}$.

given in Ref. [46] for free boundary conditions. Most of the particles only show the radial breathing mode $(n, l) = (0, 0)$ at a frequency $\Omega_{0,0}$, sometimes with a weak trace of the higher harmonic $(n, l) = (1, 0)$ at about $2.1 \cdot \Omega_{0,0}$, as seen in ensemble measurements for silver nanoparticles [105]. An example of a detected second harmonic is shown in Fig. 4.6. Other particles show an additional mode at a lower frequency. Fig. 4.7A shows an example, where the time-response clearly deviates from a sine-curve. The power spectrum obtained by Fourier transformation of the oscillation (Fig. 4.7B, top trace) shows two distinct peaks. The high-frequency peak (at 67 GHz for the upper spectrum) corresponds to the spherical breathing mode $(n, l) = (0, 0)$ of a 45 nm diameter gold sphere [17]. Another peak appears at lower frequency (28 GHz for the upper spectrum). This new peak cannot arise from the breathing mode of a second, larger particle at the same spot, for the optical signal (which scales as the third power of particle diameter) would then be too weak . We assign the peak at 28 GHz to the non-spherically symmetric $(n, l) = (0, 2)$ mode, involving shear strain (uniaxial cigar-to-pancake deformations of the sphere, or ellipsoidal deformation), which was seen already in Raman spectra of semiconductor nanoparticles [46]. We rule out the lower-order $(n, l) = (0, 1)$ mode, corresponding to a pear-shaped deformation, because it does not couple to the optical response, at least at the lowest order and in a spherically symmetric environment. Both modes can only be excited by the isotropic heat pulse if the spherical symmetry of the particle's expansion is broken either by the substrate, or by the particle's shape. Indeed, the $(n, l) = (0, 2)$ mode does not appear in ensemble pump-probe experiments, where the particles' environment is isotropic. The measured frequency of

70
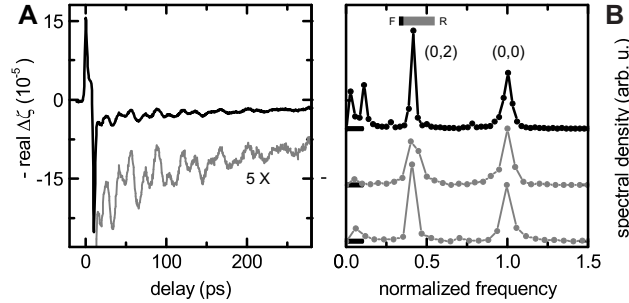
Figure 4.7: (A) Delay scan of a single gold nanoparticle. The oscillation pattern shows a complex modulation. The tail of the trace is also shown 5× enlarged. (B) Power spectra of this particle's oscillation (top spectrum) and of two other particles. Frequencies and amplitudes are normalized to those of the $(0,0)$ mode (The absolute frequencies were 67 GHz, 59 GHz, 63 GHz, from top to bottom). The low frequency peak (top spectrum: 28 GHz) lies between calculated frequencies of the $(0,2)$ mode for free boundary (F, thick line on bar) and for rigid boundary (R, end of bar). The ratio of its frequency to that of the breathing mode is constant.

the $(n,l) = (0,2)$ mode lies between the frequencies expected for a sphere with free and rigid boundaries (see bar in Fig. 4.7B). The shift from the free sphere's vibration could possibly arise from elastic perturbation by the glass half-space. We note, moreover, that the ratio of $(0,2)$ to $(0,0)$ frequencies was the same for all measured particles, which rules out deviations from the spherical shape as origin of the low-frequency mode, as these would vary from particle to particle.

4.6 Conclusion

Interferometric pump-probe measurements of single metal particles have the double advantage of high sensitivity and of providing the full optical response, including phase and amplitude. We have imaged gold particles as small as 10-nm diameter, these being the detection limit of our setup, due to saturation of the absorption. The use of 100-fs pulses allows us to study electronic properties on a single-particle basis. On a longer timescale, we recorded time-traces of acoustical breathing modes, displaying particle-to-particle fluctuations in frequency and decay rate, and revealing the intrinsic damping of mechanical vibrations. We found a new mode at lower frequency, so far unobserved in pump-probe experiments, and presumably coupled by a substrate-induced breaking of the spherical symmetry. Mechanical vibra-

tion modes are fascinating doorways to the elastic properties of metal particles and of their environment. More generally, probing single nano-objects and nano-structures with short laser pulses opens a wealth of real-time studies of nano-mechanics on picoseconds, the characteristic vibration times at nanometer length scales.

5

Correlation of optical and structural properties

5.1 Introduction

The optical responses of gold nanoparticles as studied in this thesis carry signatures of their structural properties, such as their size and shape, and also of their environment. For example, the period of the acoustic vibration depends strongly on the size of the particle and is hardly affected by anything else, while the damping time on the other hand is strongly influenced by the elastic coupling of the particle to its close environment (see chapter 1 and [50]). Like snowflakes, no two gold nanoparticles are exactly alike. Electron microscopy images show a rich variety in sizes and shapes within a sample of particles of nominally the same size. The ultimate goal of this chapter is to try to make a correlation between the optical effects that we detect and the structure of the individual particles. Obviously this is a rather ambitious objective, since the structural properties manifest themselves only indirectly. The spatial resolution of optical experiments is limited to the wavelength of the light source, which in our case exceeds the dimensions of the particles by far. Electron microscopy, exploiting the much shorter wavelength of electrons, can achieve a much higher resolution, up to the atomic scale, and is therefore capable of accurately mapping the structure of the particle. Ideally, we should therefore combine our optical experiments with electron microscopy on the exact same particle. Although these experiments, that are far from trivial, are

currently pursued in our lab, here we will still have to do without.

Besides electron microscopy, there are a number of other methods that can be used to acquire more information about the structure of a nanoparticle. One of those methods is white-light spectroscopy, a method with which the absorption spectrum of a particle can be measured. Polarization dependent measurements of the absorption spectrum can give information on the ellipticity and orientation of the particle [106]. Additionally we can obtain structural information from time-resolved experiments. A measurement of the period of the acoustic vibration can for example yield the size of the particle, although assumptions about the shape and environment of the particle have to be included in the calculation [50, 48]. Another method to correlate optical and structural properties is statistical analysis of many single particles. By comparing electronic and vibrational properties of many individual particles, not only can we gain insight into the average properties of the ensemble, but we can also investigate the differences between particles by plotting histograms of several parameters. By doing experiments on single particles, it is for the first time possible to directly measure the homogeneous damping of the particles, which is solely governed by the elastic interaction of the particle and its local environment.

In the first part of this chapter, we explain the white-light spectroscopy experiments and show that it is possible to make a first-order determination of the shape of our particles. We then proceed to combine white-light spectroscopy and pump-probe interferometry on the same particle, in order to unravel the processes behind the signals that are detected in the pump-probe experiments. The second part contains a statistical analysis of the electronic and vibrational properties of a large collection of single particles. We will also make a first step towards investigating the effect of the environment on the period and damping time of the acoustic vibrations by studying gold nanoparticles that are coated with a layer of silica. Finally, in section 5.4, we present some more detailed experiments on particles that show a second vibrational mode, associated with ellipsoidal deformation, that were already touched upon in section 4.5.

5.2 Combination of white-light spectroscopy and pump-probe interferometry

We show the combination of white-light spectroscopy, with which the absorption spectra of single gold nanoparticles can be measured, and the pump-probe technique that has been presented in chapters 3 and 4. In this exper-

iment, light is reflected from a surface on which gold nanoparticles are deposited. The reflected light is collected on a spectrometer, and contains contributions from light that is scattered by the particle and light that is reflected from the interface. From the interference of these two contributions, the scattering and absorption spectra can be extracted.

5.2.1   Experimental method

White light from a high-power gas discharge lamp is focussed with an air-spaced objective (Olympus, 60×, NA = 0.9, cover-slide corrected) on an interface between microscopy immersion oil and a cover slide on which gold nanoparticles are spincoated. The samples were prepared using the method described in section 3.2. The reflected light that is collected, is a superposition of the waves that are reflected from the interface and of the waves that are scattered by the particles. We can detect the reflected light with a photon-counting APD (PerkinElmer) or with a spectrometer (SpectroPro 500i, Acton Research) and a liquid-nitrogen-cooled CCD-camera (Spec-10, Princeton Instruments). A bandpass filter, transmitting light between 450 and 700 nm was placed before the APD. In order to select a proper beam profile, a pinhole of 15 μm diameter was placed in the focus of the beam expander in the excitation path. A sketch of the white-light scattering setup is shown in Fig. 5.1A, while a typical source spectrum of the Xenon lamp is plotted in Fig. 5.1B. The pump-probe experiment is explained in detail in chapter 3.

If an incident field E_i is focused onto an interface, the reflected field is $E_r = rE_ie^{-i\pi/2}$ (with r the reflection coefficient of the interface, and a phase of $\pi/2$ has been introduced to account for the Gouy phase shift [66]). Following [66] further, the field scattered from the particle is $E_s = s(\lambda)E_i$, where $s = |s(\lambda)|e^{\phi(\lambda)}$ is given by

$$s = \eta\alpha(\lambda), \tag{5.1}$$

where η is a factor describing the geometry of the experiment with the particle in the focal spot, with dimension $1/V$. $\alpha(\lambda)$ is the polarizability of the particle (Eq. (1.15)). The intensity I_{det} measured at the detector is a superposition of the light that is reflected from the interface and the light that is scattered by the particle.

$$I_{det} = |E_r + E_s|^2 = |E_i|^2 \left(r^2 + |s|^2 - 2r|s|\sin(\phi)\right) \tag{5.2}$$

To measure the spectrum of the particle $\sigma(\lambda)$, we have normalized the spectrum recorded with a particle in the focus $I_{det}(\lambda)$ to a signal recorded next to
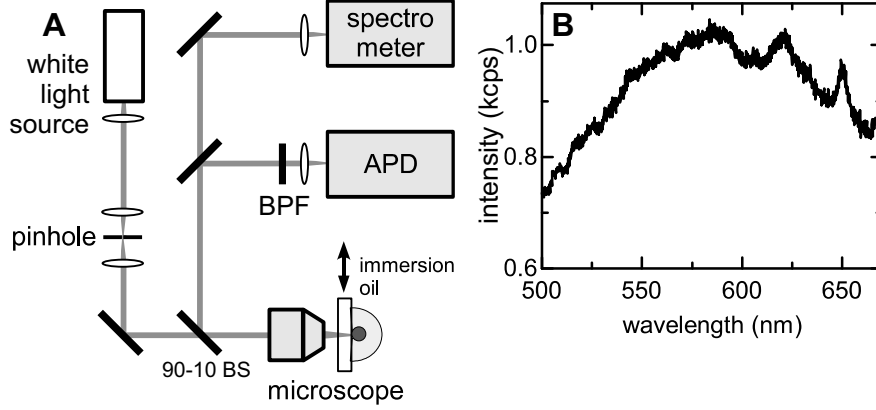
Figure 5.1: (A) Schematic drawing of the setup used for white-light spectroscopy of single gold nanoparticles. Light from a Xenon lamp is reflected from an interface on which gold nanoparticles are dispersed. From the interference of the reflected light and the light scattered by the particle, collected by a spectrometer, the absorption spectra can be deduced. With the APD, confocal scans of the sample can be made. The 90-10 BS is a beam splitter that reflects 90% of the light and transmits 10%. The BPF is a band-pass filter that transmits light between 450 and 700 nm. (B) Typical spectrum of the white-light source.

the particle $I_r(\lambda)$ (typically 3 μm away):

$$\sigma(\lambda) = \frac{I_{det}(\lambda) - I_r(\lambda)}{I_r(\lambda)} = \frac{\eta^2}{r^2}|\alpha(\lambda)|^2 - 2\frac{\eta}{r}|\alpha(\lambda)|\sin(\phi)$$

$$= \frac{\eta^2}{r^2}|\alpha(\lambda)|^2 - 2\frac{\eta}{r}\mathrm{Im}\left[\alpha(\lambda)\right] \tag{5.3}$$

We see that part of the signal has contributions proportional to $|\alpha(\lambda)|^2$ and to $\mathrm{Im}\left[\alpha(\lambda)\right]$, similar to scattering (Eq. 1.17) and absorption spectra (Eq. 1.16), respectively. Note that the spatial dependence of the scattered and reflected fields are not equal. The reflected wave is a Gaussian wave, while the scattered wave is spherical. However, we neglect this inequality here, assuming that the NA of the reflected field is very large, so that it approximately overlaps with the scattered field.

5.2.2 White-light scattering

Figure 5.2A shows a confocal scan of 20 × 20 μm, of a sample containing gold nanoparticles with a nominal diameter of 60 nm, illuminated with unpolarized white light from a Xenon lamp. The light is detected by the APD through
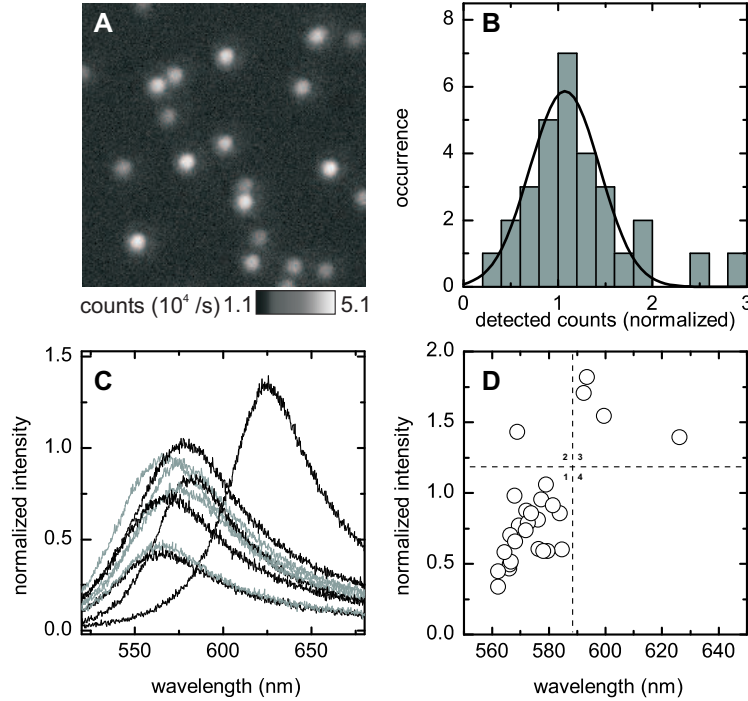
Figure 5.2: Scattering spectra with unpolarized white light from a high power Xenon gas discharge lamp, of gold nanoparticles with a nominal diameter of 60 nm, on a BK7 substrate in immersion oil. (A) 20x20 μm image of light collected on the APD while scanning the sample through the focus of the microscope. (B) Histogram of normalized scattered intensities as collected with the APD. The intensities were normailzed as $I_{norm} = (I_{peak} - I_{bg})/I_{bg}$. The solid line is a Gaussian fit of the histogram, yielding a width of 37%. (C) Spectra recorded for the spots in (A) in the focus of the microscope, normalized to a background spectrum next to the particle. (D) Maximal normalized intensity of 28 spectra, including those shown in (C), plotted against the wavelength of the maximum. The four quadrants are used to classify the particles as single or double particles, see text for details.

a bandpass filter that transmits light between 450 nm and 700 nm. The particles are clearly detected, and a histogram of detected intensities, normalized to the background here, of 28 particles (see Fig. 5.2B) shows a monomodal distribution, of which the relative width is about twice the volume distribution as it is specified by the manufacturer, indicating that we detect single particles here. The spots in this image have a width of about 1 μm (FWHM) and a signal-to-noise ratio of roughly 30.

Figure 5.2C shows spectra of the particles in Fig. 5.2A, again measured

with unpolarized light and normalized to a background spectrum, measured roughly 3 μm away from each particle. Most of the spectra have a peak between 560 and 580 nm, however, one of the spectra is largely red shifted compared to the others. The distribution of maximum detected intensities is comparable to the distribution shown in Fig. 5.2A, with the red shifted particle also here as an outlier. The peak wavelength is plotted against the maximum intensity in Fig. 5.2D, for the spectra shown in Fig. 5.2C and 18 other spectra. To make a distinction between the different types of spectra, we have divided this plot in four quadrants. Most spectra fall in the first quadrant, with peak wavelengths below 590 nm and a maximum normalized intensity below 1.2. The intensity distribution in these spectra resembles the Gaussian distribution in the histogram of Fig. 5.2B, and these spectra stem from single particles. The outliers of the distribution either lie in quadrant 2, having a high maximum intensity, but a peak wavelength below 590 nm, or in quadrant 3, having a high maximum intensity and a highly red-shifted peak wavelength. These latter spectra most likely stem from close pairs of particles. The spectrum in quadrant 2 is simply the sum of two single-particle spectra, located far away from each other so that there is no interaction. The red shift of the spectra in quadrant 3 can be explained by a near-field interaction of the electrons of two particles located close together. The longitudinal plasmon that is thus created gives rise to a largely red-shifted spectrum. No particles are located in the fourth quadrant. A particle that would fall in this square could for example be a rod-shaped particle with roughly the same volume as a sphere with a 60-nm diameter. Although electron microscopy shows that such shapes can occur in our samples, no such particles have been detected here.

The elongation and orientation of the particles in the plane of the sample can be determined from spectra measured with polarized white light [106]. If a particle is elongated, a second, red-shifted, peak appears in the spectrum, which is associated with a plasmon polarized along the long axis of the elongated particle. The intensity of the longitudinal peak strongly depends on polarization. If the elongation is small, the two modes fall close together and cannot be distinguished. The spectrum of a slightly elongated particle therefore appears as a single peak, which red-shifts as the polarization of the source is rotated. A major drawback of this method is that it is completely blind for elongations perpendicular to the sample plane. A previous study that used polarization dependent absorption spectra to determine the shape and orientation of nanoparticles used the dipole approximation to model the spectra [106]. Our particles are too large for this approximation and we have
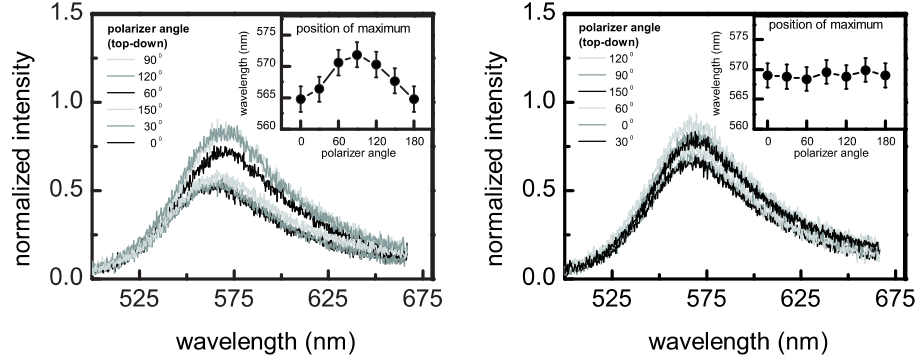
Figure 5.3: Scattering spectra using linearly polarized white light, as functions of polarization angle, of 30-nm radius particles in immersion oil, on a sample of BK7 glass. In (A) the spectra shift as the polarization angle is rotated, which means that the particle is elongated. In (B), the spectra are independent of polarization angle, indicating that the particle is possibly spherical.

to use Mie theory, which only applies to spherical particles. To determine the absorption spectra of large non-spherical particles, numerical methods such as the T-matrix method [107, 108] have to be used. Since at this point, we are only qualitatively interested in the question whether the particles are spherical or not, and not quantitatively in their ellipticity, we have not attempted to model the polarization dependence of these spectra. To obtain an idea of the order of magnitude of the detected elongations, in the dipole approximation, a red shift of 5 nm for perpendicular polarizations, as observed in Fig. 5.3A, gives an aspect ratio (short axis of the particle divided by the long axis of the particle) of 0.9 [106].

Figure 5.3 shows spectra of two single gold nanoparticles, as functions of the polarization direction of the light source. In Fig. 5.3A, the spectrum red shifts as the polarization changes, with a 90° difference between the minimum and maximum red shift. This particle is clearly elongated. For the particle in Fig. 5.3B, there is no red shift observed at all as the polarization is rotated. For this particle we can conclude that, at least in the sample plane, it is spatially isotropic. Although there is no red shift detected for this particle, there is a significant change in the normalized intensity of the spectrum as the polarization is rotated. The maximum intensity is detected at 120 degrees, and in fact, all polarization-dependent spectra have a bias towards this value, even spectra of particles that have the maximum red shift away from 120°. We therefore do not believe that this effect is caused by the particle, but rather that it is an artefact of the measurement, most probably an im-

perfection in the normalization, possibly caused by a mismatch between the Gaussian wave of the source and the spherical scattered wave. Note that the 120 degrees is measured in the frame of the polarizer, and corresponds to an angle of 45 degrees from vertical in the laboratory frame.

5.2.3   White-light and pump-probe spectra of the same particle

By combining white-light spectroscopy with pump-probe interferometry, we can now correlate the ultrafast properties of the particle measured in the pump-probe experiment directly with the absorption spectrum that we know from the white-light experiment. In this way, we hope to exclude shape effects from the measurements by selecting spherical particles, and more-over we can gain a better insight into the mechanisms behind our detection scheme. In order to do so, we first have to extract the absorption spectrum from the spectra that we measure.

From the similarity of Eq. (5.3) to contributions from scattering and absorption, we have chosen to fit our spectra with a linear combination of absorption and scattering spectra Eqs. (1.4) and (1.5).

$$\sigma(\lambda, R) = A(R, \eta) \left[\sigma_{sca}(\lambda, R) - B(R)\sigma_{abs}(\lambda, R) \right] + C \qquad (5.4)$$

With a known dielectric function of the particle [27], and assuming that the particles are spherical, the Mie spectra only depend on the radius of the particle and the refractive index of the environment. These two parameters cannot be determined independently, thus we have to fix one. In the configuration that we have chosen here, with the particles embedded in immersion oil, the refractive index is well defined, and therefore fixed at 1.52. We now find a radius of the particle from our fit and using this, we can reconstruct the absorption spectrum of the particle. Note that the fit function above assumes that the particles are completely spherical, and that the radius that is returned is only valid for the chosen refractive index of the medium, while we cannot exclude local variations of the index of refraction. We therefore only use this fit to determine the absorption spectrum, and not to find structural parameters such as the radius of the particle.

For four different particles, we have determined the absorption spectra in this way, and we have combined this with pump-probe measurements with six different probe wavelengths between 523 and 609 nm. Figure 5.4 shows these delay traces for one particle. We see that the electronic amplitude, defined as the magnitude of the first peak in the delay scans, changes sign between 550 nm and 570 nm, and that the phase of the vibrations makes a 180°

phase shift between 530 nm and 550 nm. Also at 550 nm, the electronic amplitude is strongest, while the vibrations are weakest. We have determined the intensity of the electronic amplitude and the amplitude of the oscillations for this and three other particles and compared these signals to absorption spectra measured with an unpolarized light source. This is shown for each particle separately in Fig. 5.5. The differential spectra, as measured in the pump-probe experiments, are completely different for the electronic signal and the acoustic vibration, due to their distinct spectral origin (see section 1.3.3). If we compare the differential spectra to the absorption spectra, we see that each particle shows a similar trend. The electronic signal peaks at the resonance, where the vibrations vanish. The maximum amplitude of the vibrations lies roughly halfway between the resonance and the half-width at half maximum in the red wing of the spectrum. In the blue wing, the vibrations are always much weaker than in the red wing. The polarization-dependence of the resonance wavelength is plotted for al four particles in Fig. 5.6.

To enable a more quantitative comparison between the differential and the absorption spectra, we have scaled all spectra according to
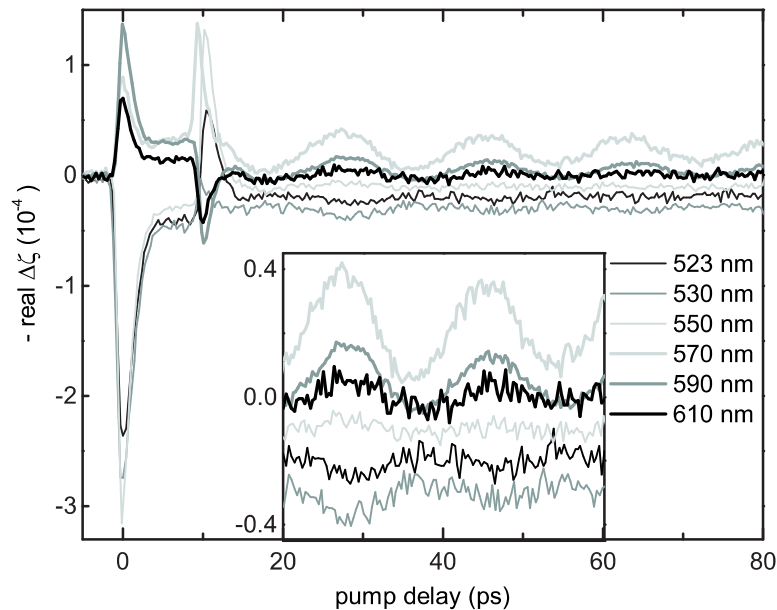
Figure 5.4: Delay traces of a single gold nanoparticle for six different probe wavelengths. The inset shows an enlarged crop of the oscillatory part of the traces. The pump power was kept constant at 125 μW in the sample plane.
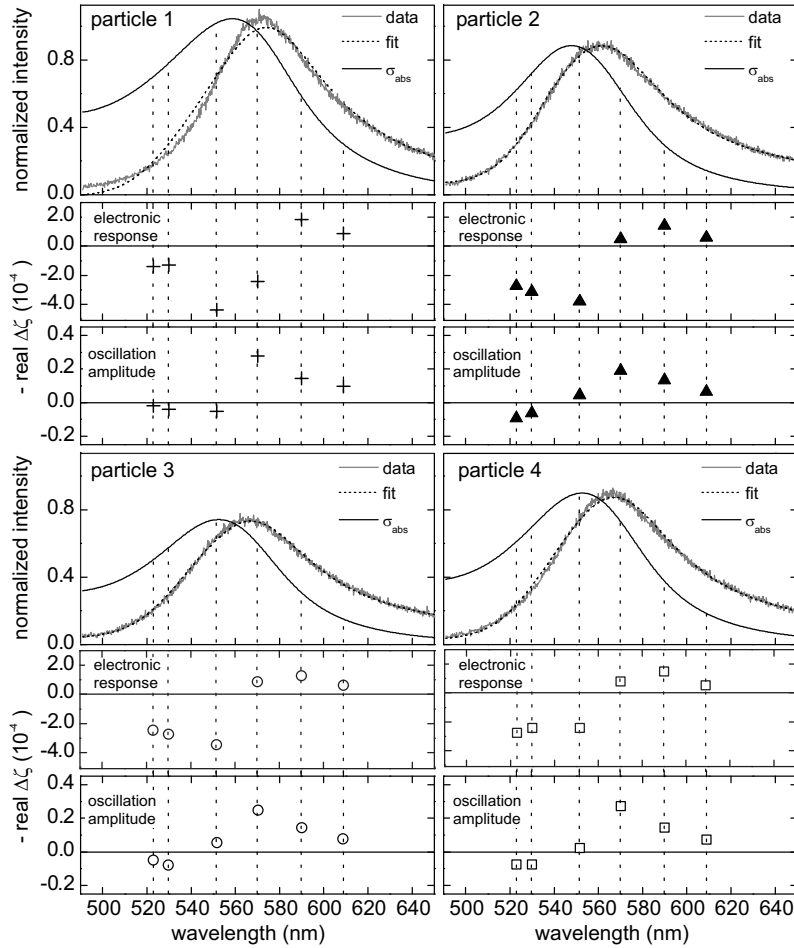
Figure 5.5: Comparison of absorption and pump-probe spectra of four different single gold nanoparticles. For each particle, the top panel shows white-light spectra as measured using an unpolarized source. The dotted lines are fits of the spectra to Eq. 5.4. The solid lines are plots of the corresponding absorption spectra. In the middle panel, the electronic response, defined as the highest point of the first peak in the delay traces, has been plotted for the corresponding probe wavelength. In the bottom panel, the oscillation amplitude has been plotted against the probe wavelength.

$$\lambda_s = \frac{\lambda - \lambda_0}{w} \qquad (5.5)$$

where λ_0 is the resonance wavelength and w is the half width at half maximum in the red wing of the resonance. By applying this scaling, and normalizing all spectra, the absorption spectra almost fully overlap. The result of this transformation can be seen in Fig. 5.7, in the top panel for the absorption spectra and in the lower two panels for the electronic response and the acoustic vibrations. It appears that all points fall on the same curve. We have tried to model these results, using a model based on separation of the dielectric functions of the bound and free electrons, using a Drude model [26]. Heating of electrons and lattice were then calculated through their effect on the free electrons only. Although the rough behavior fits the experimental observations, the model was too simple to make accurate predictions. The effect of the bound electrons has to be included for a correct prediction of the differential spectra. The qualitative behavior however agrees with the optical contrast mechanisms explained in section 1.3.3.

To summarize these results, we have been able to measure white-light scattering spectra of single gold nanoparticles, and have correlated these spectra with pump-probe interferometry on the same particle. The results we find can be qualitatively explained by broadening as the contrast mechanism of the electronic peak, and with a periodic red shift of the surface plasmon resonance as the contrast mechanism of the acoustic vibrations. A quantitative theoretical explanation could unfortunately not be given. A model that only included excitation of the free electrons proved to be too simple to fully explain the experimental results.
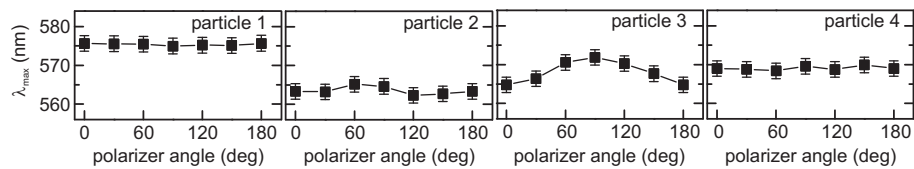
Figure 5.6: Wavelength of the resonance in the detected white-light spectra as a function of polarization angle of a polarized white-light source. These plots are a measure for the ellipticity of the particles.
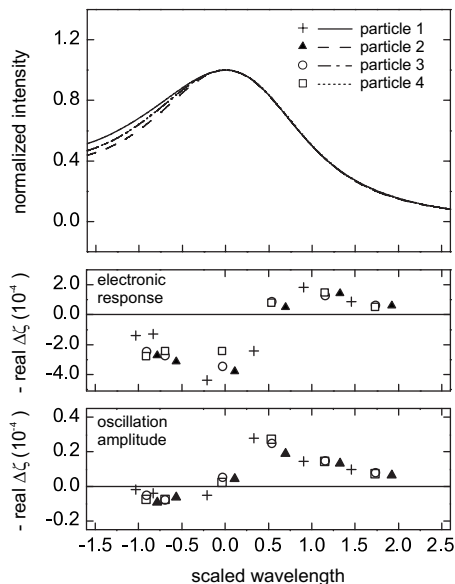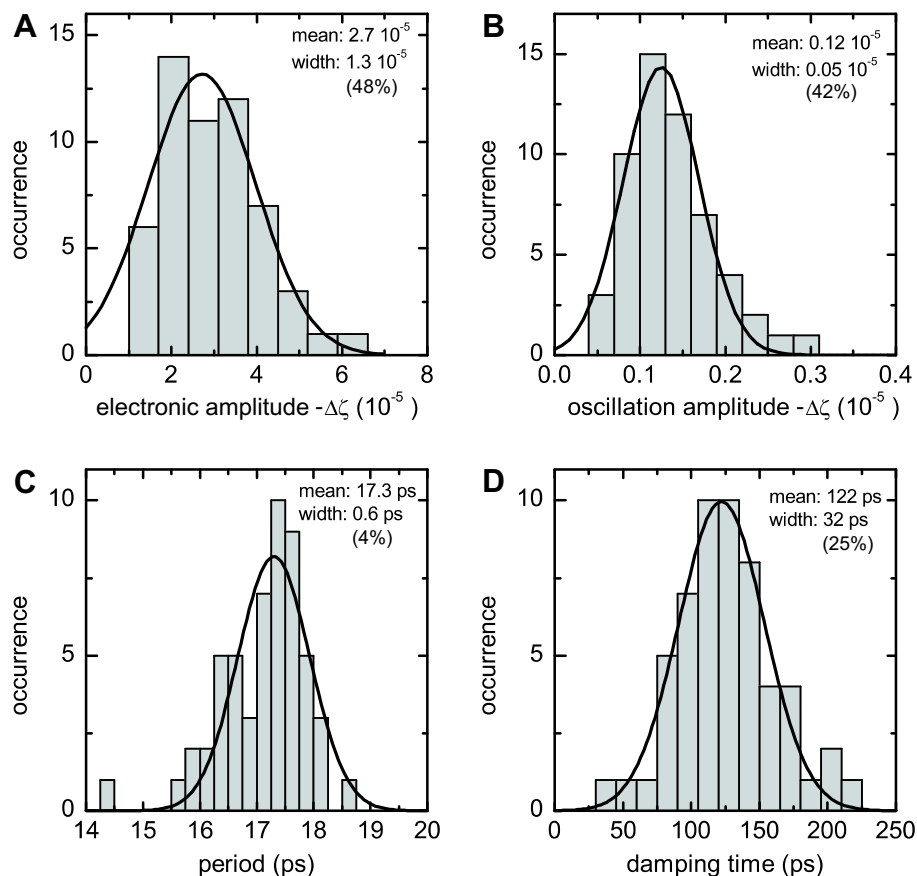
Figure 5.7: (A) Normalized absorption spectra of the 4 particles on a rescaled wavelength axis, where now all spectra fall one the same curve. The wavelength axis has been rescaled according to Eq. (5.5). (B) Electronic response for four different particles plotted against the rescaled wavelength. (C) Oscillation amplitude for four different particles plotted against the rescaled wavelength.

5.3   Statistical analysis of single-particle pump-probe dynamics

In order to gain more insight in the distribution of electronic and vibrational parameters of single gold particles within a sample, we have measured delay traces of many different particles under the same conditions, and have constructed histograms for the relevant parameters. Also shown here are first experiments on single gold nanoparticles coated with a layer of silica. For all experiments in this section, the probe wavelength was 590 nm. The sample preparation procedures were the same as explained in chapter 3.2. The BK7 substrates were cleaned with the procedure explained in chapter 3.2, the fused silica substrates were only ozone cleaned and did not undergo the KOH/acetone procedure.

We have measured delay traces of of 55 single gold nanoparticles with a nominal size of 60 nm, spincoated on BK7 glass. From the delay traces, we have determined the electronic amplitude by measuring the maximum

Figure 5.8: Histograms of fitted parameters of single-particle delay traces. Of 55 single particles, delay traces were measured under the same experimental conditions. Shown here are the magnitude of the first peak (electronic amplitude) (A), and the oscillation amplitude (B), period (C) and damping time (D). The particles have a nominal diameter of 60 nm, and were spincoated in a PVA solution on a cover slide of BK7 glass. All histograms could be fitted to a Gaussian distribution.

value of the first peak in the trace. The oscillation amplitude, period and damping time have been determined by fitting a damped cosine function to the oscillatory part of the trace. These parameters are plotted in histograms in Fig. 5.8. All histograms could be fitted to a Gaussian distribution.

The electronic amplitude (Fig. 5.8A) is expected to scale with the volume of the particle, since the detection method is based on absorption (see section 1.2). If the particles are assumed to be spherical and the environment
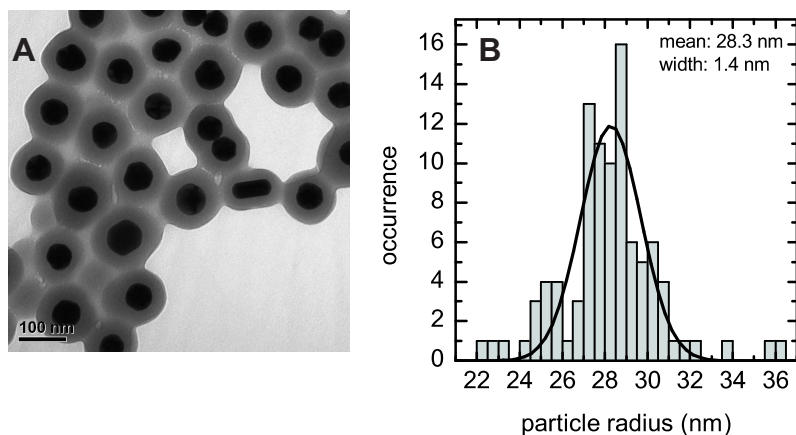
Figure 5.9: (A) TEM image of a sample of 60-nm gold nanoparticles coated with a 30-nm layer of silica (image by Peter Zijlstra). (B) Histogram of particle radii as determined from TEM images, assuming that the particles are spherical (the average circularity was 0.9, but this is neglected here). The mean radius is 28.3 nm, which does not correspond to the manufacturer's value of 30.1 nm. The width of the size distribution of the sample is 5%.

homogeneous, the width of this distribution should be 15%, three times the size distribution of the particles. The measured width of 50% is, however, much broader. There are a number of reasons for this. First of all, the method by which the peak value is determined is based on only one data point per delay trace, and is therefore prone to noise. Secondly, the particles are not spherical and the environment is not homogeneous, and these variations are amplified by the detection method. We measure a nonlinear effect, with the probe wavelength tuned to the most sensitive part of the spectrum, where $d\sigma/d\lambda$ is largest. As a result of this, small spectral variations are amplified, and broaden the distribution. The same holds for the oscillation amplitude (Fig. 5.8B), even though the spectral origin of this signal is different, as a result of which, the width of this distribution does not *a priori* have to be the same as that of the electronic response, even though here it is.

The histogram of vibration periods (Fig. 5.8C) is rather narrow, and with 4% very close to the size distribution as given by the manufacturer, which fits expectations, since the vibration period scales linearly with the size of the particle [17]. From the mean period, the average radius of the particles can be determined. Analysis of TEM images (Fig. 5.9, of particles from the same batch but coated with a 30-nm layer of silica, and assuming that the particles are spherical) yielded an average radius of 28.3 nm and a size distribution of

5%. Calculated vibration periods and damping times for a gold nanoparticle with a radius of 28 nm are given in Table 1.2 on page 30. From our experimental conditions, we would expect the vibration period to lie somewhere between the period of a gold nanoparticle fully embedded in glass and of the period of a free sphere (the period of a particle embedded in PVA falls in between these two values). The vibrational periods belonging to a 28.3 nm particle under those circumstances are 17.5 ps (embedded) and 18.6 ps (free). Our detected average value of 17.3 ps falls outside this range and is shorter than expected. The reason for this deviation is not clear, but may be related to the shape of the particles, since TEM analysis yielded an average circularity of 0.9. Another explanation could be that the sound velocities inside nanoparticles differ from bulk values.

The damping times that are collected in the histogram in Fig. 5.8D are homogeneous damping times. These can be directly studied for the first time, since the single-particle experiments are not hampered by inhomogeneous broadening, inevitable for ensemble measurements. We find a mean damping time of 122 ps, with a width of 25%. The width is again much larger than expected, since the damping times are predicted to scale linearly with the size of the particle, according to the complex-frequency model presented in section 1.3 and [50]. The larger width is most probably caused by local differences in elastic coupling between the particles and the medium. The average damping time is found to be in between calculated values for a sphere homogeneously surrounded by BK7 and by PVA (see Table 1.2 on page 30), but very close to the estimated value for PVA. That suggests that the PVA film is dominant for the damping, even though this film only partly surrounds the particle.

The same experiment was carried out for particles spincoated on a fused silica substrate, again in a layer of PVA (data not shown). No significant differences in the distributions of parameters as compared to the BK7 data have been observed. Since the acoustic impedances are almost identical for BK7 and fused silica [50], not much difference is expected.

We have plotted the detected electronic and vibrational responses from Fig. 5.8 against each other in scatter plots in Fig. 5.10, to visualize how the parameters are correlated. There is a strong correlation between the electronic and oscillation amplitude (Fig. 5.10A), since both parameters directly scale with the strength of the plasmon. The period and the damping time, between which a linear correlation is expected [50], show only very little correlation (Fig. 5.10B). The correlation between the oscillation amplitude and the period is also very weak (Fig. 5.10C), which means that the oscillation amplitude and
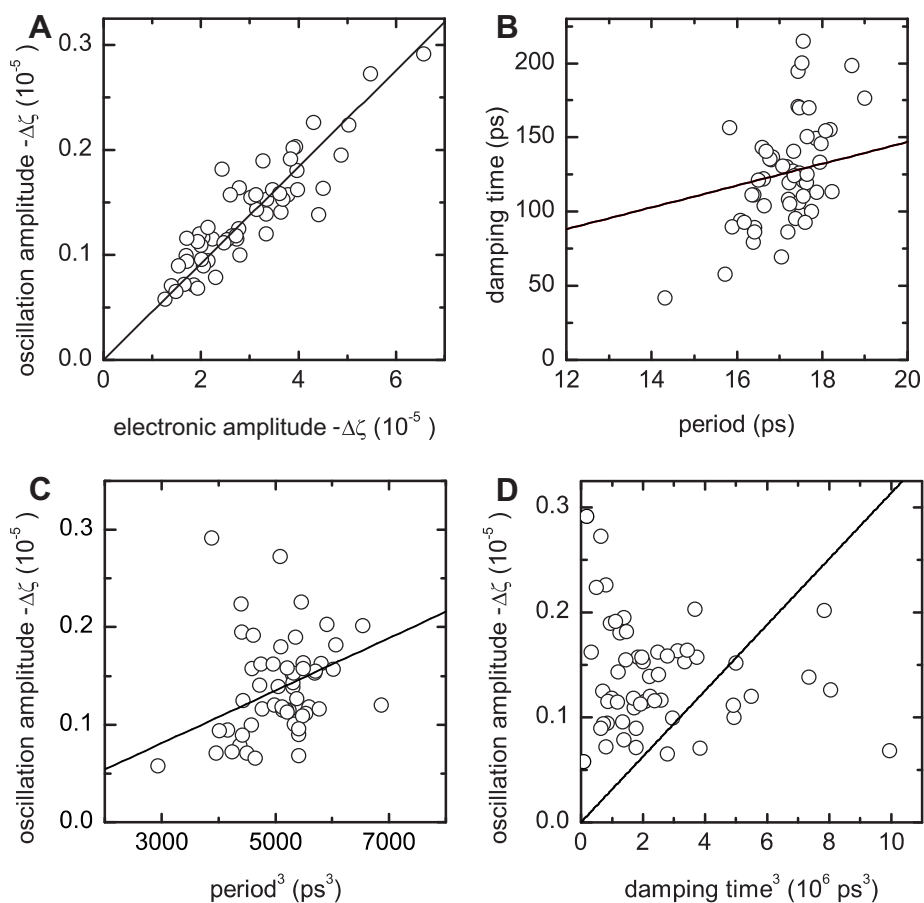
Figure 5.10: Correlation of the electronic and vibrational properties of single gold nanoparticles. The solid lines are linear fits through the origin, the open circles are the data points that were plotted in histograms in Fig. 5.8. (A) The electronic and oscillation amplitudes show a very strong correlation. (B) The period and damping time are expected to scale linearly. The correlation is weak. (C) The oscillation amplitude is expected to scale with the volume of the particle, so we should find a linear dependence of the oscillation amplitude on the third power of the period. This correlation is very weak. (D) The correlation between the oscillation amplitude and the damping time is completely absent.

the damping time are, within this size distribution, only weakly influenced by particle size. Between the oscillation amplitude and the damping time (Fig. 5.10D), there is no correlation at all.

A conclusion that can be drawn from the correlations and the widths of the histograms, is that both the surface plasmon resonance and the damping time are highly influenced by the local environment. For the electronic and oscillation amplitudes as well as for the damping time, there is hardly any size dependence observed within the particle distribution. The vibration period on the other hand, is hardly affected by the local environment. The distribution of detected periods can be fully explained from the size distribution of the sample.

A sample from the same batch was coated with a layer of silica by Peter Zijlstra and James Chon (Swinburne University Melbourne), using a method by LizMarzan et al. [9, 109]. A TEM image in which the coating is clearly visible is shown in Fig. 5.9A. Since aggregation of the particles in a PVA solution was feared, they were spincoated without PVA on fused silica glass. Delay traces were measured for 87 particles, and the corresponding histograms are shown in Fig. 5.11. The distribution of electronic amplitudes in Fig. 5.11A is not monomodal. Two peaks appear, both can be fitted with Gaussian distributions and the center of the second peak is twice as high as the center of the first peak. Very likely, double particles cause the second peak. These particles are not so close together that their plasmons influence each other, which would lead to a red shift of the absorption spectrum as observed in Fig. 5.2C, but close enough to fall in the focal volume together. The reason for observing pairs is not completely clear. It might be that the silica coating favors aggregation, it could be caused by the fact that the substrates were not cleaned with KOH and acetone before spincoating (as the BK7 substrates were), or it could be caused by the absence of PVA, which may increase the probability of agregation during spincoating. We have also observed pair formation for uncoated particles, spincoated in PVA on (uncleaned) fused silica samples, so likely, the substrate-cleaning procedure was responsible for the pair formation.

We have made a separation between single and double particles by introducing a threshold for the electronic amplitude. All particles with an amplitude above $\Delta\zeta = 3 \times 10^{-5}$ (absolute value) are classified as pairs. Obviously, in this way we will classify some single particles as doubles and vice versa, since the distributions overlap, so we have chosen the threshold as low as possible, at least to minimize the occurrence of double particles in the single-particle distribution. Figures. 5.11B, C and D, show the result of the separa-
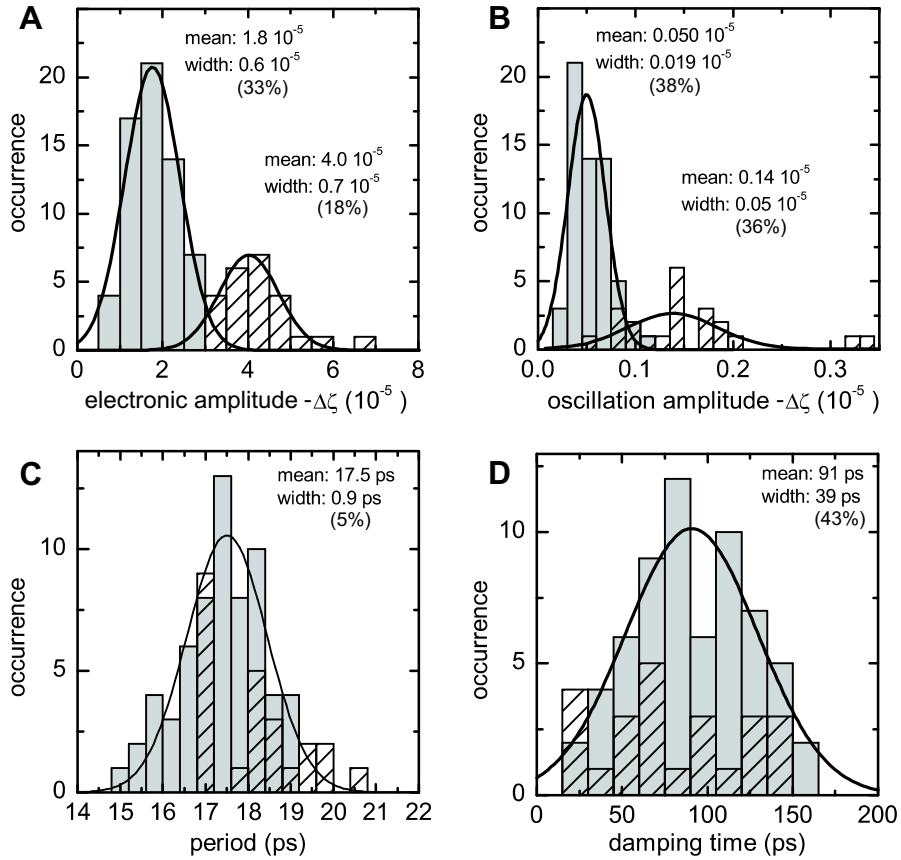
Figure 5.11: Histograms of fitted parameters of delay traces of silica-coated particles. Of 87 particles, delay traces were measured under the same experimental conditions. Shown here are the electronic amplitude (A), and the oscillation amplitude (B), period (C) and damping time (D). The particles were spincoated on a substrate of fused silica, without PVA. In contrast to the uncoated particles on BK7 glass, the electronic amplitude clearly shows two distributions. Most probably, a part of the distribution contains double particles. We have separated the single particles (grey bars) from the double particles (striped bars) using a threshold for the electronic amplitude.
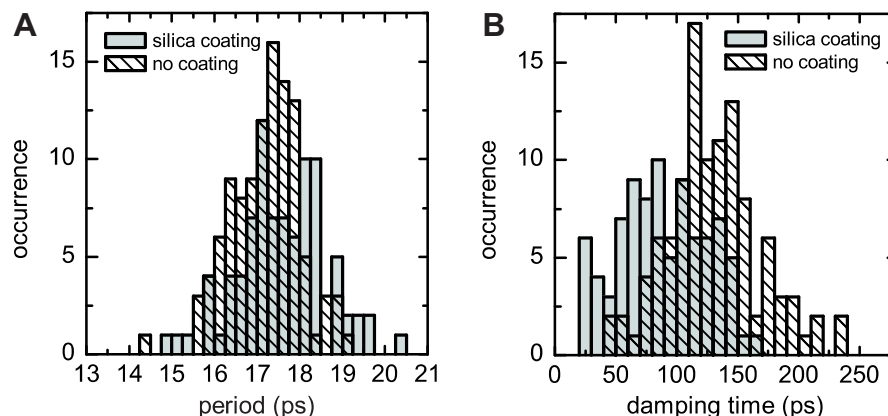
Figure 5.12: Comparison of detected period (A) and damping time (B) for large numbers of coated and uncoated gold nanoparticles. For both histograms, the number of particles is approximately 100. The uncoated particles were measured in a layer of PVA on BK7 or SiO_2 glass. The coated particles were measured without PVA on a SiO_2 substrate. The thickness of the layer was approximately 30 nm.

tion for the oscillation amplitude, period and damping time. Also for the oscillation amplitude, two distributions can be distinguished, and the particles that were classified as pairs are also here mainly in the brightest distribution. For the vibration period and the damping time, there is no clear difference between the single and the double particles, although in the distribution of the vibration period, there seems to be a small bias towards longer periods, which may be partly due to a wrong classification of large single particles as double particles.

In comparison with the uncoated particles, the coated particles damp much faster. The mean damping time is 90 ps for the selected single particles, with a width of 43%. Including the pairs did not change the mean damping time, but did increase the width of the distribution slightly, to 50%. The mean period of the selected single distribution is 17.5 ps, with a width of 5%. Here the selection seemed to be slightly biased towards smaller particles and indeed, if we include the double particles, the mean period increases slightly, to 17.6 ps, still with a width of 5%.

In order to compare the vibrational properties of coated and uncoated particles, we have plotted distributions of the vibration period and damping time of coated and uncoated particles together in Fig. 5.12. We have included the particles that were classified as doubles earlier in these distributions, since belonging to a pair does not influence the period and there was no evidence

for dephasing from comparing the damping times of single and double particles, and we have also included the uncoated particles on a fused silica substrate. The Gaussian fits of Figs. 5.8C and 5.11C returned periods of 17.3 ps for uncoated particles and 17.6 ps for coated particles, and also a statistical calculation of the average periods yielded a slight difference: 17.2 ± 0.1 ps for the uncoated particles and 17.6 ± 0.1 ps for the uncoated particles, the error here is the standard error of the mean. The damping times show a larger difference. The Gaussian fits returned values of 126 ps for the uncoated particles and 86 ps for the coated particles, with widths of 26% and 48% respectively. A statistical calculation resulted in mean values of 130 ± 4 ps and 89 ± 4 ps, with standard deviations of 29% and 41%. It has to be noted that in the experiments with uncoated particles, the particles were partly embedded in a layer of PVA, which was absent in the experiments with coated particles. Though the vibration period is not very sensitive for the environment of the particle, the damping time is very much so, which means that the comparison is not completely correct. That said, the presence of PVA decreases the damping time, since the impedance mismatch with gold is larger for air than for PVA. Therefore, the observed difference in damping time would only be larger if the two experiments would have been done in the same matrix.

The change in vibration period can be explained from the added mass of the silica shell. Sader et al. have modelled the vibrations of core-shell particles [110], and predict a decrease in frequency to 85% of the frequency of an uncoated particle, taking the bulk values of the density and sound velocities of SiO_2. We see a much smaller shift, to 97%. This may well be caused by a difference in density and sound velocity of our shell, which is thin and porous, with an air content of 10-20%, compared to bulk values.

The average damping time that we find for the coated particles is close to the calculated value for a sphere embedded in a SiO_2 matrix. The differences may be explained by the fact that our shell is thin and porous. This could first of all lead to deviations from the bulk values for the density and the sound velocities of SiO_2. Secondly, the complex-frequency model assumes that the environment extends to infinity, which it clearly does not in the experiment. This will most probably also lead to deviations in the calculated values.

To summarize this section, we have conducted a statistical analysis of electronic and vibrational properties of single gold nanoparticles. It was shown that both the plasmon resonance and the vibrational damping time were strongly dependant on the local environment, which is promising for applying gold nanoparticles as local probes of acoustic and optical properties of materials. Time-resolved experiments on single gold nanoparticles coated

with a layer of silica revealed an influence of the coating on the vibrational periods and damping times of the particles.

5.4 A closer look at ellipsoidal deformation
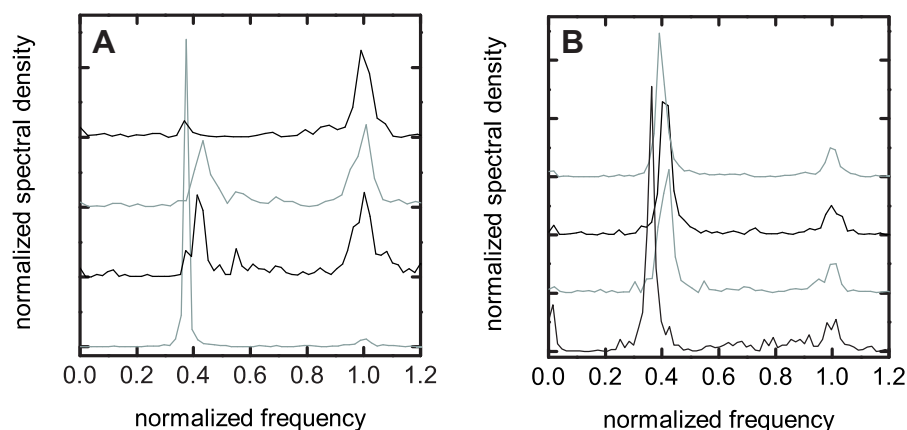
Figure 5.13: Examples of Fourier spectra of gold nanoparticles for which ellipsoidal deformation is observed. For all particles, the frequency was normalized to the frequency of the breathing mode, using a fit to a Lorentzian. Uncoated particles (A) and silica-coated particles (B) did not show a significant difference in the ratio between the breathing mode and the ellipsoidal mode. For both configurations a small variation in this ratio, between 0.37 and 0.42, has been detected. The resolution of the traces is 1 GHz. The spectral density of all traces has been normalized to the spectral density of the breathing mode, except for the bottom trace in (A) which has been normalized to $0.1\times$ the spectral density of the breathing mode. The spectra are offset for clarity.

In this section we discuss more detailed measurements on particles that undergo ellipsoidal deformation, which was shown for the first time in section 4.5. The main question we try to answer is why we see this signal only for a rare number of particles, and if we see it, why it is so strong. In section 4.5, we discussed the necessity of a broken symmetry to launch the ellipsoidal mode, and we suggested that the glass substrate was responsible for this symmetry breaking. By correlating white-light spectra to vibrational properties and by examining the influence of the probe wavelength on the ellipsoidal mode, here we try to test this hypothesis. The experimental method was similar to that of the previous section. Unless otherwise mentioned, all measurements in this section were done with a probe wavelength of 590 nm.

The acoustic spectra shown in this section were obtained from Fourier transforms of measured delay traces.

Figure 5.13 shows examples of Fourier spectra for particles that undergo an ellipsoidal deformation, for uncoated particles as well as for particles coated with a layer of silica. For all spectra, the frequency axis was normalized to the frequency of the breathing mode. We do not see a difference in the frequency ratio between the ellipsoidal mode and the breathing mode for uncoated (Fig. 5.13A) and coated (Fig. 5.13B) particles. We did however for both samples observe a slight variation between the particles, the ratio ranging between 0.37 and 0.43. Also, it appears for some of the particles that the breathing mode is split. Some care needs to be taken in claiming the observation of split lines, since the magnitude of the splitting is comparable to the noise level. We have however in some cases observed multiple measurements of split lines in which the dip appeared always at the same frequency.

We have correlated FFT spectra to white-light scattering spectra (Fig. 5.14) for particles that showed ellipsoidal information. The white-light spectra were measured using the method explained in section 5.2.1. These experiments were done on the air-glass interface, where the background from reflection from the interface is much higher than on a nearly index-matched interface of glass and immersion oil, as was used in section 5.2. As a result, the Xenon lamp was not powerful enough as a light source and we used a tapered fiber generating a supercontinuum white light (NT&C, Stuttgart) in-
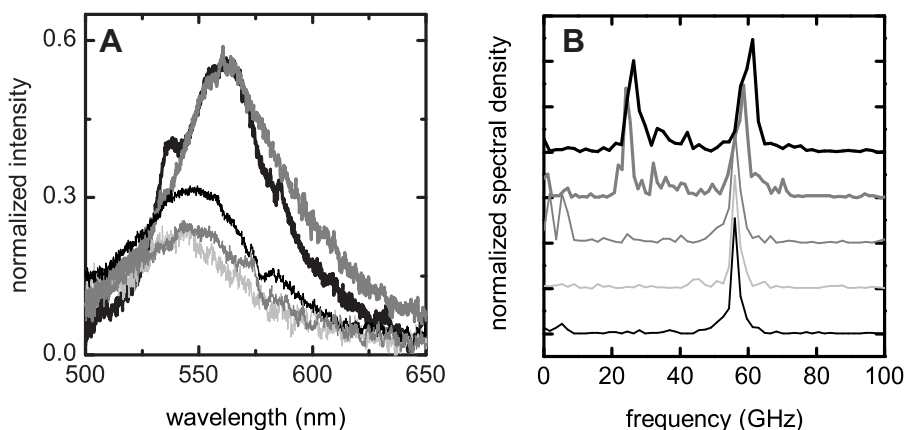
Figure 5.14: Correlation between white-light spectra (A) and Fourier spectra (B) for particles that show ellipsoidal deformation. Each different color represents a different particle and the color coding is the same for both (A) and (B). The spectra are offset for clarity and normalized to the spectral density of the breathing mode.
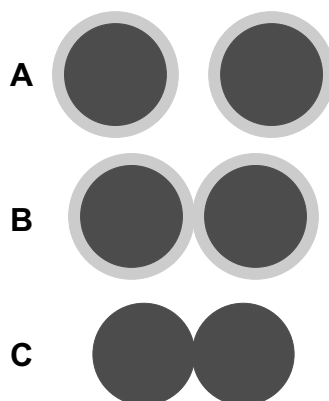
Figure 5.15: Sketch of the possible configurations for close pairs of nanoparticles. In (A) and (B), the particles are surrounded by a thin organic capping layer, whose thickness is estimated to be in the order of 1 nm. In (A), the particles are well separated, and there is no interaction. In (B), the capping layers touch, but there is no electronic contact between the particles. In (C) a touching conformation without capping layer is sketched. In this configuration, the electrons are delocalized over the two particles.

stead. Slight fluctuations in power and spectral shape of this source in combination with the small signal-to-noise ratio made it difficult to record stable spectra. Fig. 5.14A shows spectra of five different particles. The corresponding spectra are plotted in Fig. 5.14B, where the color coding is the same as in A. Although the spectra show some random fluctuations, the spectra of particles that show ellipsoidal deformation (thick lines) are remarkably different from the others (thin lines); the peak intensity is higher and the spectra are significantly red shifted.

These results point towards a different origin of the ellipsoidal deformation than the explanation that was suggested earlier. We find strong evidence that it is not the glass surface but a second particle, in mechanical contact, that is the cause of the symmetry breaking. It is important to clarify the various configurations for a pair of particles that are in close proximity. A sketch of the possibilities is given in Fig. 5.15. To stabilize the particles in solution, and to prevent aggregation, our particles are surrounded by an organic capping layer, with a thickness in the order of 1 nm. This capping layer is drawn in light grey in the figure. Two particles can be close enough to fall in the same focal volume, but too far from each other to have any mutual influence (Fig. 5.15A). This configuration was seen in Fig. 5.11. If their distance decreases, the particles come close enough for their plasmons to polarize each

other (Fig. 5.15B). This will create a longitudinal plasmon, an additional red-shifted mode in the spectrum. In the configuration sketched in Fig. 5.15B, the particles are in mechanical contact, since the capping layers touch, but electronic contact (i.e. delocalization of the electrons over the two particles) is prevented by the capping layer. In Fig. 5.15C, a configuration is drawn in which the capping layer is removed (e.g. by an intense laser beam or an electron beam). In this case, the electrons are delocalized over both particles, creating a single system with the shape of a dumbbell. This will lead to a dramatic red shift of the longitudinal mode and a large change in the vibrational properties of the particles. In a recent study, Danckwerts and Novotny [111] have calculated scattering spectra for two gold nanoparticles as a function of their mutual distance. They found that upon approach, there is a gradual red shift of the spectrum, but as soon as the particles touch electronically, the spectrum undergoes a sudden red shift towards near-infrared wavelengths.

Our experimental observations agree with the conformation in Fig. 5.15B as the origin of the strong ellipsoidal mode. The organic layer prevents electronic contact between the particles, but can act as a spring to transfer mechanical energy, launching the ellipsoidal deformation of the particles. First of all, the splitting of the line of the breathing mode (see Fig. 5.13), as well as the strong electronic amplitude for particles with ellipsoidal deformation (which can be three to four times above the average signal), suggest that more than one particle is present in the focal volume. Secondly, the red-shifted plasmon suggests that we see a mode associated with a longitudinal deformation. If we compare the spectra with those of Ref. [111], we see that the two spectra drawn with thick lines in Fig. 5.14 are consistent with an inter-particle distance in the order of 1 nm, but not with a configuration with electronic contact. Also, the ratio between the breathing mode and the ellipsoidal mode that we detect is consistent with that of a sphere (see Table 1.1 on page 27), which implies that we detect vibrations of spheres and not of dumbbell systems. Although it is difficult to calculate the vibrational frequencies for a dumbbell system as in Fig. 5.15C (the frequencies will depend largely on the contact area), surely the ratio between the breathing mode and the ellipsoidal mode will be different for a dumbbell than for a sphere.

If the ellipsoidal mode is indeed connected to a longitudinal plasmon, we would expect this mode to become stronger if the probe wavelength is longer. Figure 5.16 shows an experiment in which the delay traces of 3 particles were measured at three different probe wavelengths: 570 nm, 590 nm, and 625 nm. The Fourier spectra were then normalized to the spectral density of the ellipsoidal mode, which was determined with a fit to a Lorentzian line shape.
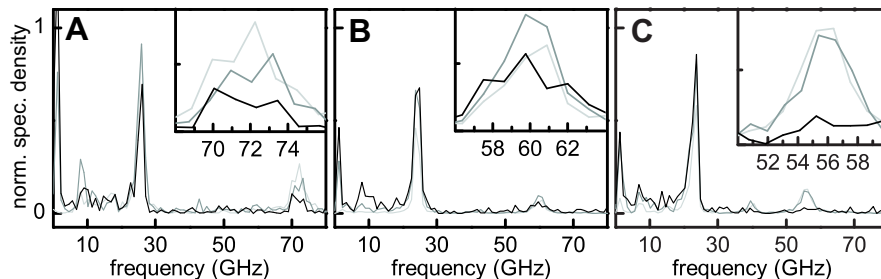
Figure 5.16: Wavelength dependence of the relative intensity of the ellipsoidal mode. Three different particles are shown in panels (A), (B) and (C) respectively. Each particle was measured with three different probe wavelengths, 570 nm (light grey in B and C), 575 nm (light grey in A), 590 nm (dark grey) and 625 nm (black). The spectra were then normalized to the intensity of the ellipsoidal mode, using a fit to a Lorentzian. The insets show an enlargement of the lines of the breathing mode. Note that a third peak appears at 40 GHz for the third particle.

For two of the three particles, the relative intensity of the breathing mode is lower for a longer pump wavelength. This strongly suggests a link between the longitudinal plasmon and the ellipsoidal-deformation mode.

As a final remark, we state that the fact alone that we detect the ellipsoidal mode for coated particles, rules out the glass surface as a source of the symmetry breaking. In TEM images of many coated particles, we did not find any uncoated particles, so all particles were embedded in a relatively homogeneous environment. We did find several occurrences of two particles within a single coating.

The final question that remains is whether we can detect the ellipsoidal mode for particles of which we are sure that they are single. The answer to that question is shown in Fig. 5.17, where we have added all the Fourier transforms of the traces of the uncoated particles of which the statistical analysis was shown in Fig. 5.8, after their frequencies were normalized to the frequency of their breathing mode. In Fig. 5.17A, where this was done for the particles spincoated on BK7 glass, a peak rises out of the background at a frequency of approximately 0.4 times the frequency of the breathing mode, exactly where we find the ellipsoidal mode. Although we cannot exclude the possibility that this peak is caused by noise, this could mean that there is a very weak trace of the ellipsoidal mode present in the single particles as well, one that could not be detected in the individual contributions. Note that if this peak is indeed noise, we can at least define it as the upper limit for the strength of the ellipsoidal mode for single particles. For particles spincoated
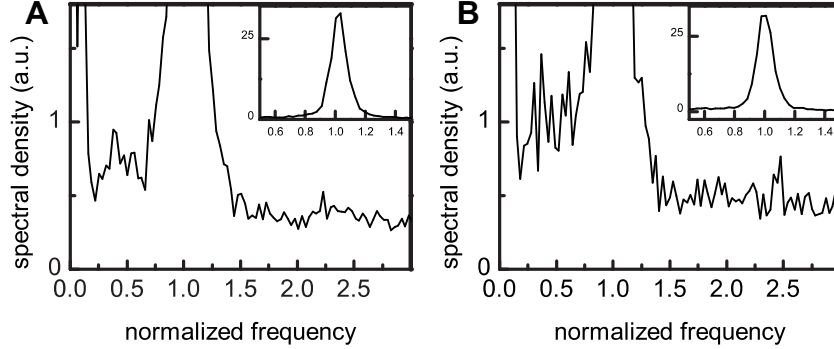
Figure 5.17: Summation of frequency-normalized Fourier spectra of single gold nanoparticles on BK7 glass (A) and fused silica glass (B). Fourier spectra of around 50 delay traces of particles spincoated in PVA on either BK7 glass or fused silica glass were fitted to a Lorentzian. The frequency axis was then normalized to the frequency of the breathing mode that was returned by the fit, before all traces were added. In (A), a peak can be seen rising out of the background at a normalized frequency of 0.4. Note that in both (A) and (B), it appears as if there is a very weak signal rising above the background at normalized frequencies between 2 and 2.5. If this is indeed a signal, it is probably a trace of the $(n, l) = (1, 0)$ mode.

on SiO_2 (Fig. 5.17B), there is an increase in the spectral density below the breathing mode, but no clear peak can be distinguished. This implies a huge amplification of the ellipsoidal mode by the second particle. The ellipsoidal mode in Fig. 5.17 is estimated to be at least 100 times smaller than the breathing mode (note that this number should be regarded as a lower limit), while the ellipsoidal mode can be equally large or even larger than the breathing mode if a second particle is present.

In conclusion, we did not find significant differences in ellipsoidal deformation between free and silica-coated particles. We found slight variations in the frequency ratio of the ellipsoidal mode and the breathing mode that may be due to splitting of the ellipsoidal mode. Most importantly, several observations all point to the proximity of a second particle, separated by the organic capping layer electronically but not mechanically, as the trigger of the ellipsoidal deformation. Electron microscopy could confirm this conclusion, since it can directly visualize two connected particles. For such measurements, care needs to be taken of the order in which the electron microscopy and pump-probe experiments are executed, since the electron beam will burn the protective capping layer away from the particles, thereby completely changing their behavior.

5.5   Conclusion

In this chapter, several experiments in which optical properties are correlated with the structure of individual particles have been presented. Using white light scattering, we could combine pump-probe experiments with a measurement of the absorption spectrum. This confirmed theories and earlier experiments on the origin of the detected phenomena, but unfortunately, a quantitative comparison of calculations with the experiment was not possible. Statistical analysis of large numbers of single-particle pump-probe parameters gave promising results for the utilization of the acoustic vibrations of single gold particles as local probes of acoustic parameters of a medium. Finally, several experiments on particles that showed ellipsoidal deformation could identify mechanical coupling of two nanoparticles as the origin of the strong amplitude of the ellipsoidal modes.

Nevertheless, the experiments are still hampered by uncertainties, caused by inhomogeneous environments and uncertainties about the shape of the particles. Also, possible deviations of the acoustic parameters of gold on the nano scale might lead to unexpected results. Eventually, we expect that experiments in more homogeneous media and correlation of pump-probe experiments with electron microscopy on the same particle, can lift these uncertainties one by one.

5 Correlation of optical and structural properties

,

Bibliography

[1] M. Salerno, J. R. Krenn, B. Lamprecht, G. Schider, H. Ditlbacher, N. Felidj, A. Leitner, and F. R. Aussenegg, "Plasmon polaritons in metal nanostructures: the optoelectronic route to nanotechnology," Opto-Electron. Rev. **10**(3), 217–224 (2002).

[2] J. R. Krenn, "Nanoparticle waveguides - Watching energy transfer," Nat. Mater. **2**(4), 210–211 (2003).

[3] S. A. Maier, P. G. Kik, H. A. Atwater, S. Meltzer, E. Harel, B. E. Koel, and A. A. G. Requicha, "Local detection of electromagnetic energy transport below the diffraction limit in metal nanoparticle plasmon waveguides," Nat. Mater. **2**(4), 229–232 (2003).

[4] W. L. Barnes, A. Dereux, and T. W. Ebbesen, "Surface plasmon subwavelength optics," Nature **424**(6950), 824–830 (2003).

[5] Y. H. Liau, A. N. Unterreiner, Q. Chang, and N. F. Scherer, "Ultrafast dephasing of single nanoparticles studied by two-pulse second-order interferometry," J. Phys. Chem. B **105**(11), 2135–2142 (2001).

[6] D. Yelin, D. Oron, S. Thiberge, E. Moses, and Y. Silberberg, "Multiphoton plasmon-resonance microscopy," Optics Express **11**(12), 1385–1391 (2003).

[7] J. Nappa, G. Revillod, I. Russier-Antoine, E. Benichou, C. Jonin, and P. F. Brevet, "Electric dipole origin of the second harmonic generation of small metallic particles," Phys. Rev. B **71**(16), 165,407 (2005).

[8] H. Ditlbacher, J. R. Krenn, B. Lamprecht, A. Leitner, and F. R. Aussenegg, "Spectrally coded optical data storage by metal nanoparticles," Opt. Lett. **25**(8), 563–565 (2000).

[9] J. W. M. Chon, C. Bullen, P. Zijlstra, and M. Gu, "Spectral encoding on gold nanorods doped in a silica sol-gel matrix and its application to high-density optical data storage," Adv. Funct. Mater. **17**(6), 875–880 (2007).

[10] K. Kneipp, H. Kneipp, I. Itzkan, R. R. Dasari, and M. S. Feld, "Surface-enhanced Raman scattering and biophysics," J. Phys.-Condes. Matter **14**(18), R597–624 (2002).

[11] H. G. Boyen, G. Kastle, F. Weigl, B. Koslowski, C. Dietrich, P. Ziemann, J. P. Spatz, S. Riethmuller, C. Hartmann, M. Moller, G. Schmid, M. G. Garnier, and P. Oelhafen, "Oxidation-resistant gold-55 clusters," Science **297**(5586), 1533–1536 (2002).

[12] J. Yguerabide and E. E. Yguerabide, "Light-scattering submicroscopic particles as highly fluorescent analogs and their use as tracer labels in clinical and biological applications- II. Experimental characterization," Anal. Biochem. **262**(2), 157–176 (1998).

[13] G. Raschke, S. Kowarik, T. Franzl, C. Sönnichsen, T. A. Klar, J. Feldmann, A. Nichtl, and K. Kurzinger, "Biomolecular recognition based on single gold nanoparticle light scattering," Nano Lett. **3**(7), 935–938 (2003).

[14] P. K. Jain, I. H. El-Sayed, and M. A. El-Sayed, "Au nanoparticles target cancer," Nano Today **2**(1), 18–29 (2007).

[15] S. Link and M. A. El-Sayed, "Size and temperature dependence of the plasmon absorption of colloidal goldnanoparticles," J. Phys. Chem. B **103**(21), 4212–4217 (1999).

[16] C. Voisin, N. Del Fatti, D. Christofilos, and F. Vallée, "Ultrafast electron dynamics and optical nonlinearities in metal nanoparticles," J. Phys. Chem. B **105**(12), 2264–2280 (2001).

[17] G. V. Hartland, "Measurements of the material properties of metal nanoparticles by time-resolved spectroscopy," Phys. Chem. Chem. Phys. **6**(23), 5263–5274 (2004).

[18] B. Lamprecht, J. R. Krenn, A. Leitner, and F. R. Aussenegg, "Resonant and off-resonant light-driven plasmons in metal nanoparticles studied by femtosecond-resolution third-harmonic generation," Phys. Rev. Lett. **83**(21), 4421–4424 (1999).

[19] S. Link and M. A. El-Sayed, "Shape and size dependence of radiative, non-radiative and photothermal properties of gold nanocrystals," Int. Rev. Phys. Chem. **19**(3), 409–453 (2000).

[20] E. Dulkeith, T. Niedereichholz, T. A. Klar, J. Feldmann, G. von Plessen, D. I. Gittins, K. S. Mayya, and F. Caruso, "Plasmon emission in photoexcited gold nanoparticles," Phys. Rev. B **70**(20), 205,424 (2004).

[21] B. Palpant, H. Portales, L. Saviot, J. Lerme, B. Prevel, M. Pellarin, E. Duval, A. Perez, and M. Broyer, "Quadrupolar vibrational mode of silver clusters from plasmon-assisted Raman scattering," Phys. Rev. B **60**(24), 17,107–17,111 (1999).

[22] Special issue on Single Molecules, Science **283**(5408), 1593–1804 (1999).

[23] P. Tamarat, A. Maali, B. Lounis, and M. Orrit, "Ten years of single-molecule spectroscopy," J. Phys. Chem. A **104**(1), 1–16 (2000).

[24] X. Michalet, F. Pinaud, T. D. Lacoste, M. Dahan, M. P. Bruchez, A. P. Alivisatos, and S. Weiss, "Properties of fluorescent semiconductor nanocrystals and their application to biological labeling," Single Mol. **2**(4), 261–276 (2001).

[25] G. Mie, "Beiträge zur Optik trüber Medien, speziell kolloidaler Metallösungen," Ann. Physik **330**(3), 377–442 (1908).

[26] C. F. Bohren and D. R. Huffman, *Absorption and Scattering of Light by Small Particles* (Wiley, 1998).

[27] P. B. Johnson and R. W. Christy, "Optical-Constants Of Noble-Metals," Phys. Rev. B **6**(12), 4370–4379 (1972).

[28] U. Kreibig and M. Vollmer, *Optical Properties of Metal Clusters*, vol. 25 of *Springer Series in Materials Science* (Springer, Berlin, 1995).

[29] M. Otter, "Temperaturabhängigkeit Der Optischen Konstanten Massiver Metalle," Z. Phys. **161**(5), 539–549 (1961).

[30] F. Ercolessi, W. Andreoni, and E. Tosatti, "Melting Of Small Gold Particles - Mechanism And Size Effects," Phys. Rev. Lett. **66**(7), 911–914 (1991).

[31] G. V. Hartland, M. Hu, and J. E. Sader, "Softening of the symmetric breathing mode in gold particles by laser-inducedheating," J. Phys. Chem. B **107**(30), 7472–7478 (2003).

[32] A. Plech, V. Kotaidis, S. Gresillon, C. Dahmen, and G. von Plessen, "Laser-induced heating and melting of gold nanoparticles studied by time-resolved x-ray scattering," Phys. Rev. B **70**(19), 195,423 (2004).

[33] S. Inasawa, M. Sugiyama, and Y. Yamaguchi, "Laser-induced shape transformation of gold nanoparticles below the melting point: The effect of surface melting," J. Phys. Chem. B **109**(8), 3104–3111 (2005).

[34] H. C. van de Hulst, *Light Scattering by Small Particles* (Dover Publications, 1981).

[35] R. W. Schoenlein, W. Z. Lin, J. G. Fujimoto, and G. L. Eesley, "Femtosecond studies of nonequilibrium electronic processes in metals," Phys. Rev. Lett. **58**(16), 1680–1683 (1987).

[36] S. D. Brorson, A. Kazeroonian, J. S. Moodera, D. W. Face, T. K. Cheng, E. P. Ippen, M. S. Dresselhaus, and G. Dresselhaus, "Femtosecond Room-Temperature Measurement Of The Electron-Phonon Coupling Constant Lambda In Metallic Superconductors," Phys. Rev. Lett. **64**(18), 2172–2175 (1990).

[37] R. H. J. Kop and R. Sprik, "Phase-sensitive interferometry with ultrashort optical pulses," Rev. Sci. Instrum. **66**(12), 5459–5463 (1995).

[38] M. Nisoli, S. DeSilvestri, A. Cavalleri, A. M. Malvezzi, A. Stella, G. Lanzani, P. Cheyssac, and R. Kofman, "Coherent acoustic oscillations in metallic nanoparticles generated with femtosecond optical pulses," Phys. Rev. B **55**(20), 13,424–13,427 (1997).

[39] J. H. Hodak, I. Martini, and G. V. Hartland, "Observation of acoustic quantum beats in nanometer sized Au particles," J. Chem. Phys. **108**(22), 9210–9213 (1998).

[40] N. Del Fatti, S. Tzortzakis, C. Voisin, C. Flytzanis, and F. Vallée, "Time resolved investigation of coherent acoustic mode oscillations in silver nanoparticles," Physica B **263**, 54–56 (1999).

[41] G. V. Hartland, "Coherent vibrational motion in metal particles: Determination of the vibrationalamplitude and excitation mechanism," J. Chem. Phys. **116**(18), 8048–8055 (2002).

[42] M. Hu and G. V. Hartland, "Heat dissipation for Au particles in aqueous solution: Relaxation time versus size," J. Phys. Chem. B **106**(28), 7029–7033 (2002).

[43] J. H. Hodak, A. Henglein, and G. V. Hartland, "Size dependent properties of Au particles: Coherent excitation and dephasing of acoustic vibrational modes," J. Chem. Phys. **111**(18), 8613–8621 (1999).

[44] M. Perner, S. Gresillon, J. Marz, G. von Plessen, J. Feldmann, J. Porstendorfer, K. J. Berg, and G. Berg, "Observation of hot-electron pressure in the vibration dynamics of metal nanoparticles," Phys. Rev. Lett. **85**(4), 792–795 (2000).

[45] H. Lamb, "On the Vibrations of an Elastic Sphere," Proc. London Math. Soc. **13**, 189–212 (1882).

[46] L. Saviot, B. Champagnon, E. Duval, I. A. Kudriavtsev, and A. I. Ekimov, "Size dependence of acoustic and optical vibrational modes of CdSe nanocrystalsin glasses," J. Non-Cryst. Solids **197**(2-3), 238–246 (1996).

[47] J. Park, T. R. A. Song, J. Tromp, E. Okal, S. Stein, G. Roult, E. Clevede, G. Laske, H. Kanamori, P. Davis, J. Berger, C. Braitenberg, M. Van Camp, X. Lei, H. P. Sun, H. Z. Xu, and S. Rosat, "Earth's free oscillations excited by the 26 December 2004 Sumatra-Andaman earthquake," Science **308**(5725), 1139–1144 (2005).

[48] D. B. Murray and L. Saviot, "Acoustic vibrations of embedded spherical nanoparticles," Physica E **26**(1-4), 417–421 (2005).

[49] V. A. Dubrovskiy and V. S. Morochnik, "Natural vibrations of a spherical inhomogeneity in an elastic medium," Izv. Earth Phys. **17**, 494–504 (1981).

[50] C. Voisin, D. Christofilos, N. Del Fatti, and F. Vallée, "Environment effect on the acoustic vibration of metal nanoparticles," Physica B **316**, 89–94 (2002).

[51] D. B. Murray and L. Saviot, "Phonons in an inhomogeneous continuum: Vibrations of an embedded nanoparticle," Phys. Rev. B **69**(9), 094,305 (2004).

[52] M. Perner, P. Bost, U. Lemmer, G. von Plessen, J. Feldmann, U. Becker, M. Mennig, M. Schmitt, and H. Schmidt, "Optically induced damping of the surface plasmon resonance in gold colloids," Phys. Rev. Lett. **78**(11), 2192–2195 (1997).

[53] M. R. Beversluis, A. Bouhelier, and L. Novotny, "Continuum generation from single gold nanostructures through near-field mediated intraband transitions," Phys. Rev. B **68**(11), 115,433 (2003).

[54] C. D. Geddes, A. Parfenov, and J. R. Lakowicz, "Luminescent blinking from noble-metal nanostructures: New probes for localizationand imaging," J. Fluoresc. **13**(4), 297–299 (2003).

[55] L. A. Peyser, A. E. Vinson, A. P. Bartko, and R. M. Dickson, "Photoactivated fluorescence from individual silver nanoclusters," Science **291**(5501), 103–106 (2001).

[56] M. Pelton, M. Z. Liu, S. Park, N. F. Scherer, and P. Guyot-Sionnest, "Ultrafast resonant optical scattering from single gold nanorods: Large nonlinearities and plasmon saturation," Phys. Rev. B **73**(15), 155,419 (2006).

[57] M. Lippitz, M. A. van Dijk, and M. Orrit, "Third-harmonic generation from single gold nanoparticles," Nano Lett. **5**(4), 799–802 (2005).

[58] C. Sönnichsen, S. Geier, N. E. Hecker, G. von Plessen, J. Feldmann, H. Ditlbacher, B. Lamprecht, J. R. Krenn, F. R. Aussenegg, V. Z. H. Chan, J. P. Spatz, and M. Moller, "Spectroscopy of single metallic nanoparticles using total internal reflectionmicroscopy," Appl. Phys. Lett. **77**(19), 2949–2951 (2000).

[59] S. Schultz, D. R. Smith, J. J. Mock, and D. A. Schultz, "Single-target molecule detection with nonbleaching multicolor optical immunolabels," Proc. Natl. Acad. Sci. U. S. A. **97**(3), 996–1001 (2000).

[60] S. Berciaud, L. Cognet, P. Tamarat, and B. Lounis, "Observation of intrinsic size effects in the optical response of individual gold nanoparticles," Nano Lett. **5**(3), 515–518 (2005).

[61] O. L. Muskens, N. Del Fatti, and F. Vallée, "Femtosecond response of a single metal nanoparticle," Nano Lett. **6**(3), 552–556 (2006).

[62] M. A. van Dijk, M. Lippitz, and M. Orrit, "Detection of acoustic oscillations of single gold nanospheres by time-resolved interferometry," Phys. Rev. Lett. **95**(26), 267,406 (2005).

[63] J. Gelles, B. J. Schnapp, and M. P. Sheetz, "Tracking Kinesin-Driven Movements With Nanometre-Scale Precision," Nature **331**(6155), 450–453 (1988).

[64] A. Arbouet, D. Christofilos, N. Del Fatti, F. Vallée, J. R. Huntzinger, L. Arnaud, P. Billaud, and M. Broyer, "Direct measurement of the single-metal-cluster optical absorption," Phys. Rev. Lett. **93**(12), 127,401 (2004).

[65] T. Plakhotnik and V. Palm, "Interferometric signatures of single molecules," Phys. Rev. Lett. **8718**(18), 183,602 (2001).

[66] K. Lindfors, T. Kalkbrenner, P. Stoller, and V. Sandoghdar, "Detection and spectroscopy of gold nanoparticles using supercontinuum white light confocal microscopy," Phys. Rev. Lett. **93**(3), 037,401 (2004).

[67] S. Berciaud, D. Lasne, G. A. Blab, L. Cognet, and B. Lounis, "Photothermal heterodyne imaging of individual metallic nanoparticles: Theory versus experiment," Phys. Rev. B **73**(4), 045,424 (2006).

[68] D. Boyer, P. Tamarat, A. Maali, B. Lounis, and M. Orrit, "Photothermal imaging of nanometer-sized metal particles among scatterers," Science **297**(5584), 1160–1163 (2002).

[69] F. V. Ignatovich and L. Novotny, "Real-time and background-free detection of nanoscale particles," Phys. Rev. Lett. **96**(1), 013,901 (2006).

[70] M. A. van Dijk, M. Lippitz, D. Stolwijk, and M. Orrit, "A common-path interferometer for time-resolved and shot-noise-limited detection of single nanoparticles," Opt. Express **15**(5), 2273–2287 (2007).

[71] S. Berciaud, L. Cognet, G. A. Blab, and B. Lounis, "Photothermal heterodyne imaging of individual nonfluorescent nanoclusters and nanocrystals," Phys. Rev. Lett. **93**(25), 257,402 (2004).

[72] H. C. van de Hulst, "On The Attenuation Of Plane Waves By Obstacles Of Arbitrary Size And Form," Physica **15**(8-9), 740–746 (1949).

[73] M. Born and E. Wolf, *Principles of Optics 6th ed.* (Pergamon Press, Oxford, England, 1986).

[74] M. Bruchez, M. Moronne, P. Gin, S. Weiss, and A. P. Alivisatos, "Semiconductor nanocrystals as fluorescent biological labels," Science **281**(5385), 2013–2016 (1998).

[75] S. Link and M. A. El-Sayed, "Spectral properties and relaxation dynamics of surface plasmon electronic oscillations in gold and silver nanodots and nanorods," J. Phys. Chem. B **103**(40), 8410–8426 (1999).

[76] A. Arbouet, C. Voisin, D. Christofilos, P. Langot, N. Del Fatti, F. Vallée, J. Lerme, G. Celep, E. Cottancin, M. Gaudry, M. Pellarin, M. Broyer, M. Maillard, M. P. Pileni, and M. Treguer, "Electron-phonon scattering in metal clusters," Phys. Rev. Lett. **90**(17), 177,401 (2003).

[77] C. Sönnichsen, T. Franzl, T. Wilk, G. von Plessen, J. Feldmann, O. Wilson, and P. Mulvaney, "Drastic reduction of plasmon damping in gold nanorods," Phys. Rev. Lett. **88**(7), 077,402 (2002).

[78] L. Canioni, S. Rivet, L. Sarger, R. Barille, P. Vacher, and P. Voisin, "Imaging of Ca 2+ intracellular dynamics with a third-harmonic generation microscope," Opt. Lett. **26**(8), 515–517 (2001).

[79] S. V. Fomichev, S. V. Popruzhenko, D. F. Zaretsky, and W. Becker, "Laser-induced nonlinear excitation of collective electron motion in a cluster," J. Phys. B **36**, 3817–3834 (2003).

[80] J. M. Schins, T. Schrama, J. Squier, G. J. Brakenhoff, and M. Müller, "Determination of material properties by use of third-harmonic generation microscopy," J. Opt. Soc. Am. B **19**(7), 1627–1634 (2002).

[81] J. Y. Courtois, J. M. Courty, and J. C. Mertz, "Internal dynamics of multilevel atoms near a vacuum-dielectric interface," Phys. Rev. A **53**(3), 1862–1878 (1996).

[82] S. V. Fomichev, S. V. Popruzhenko, D. F. Zaretsky, and W. Becker, "Nonlinear excitation of the Mie resonance in a laser-irradiated cluster," Optics Express **11**(19), 2433–2439 (2003).

[83] D. Carroll and X. H. Zheng, "Spatial and angular distributions of third harmonic generation from metal surfaces," Eur. Phys. J. D **5**(1), 135–144 (1999).

[84] D. Lasne, G. A. Blab, S. Berciaud, M. Heine, L. Groc, D. Choquet, L. Cognet, and B. Lounis, "Single nanoparticle photothermal tracking (SNaPT) of 5-nm gold beads in live cells," Biophys. J. **91**(12), 4598–4604 (2006).

[85] L. Cognet, C. Tardin, D. Boyer, D. Choquet, P. Tamarat, and B. Lounis, "Single metallic nanoparticle imaging for protein detection in cells," Proc. Natl. Acad. Sci. U. S. A. **100**(20), 11,350–11,355 (2003).

[86] R. C. Jin, J. E. Jureller, H. Y. Kim, and N. F. Scherer, "Correlating second harmonic optical responses of single Ag nanoparticles with morphology," J. Am. Chem. Soc. **127**(36), 12,482–12,483 (2005).

[87] M. A. van Dijk, M. Lippitz, and M. Orrit, "Far-field optical microscopy of single metal nanoparticles," Accounts Chem. Res. **38**(7), 594–601 (2005).

[88] P. Stoller, V. Jacobsen, and V. Sandoghdar, "Measurement of the complex dielectric constant of a single gold nanoparticle," Opt. Lett. **31**(16), 2474–2476 (2006).

[89] M. A. van Dijk, A. L. Tchebotareva, M. Orrit, M. Lippitz, S. Berciaud, D. Lasne, L. Cognet, and B. Lounis, "Absorption and scattering microscopy of single metal nanoparticles," Phys. Chem. Chem. Phys. **8**, 3486 – 3495 (2006).

[90] F. Zernike, "Phase contrast, a new method for the microscopic observation of transparent objects," Physica **9**, Part I, 686–698, Part II, 974–986 (1942).

[91] J. Hwang, M. M. Fejer, and W. E. Moerner, "Scanning interferometric microscopy for the detection of ultrasmall phase shifts in condensed matter," Phys. Rev. A **73**(2), 021,802 (2006).

[92] M. J. LaGasse, D. Liu-Wong, J. G. Fujimoto, and H. A. Haus, "Ultrafast switching with a single-fiber interferometer," Opt. Lett. **14**(6), 311–313 (1989).

[93] N. S. Patel, K. L. Hall, and K. A. Rauschenbach, "Interferometric all-optical switches for ultrafast signal processing," Appl. Opt. **37**(14), 2831–2842 (1998).

[94] D. H. Hurley and O. B. Wright, "Detection of ultrafast phenomena by use of a modified Sagnac interferometer," Opt. Lett. **24**(18), 1305–1307 (1999).

[95] Y. Sugawara, O. B. Wright, O. Matsuda, M. Takigahira, Y. Tanaka, S. Tamura, and V. E. Gusev, "Watching ripples on crystals," Phys. Rev. Lett. **88**(18), 185,504 (2002).

[96] T. Tachizaki, T. Muroya, O. Matsuda, Y. Sugawara, D. H. Hurley, and O. B. Wright, "Scanning ultrafast Sagnac interferometry for imaging

two-dimensional surface wave propagation," Rev. Sci. Instrum. **77**(4), 043,713 (2006).

[97] F. L. Pedrotti and L. S. Pedrotti, *Introduction to Optics* (Prentice Hall, 1993).

[98] H.-A. Bachor, *A Guide to Experiments in Quantum Optics* (Wiley-VCH, 1998).

[99] R. J. McIntyre, "Multiplication Noise In Uniform Avalanche Diodes," IEEE Trans. Electron Devices **ED13**(1), 164–168 (1966).

[100] G. P. Wiederrecht, "Near-field optical imaging of noble metal nanoparticles," Eur. Phys. J.-Appl. Phys. **28**(1), 3–18 (2004).

[101] E. M. H. P. van Dijk, J. Hernando, J. J. Garcia-Lopez, M. Crego-Calama, D. N. Reinhoudt, L. Kuipers, M. F. Garcia-Parajo, and N. F. van Hulst, "Single-molecule pump-probe detection resolves ultrafast pathways in individual and coupled quantum systems," Phys. Rev. Lett. **94**(7), 078,302 (2005).

[102] T. Guenther, C. Lienau, T. Elsaesser, M. Glanemann, V. M. Axt, T. Kuhn, S. Eshlaghi, and A. D. Wieck, "Coherent nonlinear optical response of single quantum dots studied by ultrafast near-field spectroscopy," Phys. Rev. Lett. **89**(5), 057,401 (2002).

[103] C. Voisin, D. Christofilos, P. A. Loukakos, N. Del Fatti, F. Vallée, J. Lerme, M. Gaudry, E. Cottancin, M. Pellarin, and M. Broyer, "Ultrafast electron-electron scattering and energy exchanges in noble-metal nanoparticles," Phys. Rev. B **69**(19), 195,416 (2004).

[104] N. Del Fatti, C. Voisin, D. Christofilos, F. Vallée, and C. Flytzanis, "Acoustic vibration of metal films and nanoparticles," J. Phys. Chem. A **104**(18), 4321–4326 (2000).

[105] A. Nelet, A. Crut, A. Arbouet, N. Del Fatti, F. Vallée, H. Portales, L. Saviot, and E. Duval, "Acoustic vibrations of metal nanoparticles: high order radial mode detection," Appl. Surf. Sci. **226**(1-3), 209–215 (2004).

[106] O. L. Muskens, N. Del Fatti, F. Vallée, P. Huntzinger, J. R.and Billaud, and M. Broyer, "Single metal nanoparticle absorption spectroscopy and optical characterization," Appl. Phys. Lett. **88**(6), 063,109 (2006).

[107] K. S. Lee and M. A. El-Sayed, "Dependence of the enhanced optical scattering efficiency relative to that of absorption for gold metal nanorods on aspect ratio, size, end-cap shape, and medium refractive index," J. Phys. Chem. B **109**(43), 20,331–20,338 (2005).

[108] B. T. Draine and P. J. Flatau, "Discrete-Dipole Approximation For Scattering Calculations," J. Opt. Soc. Am. A-Opt. Image Sci. Vis. **11**(4), 1491–1499 (1994).

[109] L. M. LizMarzan, M. Giersig, and P. Mulvaney, "Synthesis of nanosized gold-silica core-shell particles," Langmuir **12**(18), 4329–4335 (1996).

[110] J. E. Sader, G. V. Hartland, and P. Mulvaney, "Theory of acoustic breathing modes of core-shell nanoparticles," J. Phys. Chem. B **106**(6), 1399–1402 (2002).

[111] M. Danckwerts and L. Novotny, "Optical frequency mixing at coupled gold nanoparticles," Phys. Rev. Lett. **98**(2), 026,104 (2007).

Samenvatting

Een studie van individuele gouden nanodeeltjes met

niet-lineaire optische technieken

Heel globaal gaat mijn proefschrift over de interactie tussen lichtpulsen en gouden nanodeeltjes. Gouden nanodeeltjes zijn kleine bolvormige clusters van goudatomen, met een diameter van ongeveer 1 tot 100 nanometer (een nanometer is een miljoenste van een millimeter). Het belangrijkste doel van mijn onderzoek was het ontwikkelen van nieuwe technieken om deze kleine bolletjes te detecteren, en wel zo dat de bolletjes *afzonderlijk* kunnen worden gedetecteerd. Vanzelfsprekend levert de eis om slechts één bolletje tegelijk te meten flink wat experimentele moeilijkheden op, want welke methode we ook kiezen voor de detectie van de deeltjes, het signaal van een enkel goud-deeltje zal altijd zwak zijn.

Toepassingen van gouden nanodeeltjes

Gouden nanodeeltjes hebben toepassingen in ver uiteenlopende gebieden. Eén van de belangrijkste en meest gebruikte toepassingen voor gouden na-nodeeltjes is als label in biologische experimenten. Als een bioloog wil weten hoe een bepaald eiwit zich door een cel voortbeweegt, dan heeft hij een la-bel nodig dat dit eiwit zichtbaar kan maken. Eiwitten zijn te klein om direct waar te nemen, zelfs met de sterkste microscoop, dus er dient iets aan het eiwit vastgemaakt te worden dat genoeg contrast geeft om het eiwit te kun-nen detecteren. Een mogelijk label is een gouden nanodeeltje en het grote voordeel van deze deeltjes is dat ze zeer inert zijn. Doordat het metaal vrij-wel niet met de omgeving reageert, is de levensduur van het label vrijwel

ongelimiteerd, dit in tegenstelling tot vele andere labels die vaak na enkele seconden tot enkele minuten geen signaal meer afgeven. Wel is het zo, dat als het gouddeeltje te groot is, het teveel invloed heeft op de beweging van het eiwit waaraan het is vastgemaakt. Het is dus van belang om detectiemethoden te ontwikkelen die gevoelig genoeg zijn voor detectie van zo klein mogelijke gouddeeltjes, het liefst deeltjes met een diameter kleiner dan 5 nanometer.

Een ander toepassingsgebied is optische dataopslag. Met behulp van laserlicht kunnen gouden nanostaafjes van vorm veranderd worden. Door deze vormverandering reageren ze anders op licht en deze eigenschap kan gebruikt worden om data te coderen. Een voordeel van deze staafjes is, dat de kans dat ze spontaan van vorm veranderen nihil is, waardoor de levensduur en de betrouwbaarheid van deze datadragers in potentie zeer groot is. Staafjes zijn, afhankelijk van hun vorm, slechts gevoelig voor specifieke kleuren licht. Door staafjes van verschillende afmetingen met meerdere lichtbronnen te coderen en uit te lezen, kan de dichtheid van de data op de dragers verhoogd worden.

Een toepassing die in de toekomst mogelijk zou kunnen worden door mijn onderzoek is het gebruik van gouden nanodeeltjes om eigenschappen van een stof te kunnen meten met een zeer hoge ruimtelijke resolutie. Bepaalde optische en mechanische eigenschappen van gouddeeltjes zijn zeer gevoelig voor veranderingen van bijvoorbeeld de dichtheid of de elasticiteit van een materiaal waarin ze opgelost zijn. Door deze eigenschappen te meten voor individuele deeltjes op verschillende locaties in het materiaal, kan een structuur van dichtheid of elasticiteit van een materiaal met hoge ruimtelijke preciesie bepaald worden.

Naast alle toepassingen zijn gouden nanodeeltjes op zichzelf zeer interessante studie-objecten vanuit een fundamenteel natuurkundig oogpunt. Omdat gouden nanodeeltjes zich qua afmeting bevinden op het grensgebied tussen de klassieke natuurkunde en de kwantummechanica, die het gedrag van moleculen en atomen beschrijft, zijn wetenschappers al meerdere decennia geïnteresseerd in de optische en mechanische eigenschappen van deze deeltjes.

Individuele deeltjes

Het is belangrijk om een onderscheid te maken tussen bulk-detectie, het doen van metingen aan veel gouddeeltjes tegelijk, en de studie van individuele gouddeeltjes, waarbij slechts één deeltje tegelijk wordt bestudeerd. Hoewel bulk-detectie experimenteel veel eenvoudiger is (de signalen zijn vanzelfsprekend stukken sterker) en dit soort metingen de afgelopen decennia veel

interessante resultaten hebben opgeleverd, biedt de studie van individuele gouddeeltjes een aantal voordelen. Vergelijk het met een orkest. Als alle muzikanten in een orkest netjes in de maat spelen en hun instrumenten goed zijn gestemd, is er niets aan de hand en produceert het orkest prachtige muziek. Als echter één of meer muzikanten vals of uit de maat spelen, loont het de moeite om alle muzikanten apart te nemen om uit te vinden bij wie het fout gaat. Zo is het ook bij een verzameling van gouddeeltjes. Zolang alle fysische processen zich bij alle deeltjes op dezelfde manier en tegelijkertijd manifesteren zijn deze processen in een bulk experiment te meten. Echter, om verschillen tussen de deeltjes te bepalen, of om processen te meten die niet bij alle deeltjes tegelijk plaatsvinden, is het nodig om de deeltjes één voor één te bestuderen. Een voorbeeld hiervan zijn gouddeeltjes die aan eiwitten gelabeld allemaal door elkaar door een cel bewegen. In bulk detectie wordt vrijwel geen beweging gemeten, omdat er vrijwel evenveel gouddeeltjes naar links als naar rechts bewegen, maar door de gouddeeltjes afzonderlijk te bestuderen kan de beweging van de verschillende eiwitten in kaart worden gebracht.

Licht, laserpulsen en detectie van gouden nanodeeltjes

Voor een goed begrip van mijn onderzoek is eerst wat basiskennis noodzakelijk, voornamelijk over het golfkarakter van licht. Licht is een vorm van energie die zich voortplant als een trillend elektromagnetisch veld, met een snelheid van 300.000 kilometer per seconde, de lichtsnelheid. Het karakter van het licht kan worden beschreven met de golflengte, die wordt uitgedrukt in nanometers (afkorting nm, 1 miljardste van een meter). Zichtbaar licht beslaat slechts een klein deel van het totale elektromagnetische spectrum met golflengten ongeveer tussen 400 nm en 650 nm. De kleur van het licht zoals wij dat waarnemen is afhankelijk van de golflengte. Zo is licht met een golflengte van 450 nm blauw, licht met een golflengte van 530 nm groen en licht met een golflengte van 650 nm rood.

Als lichtbron wordt in hedendaagse optische experimenten meestal een laser gebruikt. In mijn experimenten maakte ik gebruik van een speciale klasse lasers: pulserende lasers. Terwijl normale lasers een continu vermogen uitzenden, wordt het licht van een pulserende laser in korte pulsen uitgezonden. De pulsduur is in de orde van een picoseconde, ofwel een miljardste van een milliseconde.

Het samenpersen van het licht in deze korte pulsen heeft twee voordelen. Ten eerste kan het lichtvermogen zeer hoge waarden aannemen, omdat al het licht vrijwel tegelijk bij het te bestuderen systeem aankomt. Hierdoor kunnen processen worden waargenomen die onder normale omstandigheden veel te

zwak zijn. Een tweede voordeel van het gebruik van korte lichtpulsen is dat processen bestudeerd kunnen worden op tijdschalen die overeenkomen met de lengte van de puls. Deze tijdschaal is veel te kort om conventionele detectiemethoden te kunnen gebruiken, de elektronica is simpelweg te langzaam.

Om de dynamica van een systeem op ultrakorte tijdschalen te bestuderen wordt een techniek gebruikt die pomp-sonde spectroscopie wordt genoemd. Dit is het beste uit te leggen met een voorbeeld. Een systeem waar metingen aan gedaan worden, dit noemen we een sample, wordt belicht met een korte lichtpuls, waardoor het opwarmt en even later weer afkoelt. De vraag is nu hoe snel het systeem precies afkoelt. De optische eigenschappen van het sample zijn in dit geval afhankelijk van de temperatuur, waardoor het mogelijk is om die temperatuur met behulp van licht te meten. Het experiment gaat nu als volgt. Eerst wordt het sample met een korte lichtpuls, de pomppuls, opgewarmd. Vervolgens blijft het korte tijd donker, waarna een sondepuls de temperatuur van het sample meet. Door het interval tussen de pomppuls en de sondepuls te variëren in een serie metingen, kan het gehele tijdsverloop worden bepaald. De truc zit in het variëren van het interval tussen de pomppuls en de sondepuls. Dit kan heel nauwkeurig geregeld worden door de afstand die beide pulsen afleggen vanaf de laser tot aan het sample te variëren, bijvoorbeeld door een spiegel te verplaatsen. Voor een interval van 1 picoseconde dient deze spiegel 0,15 mm verplaatst te worden, wat met huidige technieken eenvoudig en zeer nauwkeurig voor elkaar te krijgen is.

De meest gangbare processen die voor het detecteren van gouden nanodeeltjes worden gebruikt, zijn *absorptie* en *verstrooiing*. Absorptie van licht is de opname van lichtenergie door een materiaal, waarna het wordt omgezet in een andere energievorm, zoals warmte. In het geval van verstrooiing wordt het licht van richting veranderd door het deeltje waarmee het interactie heeft. Beide processen leiden er toe dat de intensiteit van een lichtbundel in de voorwaartse richting wordt verminderd en dat is dan ook dé manier om absorptie en verstrooiing te meten. Het moge duidelijk zijn dat bij absorptie en verstrooiing door een enkel gouddeeltje de lichtintensiteit maar heel weinig verandert. Een enkel gouddeeltje absorbeert slechts 0.01% van een goed gefocusseerde lichtbundel. Dit is zo weinig dat dit signaal normaal gesproken volledig wordt overvleugeld door de ruis die onvermijdelijk aanwezig is in iedere lichtbundel. Het is daarom noodzakelijk om speciale technieken te ontwikkelen om dit probleem te kunnen omzeilen.

Een onmisbaar hulpmiddel bij de studie van individuele gouddeeltjes is een microscoop. In een microscoop worden de lichtstralen zeer sterk gefocusseerd, waardoor het mogelijk is al het licht in een laserbundel op een zeer

klein oppervlak samen te brengen. Dit focusseren is echter niet ongelimiteerd. Het is fysisch niet mogelijk om de diameter van het brandpunt kleiner te maken dan (ongeveer) de golflengte van het gebruikte licht. Met een microscoop is het dus mogelijk al het licht samen te brengen op een oppervlak waarvan de diameter in de orde van het tienvoudige van de diameter van een gouddeeltje is. Op deze manier wordt er relatief meer licht door een gouddeeltje verstrooid dan wanneer het gouddeeltje met een ongefocusseerde lichtbundel zou worden belicht. De gouddeeltjes worden op een glasplaatje in de microscoop geplaatst. Een glasplaatje met gouddeeltjes noemen we een *sample*. Het sample kan in de microscoop bewogen worden en zo wordt het oppervlak van het glasplaatje gescand op de aanwezigheid van gouddeeltjes. Doordat de concentratie van de gouddeeltjes op het glasplaatje erg laag is, is het mogelijk om slechts één deeltje tegelijk in het brandpunt van de laser te observeren. Op de achterkant van dit proefschrift staat een foto van onze microscoop. Te zien zijn twee microscoop-objectieven, één om de laserbundel te focusseren en één om de bundel na interactie met het sample weer evenwijdig te maken. Tussen de twee objectieven is een glasplaatje te zien waarop de gouddeeltjes zich bevinden.

Om de gouddeeltjes op het sample te kunnen detecteren, moeten ze onderscheiden worden van de achtergrond. Dit kan bijvoorbeeld door gebruik te maken van hun absorptie-eigenschappen. Een gouddeeltje absorbeert meer licht dan het glasplaatje, dus als een gouddeeltje in het brandpunt van de laser wordt geplaatst, valt er minder licht op de voor de detectie gebruikte lichtmeter, mits de ruis voldoende kan worden onderdrukt om het signaal te kunnen meten. Een andere detectiemethode is om in een gouddeeltje licht van andere kleuren dan die van de lichtbron te genereren. In dat geval is het door een gebruik van een kleurenfilter voor de detector vrij eenvoudig om het signaal van de gouddeeltjes van de achtergrond te onderscheiden.

Mijn onderzoek

In de eerste maanden van mijn promotieonderzoek heb ik me bezig gehouden met een techniek die gebaseerd is op de generatie van nieuwe golflengten en gebruik maakt van de hoge vermogens van laserpulsen. We gebruikten een niet-lineair verstrooiingsproces, derde harmonische generatie. Verstrooiing van licht, zoals eerder in deze samenvatting is uitgelegd, is simpel gesteld de verandering van richting van licht door een gouddeeltje. Wat er eigenlijk gebeurt, is dat de energie van het licht heel kort wordt omgezet in een trilling in het gouddeeltje. Door deze trilling zendt het gouddeeltje vrijwel meteen weer licht uit, met dezelfde golflengte als dat van de bron, maar in een andere

richting. Dit is lineaire verstrooiing. Een heel klein deel van het licht wordt echter niet met dezelfde golflengte uitgezonden, maar met de heldt of een derde van de golflengte van de bron en dit is niet-lineaire verstrooiing. Als we dus licht met een golflengte van 1500 nm aan een gouddeeltje verstrooien, wordt ook licht met golflengten van 750 nm (dit heet tweede harmonische generatie) en 500 nm (derde harmonische generatie) verstrooid. Deze signalen zijn zeer zwak, maar worden versterkt door het hoge piekvermogen van een laserpuls. Bij lineaire verstrooiing is het zo, dat als de intensiteit van de lichtbron verdubbeld wordt, de intensiteit van het verstrooide licht ook verdubbelt. Bij tweede harmonische generatie neemt als de intensiteit van de bron wordt verdubbeld het verstrooide licht met een factor vier toe en bij derde harmonische generatie zelfs met een factor acht. Dit is een niet-lineaire versterking van het signaal. Om deze reden is het dus belangrijk om, bijvoorbeeld door gebruik te maken van laserpulsen, hele hoge piekvermogens te kunnen bereiken. Voor een klein bolvormig object zoals een gouden nanodeeltje is tweede harmonische generatie fysisch onmogelijk. Doordat in de praktijk gouddeeltjes geen ideale bollen zijn, maar altijd wat onvolkomenheden hebben, wordt tweede harmonische generatie toch gedetecteerd, zij het dat het signaal erg onvoorspelbaar is. Om deze reden probeerden wij de deeltjes te detecteren via derde-harmonische generatie. Met een lichtbron met een golflengte van 1500 nm observeerden wij licht dat verstrooid werd door individuele deeltjes bij een golflengte van 500 nm (dus de derde harmonische). Dit experiment wordt in hoofdstuk 2 beschreven. De onderste grafiek op de kaft van dit proefschrift geeft een golflengte-afhankelijke detectie van tweede en derde harmonische generatie aan een individueel gouddeeltje. Te zien zijn twee pieken, de linker heeft een golflengte van 500 nm en de rechter een golflengte van 750 nm (de assen zijn hier uiteraard om louter estetische redenen verwijderd). Hoewel de techniek uiteindelijk succesvol was voor het detecteren van individuele gouddeeltjes, lukte het niet om deeltjes te detecteren die klein genoeg zijn om gebruikt te worden voor biologische toepassingen. Om deze reden hebben we dit experiment niet voortgezet en zijn we begonnen aan de ontwikkeling van een andere methode.

Het tweede experiment was gebaseerd op absorptie van licht door een gouden nanodeeltje en gebruikte de mogelijkheid van laserpulsen om de eigenschappen van gouddeeltjes op hele korte tijdschaal te meten, met behulp van de eerder beschreven pomp-sonde techniek. Om ruis te minimaliseren wordt in ons experiment de sondepuls in tweeën gesplitst in een optisch kristal, waarbij de tweede puls een fractie vertraagd wordt maar wel hetzelfde pad blijft volgen. Na interactie met een gouddeeltje in de microscoop worden

de twee pulsen weer samengevoegd. Je meet dan het verschil in de absorptie eigenschappen van het deeltje in de tijdsspanne tussen de twee pulsen. Doordat één en dezelfde puls gesplitst wordt en weer wordt samengevoegd, wordt ruis in de vorm van intensiteitsfluctuaties tussen de verschillende pulsen onderdrukt. Om een verschil in absorptie eigenschappen te meten moet er natuurlijk wel een verschil *zijn*, maar hier zorgt de pomppuls voor. Door een pomppuls uit een tweede laser in de tijd tussen de twee pulsen uit de interferometer bij het sample te laten komen, wordt het gouddeeltje opgewarmd. De absorptie eigenschappen zijn temperatuursafhankelijk, dus door het deeltje op te warmen wordt er een verschil in absorptie geïnduceerd, dat met de twee sondepulsen gemeten kan worden. De details van deze nieuwe meetmethode komen in hoofdstuk 3 aan de orde.

Helaas lukte het ook met deze methode niet om deeltjes die klein genoeg zijn voor biologische experimenten te meten. Daarnaast werd op ongeveer hetzelfde moment in Frankrijk een techniek ontwikkeld waarmee dit wel mogelijk is. Echter, onze methode stelde ons wel in staat om de eigenschappen van individuele deeltjes op zeer korte tijdschalen te meten, iets dat tot voor kort alleen voor grote aantallen deeltjes tegelijk gedaan kon worden. Hiermee komen we aan het laatste aspect van mijn onderzoek: het bestuderen van de optische en mechanische eigenschappen van individuele gouden nanodeeltjes. Ik heb me voornamelijk geconcentreerd op akoestische vibraties van gouddeeltjes.

Als een gouddeeltje wordt belicht met een korte laserpuls, wordt het deeltje zodanig uit evenwicht gebracht dat een trilling in het atoomrooster wordt gelanceerd, waarbij het deeltje periodiek uitzet. Deze trilling is vergelijkbaar met een klepel die tegen een bel aanslaat. De korte klap lanceert een trilling in de bel met een bepaalde frequentie en dempingstijd die karakteristiek zijn voor het materiaal, de vorm en de grootte van de bel, alsmede voor de omgeving (een bel klinkt onder water anders dan boven water). De bel zal ook boventonen laten klinken, wat het karakterisieke geluid geeft. Ook een gouddeeltje trilt met zijn eigen karakteristieke frequentie en dempingstijd, die onder andere afhangen van de grootte van het deeltje, van de geluidssnelheid van het materiaal én van de geluidssnelheid en de dichtheid van de omgeving. En net als een bel kan ook een gouddeeltje op meerdere frequenties trillen. Eén van die frequenties, die bij sommige deeltjes zeer sterk naar voren kwam, kon gerelateerd worden aan een elliptische vervorming van het deeltje. Voor lange tijd was het onduidelijk hoe het kwam dat we deze vervorming maar bij een klein aantal deeltjes zagen, maar dan wel zeer sterk. Met experimenten waarin het trillingsgedrag direct gecorreleerd werd aan

het absorptiespectrum (het absorptiespectrum geeft voor iedere kleur weer hoe sterk deze geabsorbeerd wordt), konden we uiteindelijk laten zien dat deze vervorming gedetecteerd werd bij deeltjesparen, oftewel twee deeltjes die tegen elkaar aanliggen. In hoofdstuk 4 worden de eerste experimenten met akoestische trillingen beschreven. Een voorbeeld van een meting van een akoestische trilling is te zien in Figuur 4.2 en in de bovenste grafiek op de kaft van dit proefschrift. De gedempte oscillatie die te zien is in deze plaatjes wordt veroorzaakt door de periodieke uitzetting van het atoomrooster. Hoofdstuk 5 tenslotte, is een verslag van enkele meer gedetailleerde metingen aan akoestische vibraties. Gepoogd werd om de eigenschappen die in de optische experimenten worden gemeten direct te relateren aan de structuur en de omgeving van de individuele deeltjes. Dit is een ambitieus project en nog lang niet af, maar gelukkig wordt het onderzoek na mijn promotie door anderen voortgezet.

Nawoord

Het is een groot misverstand dat een promovendus vier jaar lang in een donker kamertje eenzaam op een onderzoek zit te zwoegen. Niemand schrijft een proefschrift alleen en ik was daarin zeker geen uitzondering.

De afgelopen vier jaar heb ik met veel plezier in de MoNOS groep gewerkt. De lange gesprekken en discussies tijdens koffie- en lunchpauzes waren vaak een welkome afwisseling op het werk in het laboratorium. Florian, Alexander, Rob, Rogier, Clemens, Aureliën, en alle anderen, bedankt hiervoor. Ook de werksfeer in de groep is absoluut bijzonder te noemen. Ik heb het erg gewaardeerd dat het altijd mogelijk was even binnen te lopen voor een discussie of overleg, dat vervolgens vaak de hele middag kon duren. Florian Kulzer verdient hierin een speciale vermelding, voor zijn onuitputtelijke kennis van optica en zijn niet aflatende bereidheid om altijd even te komen helpen als dat nodig is.

De technische, elektronische en IT ondersteuning was altijd van een zeer hoog niveau, waarvoor ik Jos Disselhorst, Harmen van der Meer, René Overgauw en Arno van Amersfoort dankbaar ben. Vertragingen van technische aard waren tijdens mijn promotie vrijwel afwezig, mede dankzij jullie snelle en kundige hulp.

Daniël Stolwijk en Paul Ruijgrok hebben als studenten een bijdrage geleverd aan hoofdstukken 3 en 5 van dit proefschrift. Ik ben jullie beide zeer erkentelijk voor de inzet tijdens jullie stages en de prettige samenwerking. Ook Anna Tchebotareva ben ik dank verschuldigd voor haar wetenschappelijke bijdragen en de vele nuttige discussies.

James Chon and Peter Zijlstra cooperated on the experiments with silica-coated gold nanoparticles, presented in chapter 5, and James visited Leiden last december for some experiments on gold nanorods. Peter, bedankt voor de snelle en secure coating van mijn gouddeeltjes. Deze experimenten waren een waardevolle toevoeging aan mijn laatste hoofdstuk. James, too bad the rods experments didn't work out yet, but I'm sure something nice will come

out in the near future.

Als laatste bedank ik hier mijn vrienden en familie, met name Leo, Ria en Sanne, voor al hun steun en interesse in de afgelopen jaren. Nathalie, dank je voor je eindeloze liefde en niet in de laatste plaats voor het aanhoren en bekritiseren van al die oefenpresentaties.

List of Publications

- E. J. G. Peterman, M. A. van Dijk, L. C. Kapitein, and C. F. Schmidt, "Extending the bandwidth of optical-tweezers interferometry," Rev. Sci. Instrum. **74**(7), 3246–3249 (2003).

- M. A. van Dijk, L. C. Kapitein, J. van Mameren, C. F. Schmidt, and E. J. G. Peterman, "Combining optical trapping and single-molecule fluorescence spectroscopy: Enhanced photobleaching of fluorophores," J. Phys. Chem. B **108**(20), 6479–6484 (2004).

- M. Lippitz, M. A. van Dijk, and M. Orrit, "Third-harmonic generation from single gold nanoparticles," Nano Lett. **5**(4), 799–802 (2005).

- M. A. van Dijk, M. Lippitz, and M. Orrit, "Far-field optical microscopy of single metal nanoparticles," Accounts Chem. Res. **38**(7), 594–601 (2005).

- M. A. van Dijk, M. Lippitz, and M. Orrit, "Detection of acoustic oscillations of single gold nanospheres by time-resolved interferometry," Phys. Rev. Lett. **95**(26), 267,406 (2005).

- M. A. van Dijk, A. L. Tchebotareva, M. Orrit, M. Lippitz, S. Berciaud, D. Lasne, L. Cognet, and B. Lounis, "Absorption and scattering microscopy of single metal nanoparticles," Phys. Chem. Chem. Phys. **8**, 3486 – 3495 (2006).

- M. A. van Dijk, M. Lippitz, D. Stolwijk, and M. Orrit, "A common-path interferometer for time-resolved and shot-noise-limited detection of single nanoparticles," Opt. Express **15**(5), 2273–2287 (2007).

- M. A. van Dijk, P. V. Ruijgrok, A. L. Tchebotareva, P. Zijlstra, J. W. M. Chon, M. Gu, M. Lippitz, and M. Orrit, "Correlation of optical and structural properties of single gold nanoparticles," manuscript in preparation.

- A. L. Tchebotareva, M. A. van Dijk, P. V. Ruijgrok, , M. B. S. Hesselberth, M. Lippitz, and M. Orrit, "Correlating optical response to electron microscopy and vibration spectroscopy of a gold nanoparticle," manuscript in preparation.

Curriculum Vitae

van Meindert van Dijk, geboren te Zaanstad op 26 april 1979.

In 1997 behaalde ik mijn VWO diploma aan het Zaanlands Lyceum in Zaandam, waarna ik Natuurkunde ging studeren aan de Vrije Universiteit in Amsterdam. Mijn afstudeerstage was in de groep Fysica van Complexe Systemen waar ik onder begeleiding van dr. Erwin Peterman onderzoek heb gedaan naar bleking van fuorescerende moleculen in een optisch pincet. In augustus 2003 ben ik afgestudeerd.

In september 2003 ben ik begonnen aan een promotieonderzoek aan de Universiteit Leiden, in de MoNOS groep (Molecular Nano-Optics and Spins). Onder begeleiding van prof. dr. Michel Orrit en dr. Markus Lippitz werkte ik daar aan de ontwikkeling van nieuwe technieken voor detectie van individuele gouden nanodeeltjes en heb ik deze technieken toegepast voor studie van de fysische eigenschappen van deze deeltjes. We zijn in staat geweest om individuele gouddeeltjes te detecteren met behulp van derde-harmonische generatie, een techniek waarbij een gouddeeltje aangeslagen wordt met een infrarode laserpuls, waarna het deeltje licht genereert met een frequentie die drie maal zo hoog is als de oorspronkelijke frequentie. Een tweede methode was gebaseerd op een combinatie van pomp-sonde spectroscopie en interferometrie, waarbij een laserpuls in tweeën werd gesplitst in een dubbelbrekend kristal. Na interactie met het sample werden de pulsen weer samengevoegd, waarop ze konden interfereren. Hiermee werden veranderingen in de optische eigenschappen van de gouddeeltjes gemeten die werden geïnduceerd door een pomppuls. Met deze laatste methode was het mogelijk om akoestische trillingen van het atoomrooster van individuele gouddeeltjes te meten.

Mijn bijdrage aan het onderwijs bestond uit het begeleiden van een Natuurkundepracticum en een werkcollege Optica. Tevens heb ik twee studenten begeleid, bij een bachelorstage en bij een masterstage.